STRUCTURAL AND FUNCTIONAL STUDIES OF BACTERIAL OUTER MEMBRANE PROTEINS

Hubing Lou

A Thesis Submitted for the Degree of PhD
at the
University of St Andrews

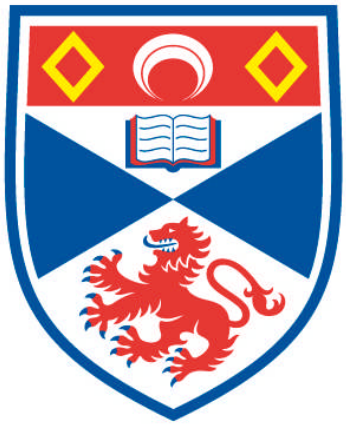

2010

Structural and functional studies of bacterial outer membrane proteins

Hubing Lou

A thesis presented for the degree of Doctor of Philosophy

School of Chemistry

University of St Andrews

Supervisor: Prof. James H. Naismith

January 2010

Declarations

I, Hubing Lou, hereby certify that this thesis, which is approximately 25,000 words in length, has been written by me, that it is the record of work carried out by me and that it has not been submitted in any previous application for a higher degree.

Date ……Signature of candidate ……

I was admitted as a research student in April, 2006 and as a candidate for the degree of Doctor of Philosophy in April, 2007; the higher study for which this is a record was carried out in the University of St Andrews between 2006 and 2009.

Date ……Signature of candidate ……

I hereby certify that the candidate has fulfilled the conditions of the Resolution and Regulations appropriate for the degree of PhD in the University of St Andrews and that the candidate is qualified to submit this thesis in application for that degree.

Date …….Signature of supervisor ……

In submitting this thesis to the University of St Andrews we understand that we are giving permission for it to be made available for use in accordance with the regulations of

the University Library for the time being in force, subject to any copyright vested in the work not being affected thereby. We also understand that the title and the abstract will be published, and that a copy of the work may be made and supplied to any bona fide library or research worker, that my thesis will be electronically accessible for personal or research use unless exempt by award of an embargo as requested below, and that the library has the right to migrate my thesis into new electronic forms as required to ensure continued access to the thesis. We have obtained any third-party copyright permissions that may be required in order to allow such access and migration, or have requested the appropriate embargo below.

The following is an agreed request by candidate and supervisor regarding the electronic publication of this thesis:

Embargo on both of printed copy and electronic copy for the same fixed period of one year on the following ground:

publication would preclude future publication.

Date …… ……signature of candidate …… ……

signature of supervisor ……

Acknowledgements

With no doubt, this thesis would never have been possible without Prof. James Naismith (Jim). It is his tremendous enthusiasm for scientific research, his firm support, complete trust, and freedom he has given that has inspired me throughout my PhD research.

Prof. Hagan Bayley at Oxford University also deserves my appreciation. During 4 months of working at his lab, Hagan was unconditionally supportive and he generously showed me a way of doing good research. It was a pleasant time working at Oxford, his postdocs Min Chen, Dvir Rotem, and Orit Braha were very kind and helpful.

Mention should also be made to the whole JHN group with a few people in particular. Kostas Beis, Jim's former student, shared with me his expertise on membrane protein crystallography. I also admired Changjiang Dong, Huanting Liu and Muse Oke, not only because of their knowledge and wisdom, but also because of their very gentle souls enlightened me during my dark time.

Last but not least, I thank my parents and younger sister who stand behind me whenever and whatever.

Abstract

This thesis studies two particular bacterial outer membrane proteins called OmpC and Wzi, focusing on their expression, purification, crystallization and X-ray structure determination.

A series of four naturally occurring OmpC mutants were isolated from a single patient with an *E. coli* infection of liver cysts. The isolated *E. coli* strains progressively exhibited increasing breadth of antibiotic resistance in which OmpC was predicted to take a partial role. We carried out an assay in which a strain of *E. coli* lacking OmpC was used to express the first (antibiotic sensitive) and the last (antibiotic resistant) of the clinical OmpC mutants and drug permeation assessed. Single channel conductance measurements were carried out and the X-ray structures for all the isolates were determined. Protein stability was assessed. With these data we propose that changes in the transverse electric field, not the pore size, underlie the clinically observed resistance to the antibiotics. This is the first demonstration of this strategy for antibiotic resistance.

Wzi is a novel outer membrane protein involved in the biosynthesis and translocation mechanism of the K30 antigen from *E. coli*. The mechanism is a complicated process that requires several proteins including outer and inner membrane proteins. The protein Wzi was expressed, purified and crystallized. Initial crystals were tested and diffracted to 15 Å. After optimization, a crystal diffracting to 2.4Å has been obtained.

List of abbreviations

Amino acids

Ala	A	Alanine	Leu	L	Leucine
Arg	R	Arginine	Lys	K	Lysine
Asn	N	Asparagine	Met	M	Methionine
Asp	D	Aspartic acid	Phe	F	Phenylalanine
Cys	C	Cysteine	Pro	P	Proline
Gln	Q	Glutamine	Ser	S	Serine
Glu	E	Glutamic acid	Thr	T	Threonine
Gly	G	Glycine	Trp	W	Tryptophan
His	H	Histidine	Tyr	Y	Tyrosine
Ile	I	Isoleucine	Val	V	Valine

Others

βOG	n-octyl-β-D-glucopyranoside
CCP4	Collaborative Computational Project Number 4
C_8E_4	octyl-tetraethylene glycol
EPPS	3-[4-(2-hydroxyethyl)-1-piperazinyl] propanesulfonic acid
HEPES	4-(2-hydroxyethyl)-1-piperazineethanesulfonic acid
HESO	2-hydroxyethyloctylsulfoxide
HMW	high molecular weight

IM	inner membrane
LB	lysogeny broth
LDAO	Lauryldimethylamine-oxide
LPS	lipopolysaccharide
Mass-spec	Mass spectrometry
MIC	minimum inhibition concentration
MTT	(3-(4,5-Dimethylthiazol-2-yl)-2,5-diphenyltetrazolium bromide
NAD+	Nicotinamide adenine dinucleotide (oxidized form)
NADH	Nicotinamide adenine dinucleotide (reduced form)
NADPH	Nicotinamide adenine dinucleotide phosphate (reduced form)
NCS	non-crystallographic symmetry
OD	optical density
OM	outer membrane
OMP	outer membrane protein
OPOE	n-octylpolyoxyethylene
PDB	protein data bank
PDC	protein-detergent complex
PEG	polyethylene glycol
PEG 2000 MME	polyethylene glycol 20000 monomethyl ethane
SDS-PAGE	sodium dodecyl sulfate polyacrylamide gel electrophoresis
SB 3.14	3-(N, N-Dimethylmyristyl-ammonio) propanesulfonate
TLS	Translation/Libration/Screw

Contents

Chapter 1

Introduction

Overview

Structure determination for membrane proteins is considered the biggest challenge among crystallography community today. Indeed, among more than 60000 PDB entries only 554 are membrane protein structures (October 2009); in other words, less than 1% of known structures are membrane proteins. However, it is predicted that 20-30% of the genomes of eubacterial, archaean and eukaryotic organisms encodes for membrane proteins and 70% of today's drugs act via membrane proteins. Therefore, it is crucial to determine the membrane proteins structures which will provide insights and basis for rational drug design.

One may ask why it is so difficult to obtain membrane protein crystal structures. In this chapter, the environment of membrane proteins is discussed and their difficult nature for crystallization explained. All the currently known structures of bacterial outer membrane structures are summarized.

1.1 The Gram-negative bacteria cell envelope

The cell envelope comprises three layers in Gram-negative bacteria such as *Escherichia coli*. These layers include the outer membrane (OM), inner membrane (IM) and a periplasmic layer in between (Nikaido and Nakae, 1979). Both membranes are bilayers composed by two leaflets, while the periplasmic layer is a gel-like fluidic band comprises proteins and peptidoglycan (Nikaido and Nakae, 1979). The inner (cytoplasmic) membrane is a symmetrical bilayer which is exclusively composed of phospholipids. Because of the hydrophobic nature of phospholipids, the IM represents a real diffusion barrier for hydrophilic solutes. Polar molecules such as sugars, nucleotides and ions move across the IM via specific integral membrane protein transporters (Nikaido, 2003). In contrast to the IM, the OM is a highly asymmetric bilayer which is composed by phospholipids in the inner leaflet and lipopolysaccharide (LPS) in the outer leaflet. The LPS comprises three domains: lipid A, core oligosaccharide, and O polysaccharides (O antigen repeats) (Figure 1.1.1) (Raetz and Whitfield, 2002). Many saccharides in the LPS are acidic and negatively charged. The charged nature of the outside LPS layer confers bacteria with high resistance to hydrophobic compounds; the lipid portion is almost impermeable to all charged molecules. Cells must import and export molecules to and from the environment; therefore, the OM contains channel-forming proteins, mainly a class of channels called porins that allow this (Nikaido, 2003).

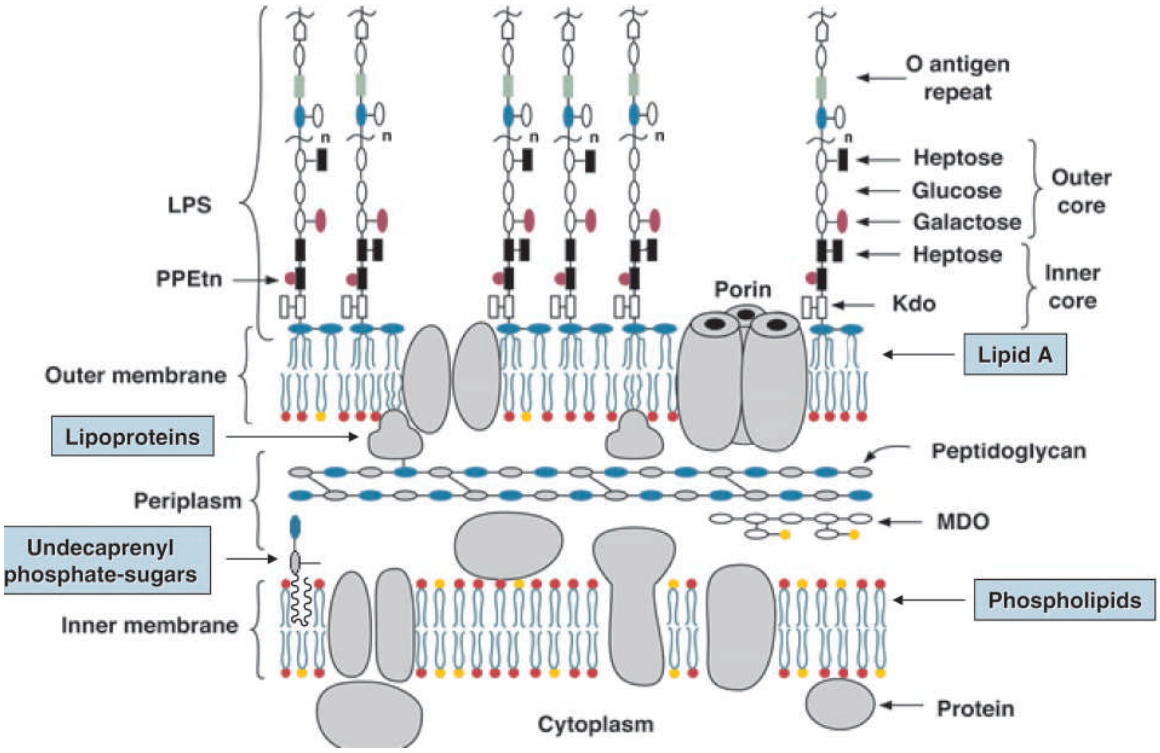

Figure 1.1.1 Schematic view of the inner and outer membranes of *E. coli* K-12. In the figure MDO is membrane-derived oligosaccharides; Kdo stands for 3-deoxy-D-manno-oct-2-ulosonic acid; PPEtn is short for pyrophosphorylethanolamine (Picture from Raetz and Whitfield, 2002).

1.2 The importance of membrane proteins and challenges of crystallization

Although the lipid bilayer comprises the backbone of Gram-negative cell membranes, membrane proteins perform the most of the specific functions, including respiration, signal transduction and molecular transport (Byrne and Iwata, 2002). Genome analysis of eubacterial, archaean, and eukaryotic organisms predicted that 20–30% of the open reading frames encode integral membrane proteins (Wallin and von Heijne, 1998). Moreover, many membrane proteins are critical components of genetic disorders and it is estimated that membrane proteins are targeted by more than 70% of today's drugs (Byrne and Iwata, 2002). It is therefore important to obtain high resolution membrane protein structures to understand their functions, which will provide insights and basis for new drugs and new therapies. The sequence and function of many membrane proteins are known, but only a small number of structures are elucidated to date. According to the "Membrane Proteins of Known 3D Structure" website of S. H. White (http://blanco.biomol.uci.edu/Membrane_Proteins_xtal.html), there are currently (October 2009) 554 membrane protein structures of which 204 are unique, in comparison to the more than 60000 structures of water-soluble proteins deposited in PDB (Protein Data Bank, October 2009, http://www.rcsb.org/pdb).

As nowadays, structure biology is becoming routine: expression, purification, crystallization and X-ray data analysis. Why it is still so hard to solve membrane protein structures? The barriers impact upon every step of structural determination. The recombinant expression and the following purification of sufficient amounts of membrane protein are often difficult. Moreover, numerous crystallization trials are necessary to get crystals that diffract to high resolution. Because of these reasons, membrane proteins of known structure in the database in early days are mainly naturally abundant. However, most membrane proteins are present in the cell at low concentrations (Hunte and Michel, 2002).

All membrane proteins that are transported to the outer membrane contain an N-terminal signal peptide, usually ~20 amino acids long, which directs them through the translocon in the IM to the periplasm. The signal peptide is removed during translocation by signal peptidases prior to protein folding and insertion into the membrane. For the recombinant production of outer membrane proteins it is important to take into account the signal peptide. *E. coli* is usually used as the host organism for the overexpression of either native or heterologous recombinant outer membrane proteins. In some cases the *E. coli* signal peptidase cannot process the signal peptide of heterologous proteins, resulting in the formation of inclusion bodies or no expression (Baneyx, 1999). Manipulation of the signal peptide of the target protein can resolve this problem (Hearn et al., 2008). Absence of the signal peptide from the recombinant protein results in the production of the target protein in the form of inclusion bodies. Outer membrane proteins expressed as inclusion bodies in

the absence of a signal peptide can be extracted and purified in the presence of urea in a relatively straightforward manner. A successful example of this method for protein production is the crystal structure of OmpG from *E. coli* (Yildiz et al., 2006).

Extraction and solubilisation of membrane proteins is challenging because of the extensive hydrophobic/amphiphilic surfaces. When the native membrane is removed during extraction and purification of the protein, suitable detergents have to replace the lipid that was in the native environment. Once extracted and purified, the membrane protein is in a form of protein-detergent complexes, or PDCs, which is the real starting material for membrane protein crystallization.

Membrane proteins do not crystallize readily. PDCs form crystals at the polar surfaces of the protein protruding from the detergent micelle, and most PDCs have only limited accessible hydrophilic surfaces (Hunte and Michel, 2002). The use of additives, such as heptane-triol, has played a significant role in membrane protein crystallization (Wiener, 2004). A goal has been to enlarge the polar surface of the protein, most often by attaching polar domains with specifically binding antibody fragments, to enhance crystallization (Ostermeier et al., 1995). The use of recombinant antibody fragments, in a form of either Fv (variable fragment, ~28 kDa) or Fab (fragment antibody binding, ~56 kDa), has been shown to improve the crystallization of several membrane proteins (Hunte et al., 2000; Iwata et al., 1995; Jiang et al., 2003).

1.3 Structures of bacterial outer membrane proteins

1.3.1 General and substrate-specific porins

Porins were the first outer membrane proteins (Omps) to be studied. The first x-ray structure of a porin from *Rhodobacter capsulatus* was determined in 1990 (Weiss et al., 1990) quickly followed by OmpF and PhoE from *Escherichia coli* (Cowan et al., 1992), a porin from *Rhodopseudomonas blastica* (Kreusch and Schulz, 1994), OmpK36 from *Klebsiella pnueumoniae* (Dutzler et al., 1999), Omp32 from *Comamonas acidovorans* (Zeth et al., 2000) and *Delftia acidovorans* (Zachariae et al., 2006), and more recently OmpC from *E. coli* K12 (Basle et al., 2006). These porins have the same basic architecture consisting of 16-stranded hollow β-barrels. They have all crystallized as trimers, with a three fold axis normal the membrane plane. The crystal structure of OmpC (Basle et al., 2006) is shown in Figure 1.3.1.1. The hydrophobic interactions between monomeric barrel surfaces stabilize the trimer. The barrels all show eight tight turns on the periplasmic side and eight large, irregular loops (L1 to L8) on the extracellular side. L2 interacts with the neighboring monomer to stabilize the trimer (Phale et al., 1998). L3 folds into the barrel forming a “constriction zone” at about midway into the barrel. As a result when viewed via a space-filling model, the central pore has an hourglass shape. In the constriction zone, there are acidic residues in L3 with a cluster of basic residues at the opposite barrel. These opposite charged residues created a transverse electrostatic field which is thought to make an important contribution to porin properties (Nikaido, 2003).

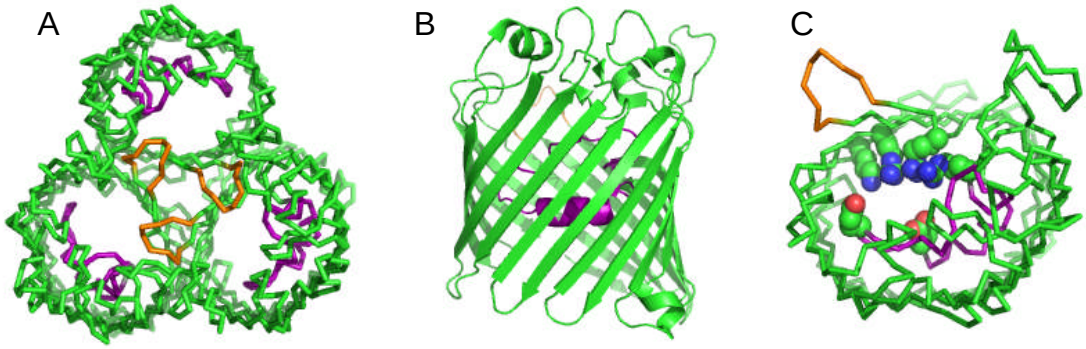

Figure 1.3.1.1 Structure of OmpC porin from *E. coli* (PDB code: 2J1N). (A) View of the trimer from the outside of membrane, loop L2 is colored in orange, L3 is in purple. (B) Side view of the monomer. (C) View of the constriction zone of the channel, featuring the opposite-charged residues that form the electrostatic field.

These porins are known as “general porins” and are water-filled channels with no particular substrate specificity. Their biological role is to control the passage of hydrophilic solutes based on the substrate molecular size (Nikaido, 2003). In addition to general porins, bacteria have substrate-specific porins which are also trimeric β-barrel proteins. The substrate-specific porins include the maltose-specific channel LamB from *E. coli* (Schirmer et al., 1995) and its homolog from *Salmonella typhimurium* (Phale et al., 1997), the sucrose-specific channel ScrY from *S. typhimurium* (Forst et al., 1998), and from *Pseudomonas aeruginosa* the phosphate-specific transporters OprP (Moraes et al., 2007), OprD (Biswas et al., 2007) and OpdK (Biswas et al., 2008).

Monomers of LamB and ScrY have 18 β-stranded structures instead of the 16 observed in general porins and also form a homotrimer, with the three-fold parallel to the membrane normal. Once again L3 folds back into the β-barrel (Figure 1.3.1.2). X-ray structure analysis of sugar-soaked LamB crystal identified a substrate translocation pathway (Schirmer et al., 1995) with of a number of aromatic amino acids as the “greasy slide” (Figure 1.3.1.2B) lined by polar residues the “ionic track” (Schirmer et al., 1995). The hydrophobic face of sugar makes van der Waals’ contacts with the greasy slide while the sugar hydroxyl groups make hydrogen bonds with the ionic track. It has been proposed that substrates move through the channel via a sequence of hydrogen bond making and breaking steps (Schirmer et al., 1995). The channel-lining residues are mostly conserved between LamB and ScrY, but the differences confer the specificity.

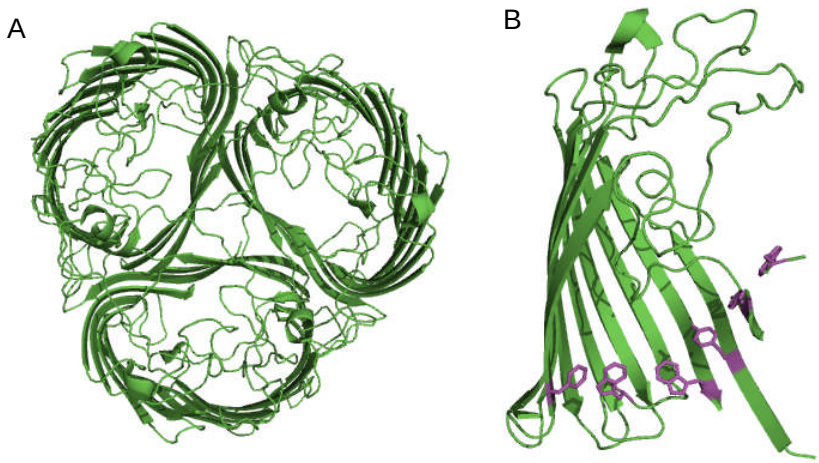

Figure 1.3.1.2 Structure of LamB (PDB code: 1MAL). (A) View of the trimer from extracellular side. (B) Aromatic residues that contribute to the greasy slide are shown in purple.

The *P. aeruginosa* OprP is a 16-stranded antiparallel β-barrel but unusually OprP has an extended periplasmic N terminus (Figure 1.3.1.3A) involved in stabilizing the trimer (Moraes et al., 2007). Inside the channel, there is a nine-residue arginine "ladder" spanning from the extracellular surface down to the constriction zone (Figure 1.3.1.3B). This ladder is proposed to control the transit of the phosphate anion (Moraes et al., 2007). The inner periplasmic surface is coated by lysine residues, creating an 'electropositive sink' that attracts the phosphates through the channel.

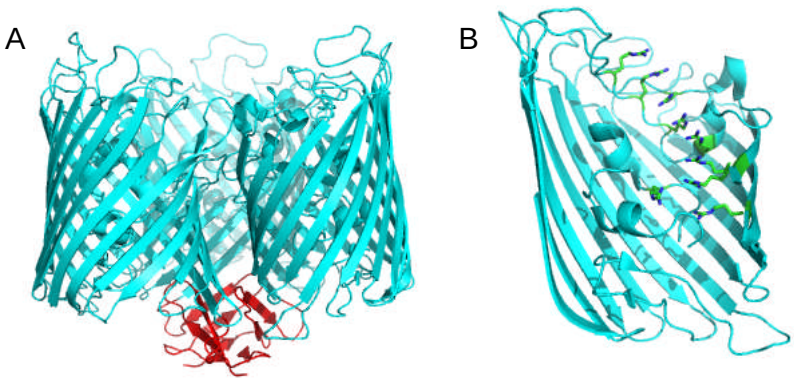

Figure 1.3.1.3 Structure of OprP (PDB code: 2O4V). (A) Side view of OprP trimer, the tricorn N terminal strands are colored red. (B) The arginine ladder located on the upper portion of the monomer of OprP is shown in stick representation

OprD and OpdK are 18 β-strand substrate-specific porins from *P. aeruginosa;* OprD takes up basic amino acids such as lysine and arginine (Trias and Nikaido, 1990) and OpdK is responsible for taking up vanillate and related small aromatic acids (Biswas et al., 2008).

They both crystallized as monomers as shown by their crystal packing. However, biochemical and biophysical studies showed that they form trimers in the bacterial outer membrane. Similar to OprP, OprD contains a ladder of arginine and lysine residues. In OpdK, only some of the ladder residues are present. Both OprD and OprK have similar charge distribution of the residues lining the pore. However, in OprD, the periplasmic funnel surface is negatively charged whilst in OpdK it is positively charged. This difference seems to underlie the differing substrate specificities.

1.3.2 Dimeric β-barrel proteins

Besides trimeric 16 to 18 β-strand porins, bacteria also have dimeric β-barrel proteins. The first dimeric structure was the outer membrane phospholipase A (OMPLA). OMPLA is an integral membrane enzyme which catalyzes the hydrolysis of acyl ester bonds in phospholipids in a Ca^{2+}-dependent manner (Ubarretxena-Belandia et al., 1998). Dimerization is essential for its function (Ubarretxena-Belandia et al., 1998).The monomer of OMPLA is a 12-stranded antiparallel β-barrel and like the porins, has long extracellular loops and short periplasmic turns. The interior OMPLA is polar with a hydrogen-bonding network, however the central pore of OMPLA does not apparently function as a channel (Snijder et al., 1999). The dimer interface is formed by one side of the barrel (Figure 1.3.2.1) and two Ca^{2+} ions are adjacent to the interface. The active sites lie at the outer edge of the barrel and at the interface between the two monomers.

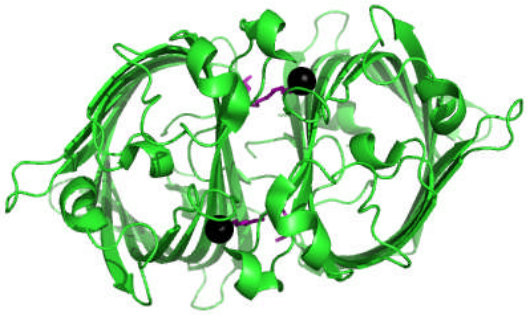

Figure 1.3.2.1 Structure of dimeric OMPLA (PDB code: 1QD6) viewed from the extracellular side. The two black spheres represent two calcium ions, the substrate analogue, hexadecanesulphonyl-fluoride, at the active sites are colored purple.

PapC is the translocation pore responsible for the assembly of adhesive pili on the surface of gram-negative pathogenic bacteria acting as P pilus usher (Remaut et al., 2008). P pili are complex extended fibers that are produced by pyelonephritic strains of *E. coli*. PapC is considered to the prototype for bacterial usher proteins and is found as a dimer arranged similarly to that seen for OMPLA. Each PapC monomer is a 24 β-stranded monomer (the largest barrel observed to date). A long sequence connects the two β-strands β6 and β7 and is located in the centre of the pore forming a "plug" domain. The plug domain is a six-stranded β-sandwich, the plane of the strands is parallel to the assumed membrane plane. The plug completely occludes the translocation pore and is held in place by a β-hairpin (connecting strands β5 and β6) that folds into the channel lumen. The only helix in the structure sits above (on the extracellular side) the β-hairpin (Figure 1.3.2.2). The inward curvature of the β5-6 hairpin creates a gap in the side of the β-barrel that is expected to extend into the outer membrane bilayer (Figure 1.3.2.2). This partly "missing stave" is thus far a unique feature.

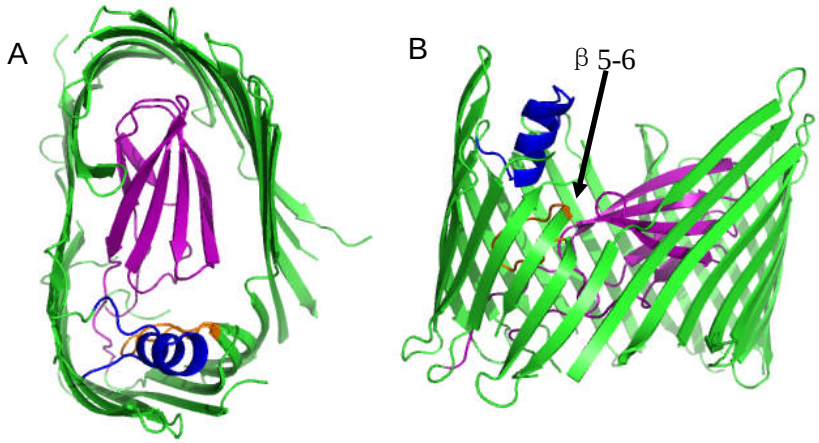

Figure 1.3.2.2 Structure of PapC translocation domain (PDB code: 2VQI). (A) The PapC translocation channel viewed from the extracellular side. The plug domain, the β5-6 hairpin, and the α-helix are colored purple, orange and blue, respectively. (B) β-barrel viewed from side. Structural elements are colored as in (A), the abnormal β5-6 is labeled.

1.3.3 TonB-dependent active transporters

In addition to trimers and dimers, monomeric β-barrel protein structures have been determined and they include structural proteins, enzymes and transporters. The TonB-dependent active transporters are 22 β-stranded barrel and use the proton motive force to transport specific substrates. The proton motive force acts from the cytoplasmic membrane through the TonB-ExbB-ExbD energy transducing complex across the bacterial outer membrane (Moeck and Coulton, 1998). Despite low sequence similarities (~15%) the iron-siderophore transporters FhuA, FepA, FecA from *E. coli*, FptA and FpvA from *P. aeruginosa*, the cobalamins (e.g., cyanocobalamin, vitamin B_{12}) transporter BtuB from *E. coli*, and the colicin I receptor Cir from *E. coli* all belong to this class (Cobessi et al., 2005). The strands of the β-barrel are connected by extracellular long loops and short periplasmic turns as already seen in porins. The N-terminal domain, often referred to as either the "plug" or "cork" domain, contains mixed four stranded β-sheets connected by a series of short β-strands, α-helices and irregular secondary structure elements. This domain is situated in the middle of the barrel (Figure 1.3.3.1A).

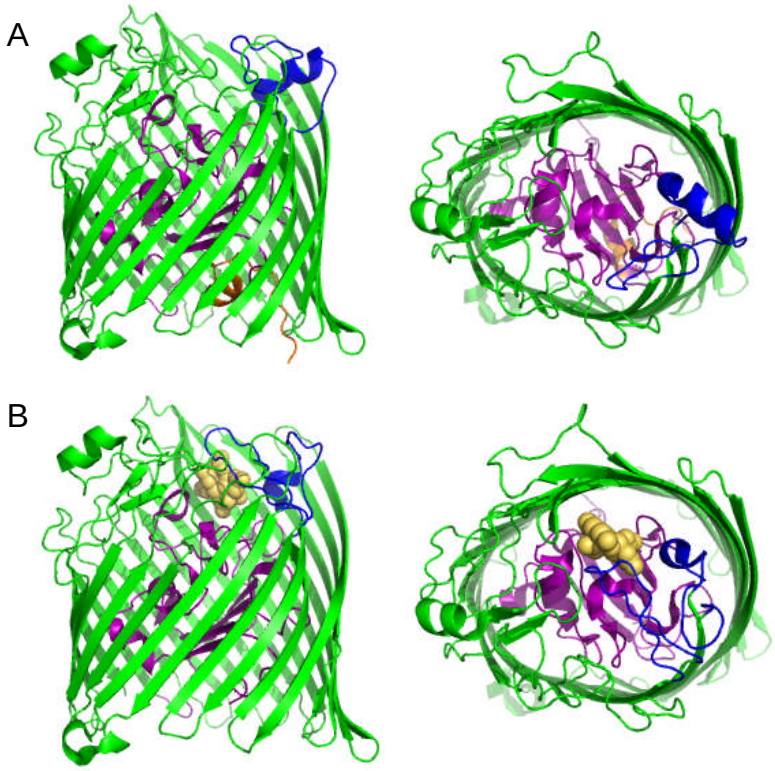

Figure 1.3.3.1 Crystal structure of (A) FecA (PDB 1KMP) and (B) FecA in complex with iron-free dicitrate (PDB 1PO0). The two extracellular loops L7 and L8, which undergo major conformational changes upon ligand binding, are shown in blue. The plug domain is colored purple. The switch helix colored orange, located in the periplasmic pocket of FecA, only observed in the unliganded conformation. The substrate iron-free dicitrate is shown as yellow spheres.

Siderophores are secreted by bacteria to acquire iron (Ferguson and Deisenhofer, 2002) and the iron siderophore complex is then transported through the outer membrane. All the iron-siderophore transporters characterized to date have essentially the same structure. The

barrels are 60-70Å in height and have an elliptical cross section. The transporters can exist in three states, (I) apo, (II) bound to siderophore and (III) bound to the iron-siderophore complex. All three binding states have been characterized for FecA (Ferguson et al., 2002; Yue et al., 2003). Comparison between the unloaded FecA and FecA bound to siderophore (citrate) reveals only minor differences (~1Å) in the extracellular loops L7 and L8. Major conformational changes occur when FecA binds the ferric citrate complex, including 10Å movements in the two extracellular loops L7 and L8. Conformational changes also occur in the plug domain and an N-terminal segment inside the periplasmic pocket, termed the 'switch helix'. The helix is thought to unwind and become disordered (Figure 1.3.3.1B). Structures of FhuA and FhuA - iron-ferrichrome complex have been reported by two independent groups (Ferguson et al., 1998; Locher et al., 1998). The barrel domain and the extracellular loops undergo only minor changes and the key differences lie in the plug domain and the 'switch helix'. Upon ligand binding, the plug domain is translated upward towards the ligand and the switch helix is completely unwound and rotated ~180° in the opposite direction of the former helix axis (Ferguson et al., 1998).

Compared to the structures of iron-siderophore transporters, BtuB and Cir have shorter transmembrane barrels with BtuB around 55Å and Cir around 40Å. In general these structures possess shorter extracellular loops, except that in Cir loops L7 and L8 are very long (Buchanan et al., 2007). Upon binding its substrate colicin Ia, Cir undergoes some conformational changes by moving its extracellular loops L7 and L8 as a rigid body. The

conformation became more open compared with the uncomplexed Cir structure (Figure 1.3.3.2) (Buchanan et al., 2007).

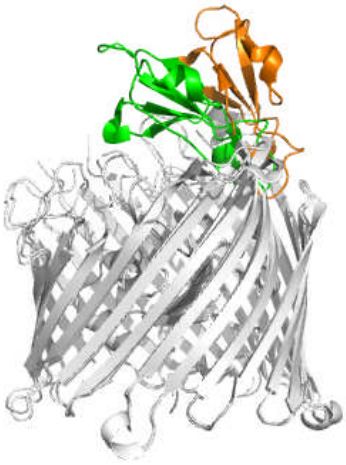

Figure 1.3.3.2 Conformational changes in Cir upon ligand binding. A superposition of uncomplexed Cir (PDB code: 2HDF) and colicin-bound Cir (PDB code: 2HDI) shows that the most significant change occurs in the extracellular loops L7 and L8. These loops are colored green in the apo Cir and orange in the Cir-colicin complex.

When BtuB binds the cyanocobalamin, small conformational changes occur in several extracellular loops and once again large changes can be observed in the plug domain. The Ton box, a highly conserved stretch of seven amino acid residues near the N-terminus of TonB-dependent transporters (Chimento et al., 2003) also undergoes change. Interestingly the conformational change in FhuA upon binding TonB is relatively minor (Pawelek et al., 2006) whilst the conformation of Ton box in BtuB-TonB complex is significant (Shultis et al., 2006). In all structures to date, the plug domain obstructs the channel therefore

conformational change of the luminal domain is required for to create a path for substrate. The nature of this change is not known.

1.3.4 Monomeric β-barrel proteins

OmpA, OmpX, OmpW, PagP from *E. coli*, and NspA from *Neisseria meningitides* all belong to the same 8 β-stranded barrel family (Figure 1.3.4.1). The basic architecture comprising of long extracellular loops and short periplasmic turns is again found in these proteins. However, there are important differences: PagP has a periplasmic N-terminal amphipathic α-helix (Figure 1.3.4.1d) and the interior of the OmpW barrel is a hydrophobic channel possibly involved in the transport of small hydrophobic molecules (Hong et al., 2006). Inside OmpA, OmpX and NspA, there is an extensive hydrogen-bonding network but no channel through which ions or other molecules could be transported (Pautsch and Schulz, 1998; Vandeputte-Rutten et al., 2003; Vogt and Schulz, 1999). PagP has an unusual interior: the hydrophobic upper half devoid of waters and the hydrophilic lower half with polar side chains (Ahn et al., 2004).

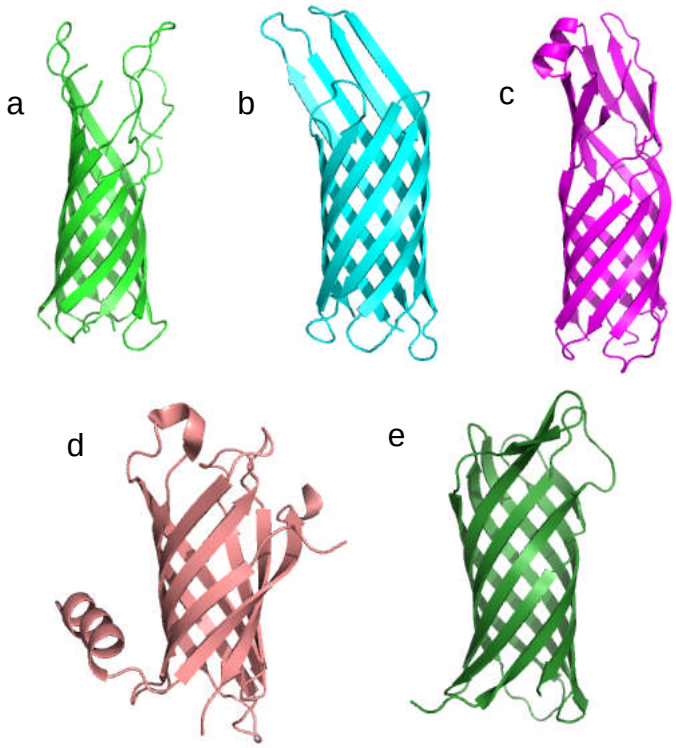

Figure 1.3.4.1 A gallery of 8-stranded β-barrel proteins. (a) OmpA (PDB code: 1BXW) (b) OmpX (PDB code: 1QJ8), (c) OmpW (PDB code: 2F1V), (d) PagP (PDB code: 1THQ), (e) NspA (PDB code: 1P4T).

Currently, there are only two outer membrane proteins with 10-strands have been structurally characterized. One is the protease OmpT from *E. coli* (Vandeputte-Rutten et al., 2001) and the other is adhesin OpcA from *Neisseria meningitides* (Prince et al., 2002). A comparison of these two structures showed that the overall fold was similar: a long transmembrane β-barrel that protrudes far from the lipid bilayer into the extracellular space (Figure 1.3.4.2). The top of OmpT barrel is circular whereas in the central part of the molecule is elliptical. In contrast, the OpcA barrel has an elliptical cross section along its

barrel axis. Both barrels are apparently accessible to water from the periplasmic side, but both are blocked on the extracellular face.

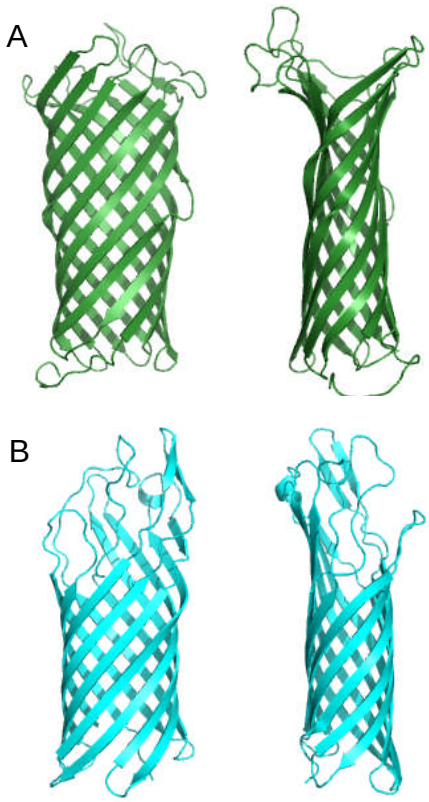

Figure 1.3.4.2 Structures of OmpT (PDB code: 1I78) and OpcA (PDB code: 1K24). (A) Side view of OmpT with 90 degree turn with respect to each other. (B) Side view of OpcA with 90 degree turn with respect to each other.

Twelve-stranded b-barrel membrane proteins have also been reported. These include the *E. coli* nucleoside transporter Tsx (Basle et al., 2004) and the *N. meningitides* autotransporter NalP β-domain (Oomen et al., 2004), which has an additional α-helical peptide (Figure 1.3.4.3A) in the middle. The autotransporter EspP from *E. coli* has a similar structure as NalP (Barnard et al., 2007) but unlike NalP, the β-domain of EspP begins with a short

α-helix. However, it is predicted that full length EspP contains an amphipathic α-helix spanning the length of the barrel pore as seen in NalP (Barnard et al., 2007). The autotransporter Hia from *Haemophilus influenzae* is a 12-stranded β-barrel domain superficially similar to that in NalP (Meng et al., 2006). Strikingly in Hia the barrel is assembled by three subunits with each contributing four β-strands. Three α-helices, one from each subunit, fill the central pore (Figure 1.3.4.3B). This is radically different from other bacterial outer membrane proteins discussed thus far whose barrels are typically formed from a single monomer.

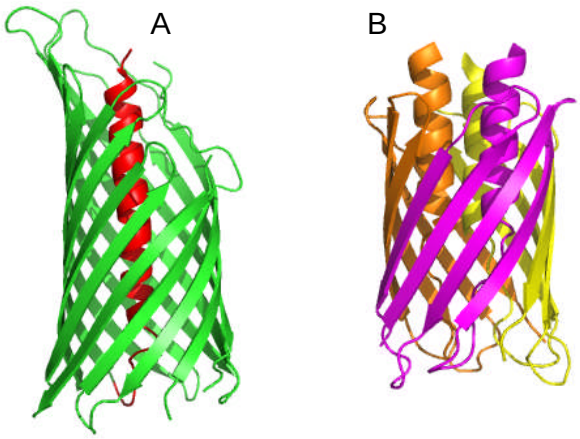

Figure 1.3.4.3 Structure of the β-domain from NalP (PDB code: 1UYN) and Hia (PDB code: 2GRB). (A) Side view of β-domain of NalP, the N-terminal α-helix is colored red. (B) Side view of Hia β-domain, each subunit is colored in a different color.

This multi subunit single barrel is also found in TolC (Koronakis et al., 2000), VceC (Federici et al., 2005), OprM (Akama et al., 2004), MspA (Faller et al., 2004) and α-haemolysin (Song et al., 1996). Although very different in sequence, *E. coli* TolC, *V. cholerae* VceC and *P. aeruginosa* OprM share a high degree of structural similarity. They have a 12 stranded β-barrel that is anchored to the outer membrane and is attached to a long α-helical periplasmic barrel. Both barrels are formed from three protomers (Figure 1.3.4.4). The β-barrel is completely open in TolC, while in both OprM and VceC three extracellular loops form a constriction. The α-helical barrel is closed at the periplasmic end in all three proteins and is assumed to represent a "resting state". As these three proteins are responsible for the export of drugs and other toxic compounds from the cytoplasm (Federici et al., 2005) the periplasmic domain must open during function.

α-haemolysin is assembled from seven subunits to form a 14 β-stranded barrel with a large extracellular domain shaped like a mushroom with a large central hydrophilic channel (Figure 1.3.4.4B). MspA from *Mycobaterium smegmatis* has a 16-stranded β-barrel formed from eight subunits (two stands per protomer) (Faller et al., 2004).

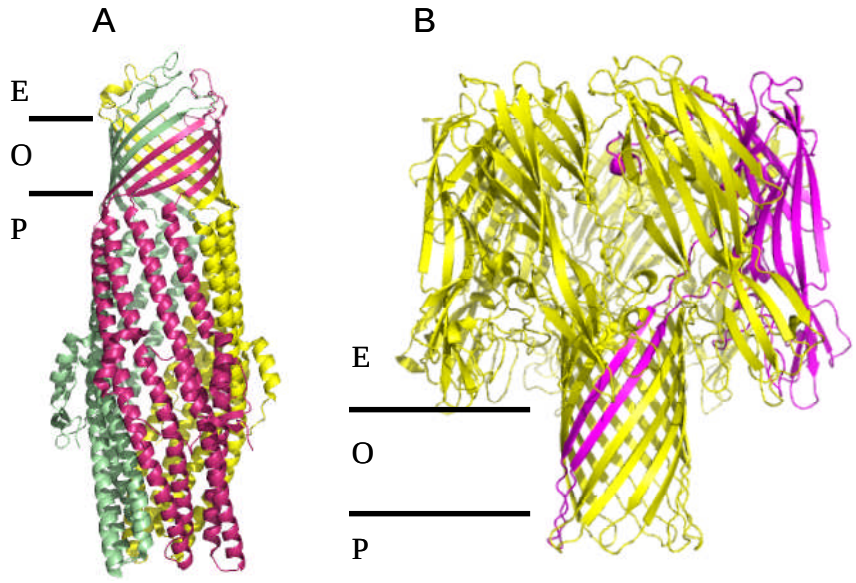

Figure 1.3.4.4 Structure of TolC (PDB code: 1EK9) and α-haemolysin (PDB code: 7AHL). (A)the three TolC subunits are colored differently.. (B) In the structure of α-haemolysin, one subunit is colored purple. The approximate position of the outer membrane (O), the extracellular side (E) and the periplasmic side (P) are indicated.

OmpG is a single protomer and is 14-stranded β-barrel functioning as a porin. OmpG has a large channel and lacks the constriction zone seen in other porins (Subbarao and van den Berg, 2006; Yildiz et al., 2006). Instead, OmpG has flexible extracellular loops which undergo conformational changes under different pH conditions. At neutral pH the pore is open (Figure 1.3.4.5A) but at pH 5.6 (or lower) the pore is blocked by loop L6 which folds across and into the channel (Figure 1.3.4.5B).

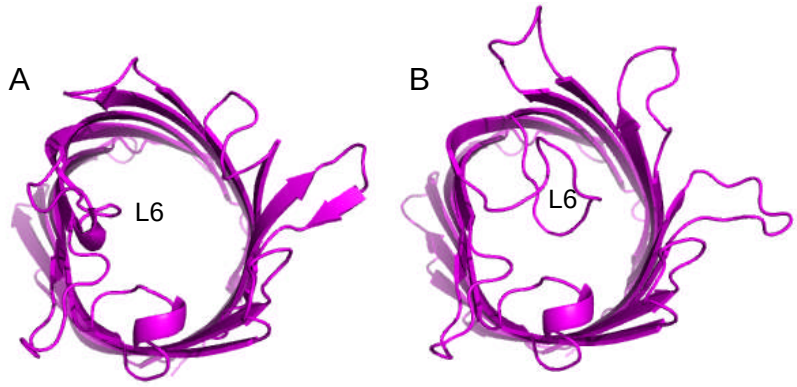

Figure 1.3.4.5 Structure of OmpG in two conformation states viewed from the extracellular side of the membrane. Loop L6 which undergoes largest conformational change is labeled. (A) Open conformation of OmpG (PDB code: 2IWV). (B) Closed conformation of OmpG (PDB code: 2IWW).

The fatty acid transporter FadL from *E. coli* (van den Berg et al., 2004), the aromatic hydrocarbon transporter TodX from *Pseudomonas putida* and TbuX from *Ralstonia pickettii* (Hearn et al., 2008) have a similar 14 β-stranded barrel. In each structure the lumen occluded by an N-terminal "hatch domain" consisting of three short helices. The L3 consists of two antiparallel α-helices which forms a hydrophobic cleft that is thought to bind substrate. In TodX and TbuX, the loop lies flat on the top of the barrel while in FadL it protrudes into the extracellular environment (Figure 1.3.4.6). Based on structural data, a model has emerged in which substrate is bound by the extracellular loop L3 before transit into the central hydrophobic channel. A conformational change of the hatch domain allows substrate to diffuse into the periplasm.

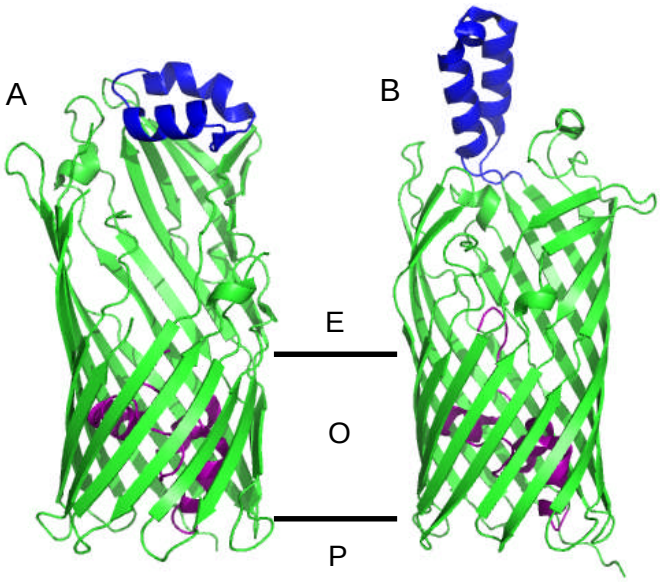

Figure 1.3.4.6 Structure features of TodX (A, PDB code: 3BSO) and FadL (B, PDB code: 1T16). The N-terminal hatch domain is colored in purple, the extracellular loop L3 is in blue. The position of outer membrane (O), the extracellular side (E) and the periplasm (P) are indicated.

As has been seen despite the variability, the dominant feature of outer membrane proteins is the β-barrel architecture. β-barrel proteins are transported and assembled by a specialised protein transport machinery involving multiple proteins (Kim et al., 2007). The outer membrane protein 85-two-partner secretion B (Omp85-TpsB) superfamily is at the heart of this system. Omp85-TpsB is thought to contain a C-terminal β-barrel region and an N-terminal region with putative polypeptide-transport-associated (PORTA) domains (Clantin et al., 2007). FhaC, an outer membrane protein from the Omp85-TpsB transporter family, plays a role in the secretion of filamentous hemagglutinin (FHA) from *Bordetella pertussis* (Clantin et al., 2007). FhaC is a monomer comprising of a 16 stranded β-barrel

with the loop L6 forming a hairpin inserted into the barrel. The extracellular N-terminus of the protein is a long α-helix (H1), and this helix spans through the transmembrane β-barrel. The helix connects to a periplasmic module that precedes the β-barrel. The periplasmic module consists of two structurally related PORTA domains. The domains, both 75 residues with the same topology of strand-helix-strand-strand, consist of a three-stranded β-sheets and one α-helix (Figure 1.3.4.7). The two domains are thought to recognize the N-terminus of FHA, providing a template for assembly and export. Translocation is proposed to start with FHA which adopts an extended β-hairpin structure during transit which refolds at the cell surface. After the C-terminus of FHA has reached the cell surface, the N-terminus of FHA dissociates from PORTA1 and completes translocation (Clantin et al., 2007). This templating function of the POTRA domains is predicted to be the basis by which β-barrels themselves are formed. A stretch of amino acids in the unfolded protein binds to the POTRA domain creating the first β-strand against which the other strands of the protein assemble. This process once started is presumably spontaneous. The β-barrel structure is extremely strong, being held together by extensive main chain hydrogen bonds. In fact many β-barrels can be removed from the membrane by very harsh detergents without unfolding, they are relatively insensitive (at least in the membrane portion) to proteases and can be handled quite harshly during purification (precipitation for example).

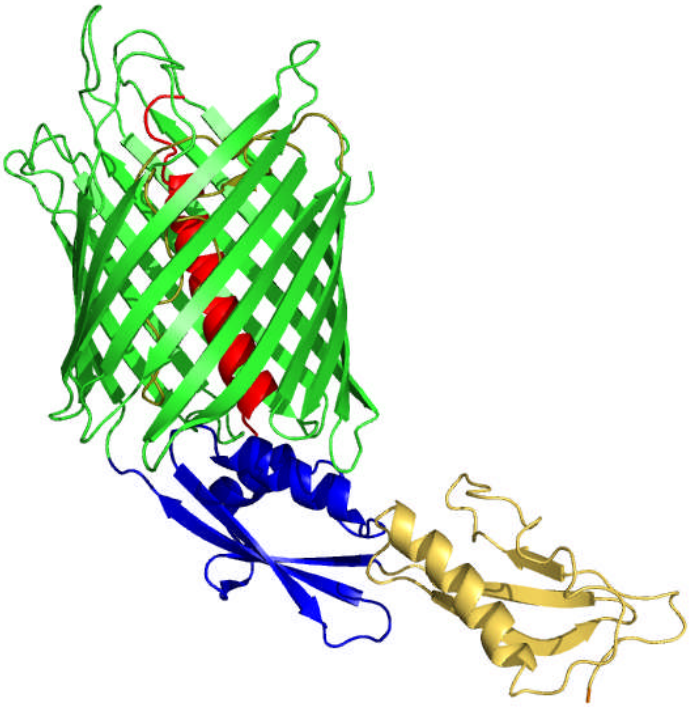

Figure 1.3.4.7 Structure of FhaC (PDB code: 2QDZ). The α-helix H1 is colored red, PORTA 1 yellow, PORTA 2 blue, loop L6 in olive.

1.3.5 α-helix outer membrane protein

Until recently all outer membrane proteins were presumed to follow the β-barrel paradigm and POTRA templating system provided a simple rationale for this. The structure of Wza showed this not to be the case, it has an α-helical barrel which spans the outer membrane (Dong et al., 2006). Wza is assembled from eight protomers with a very large central periplasmic cavity (reminiscent of TolC) (Figure 1.3.5.1). Although the α-helical barrel is completely open, the central cavity is closed to the periplasm. Creating an opening into this

central cavity would seem essential for function but the trigger for any such opening is unknown.

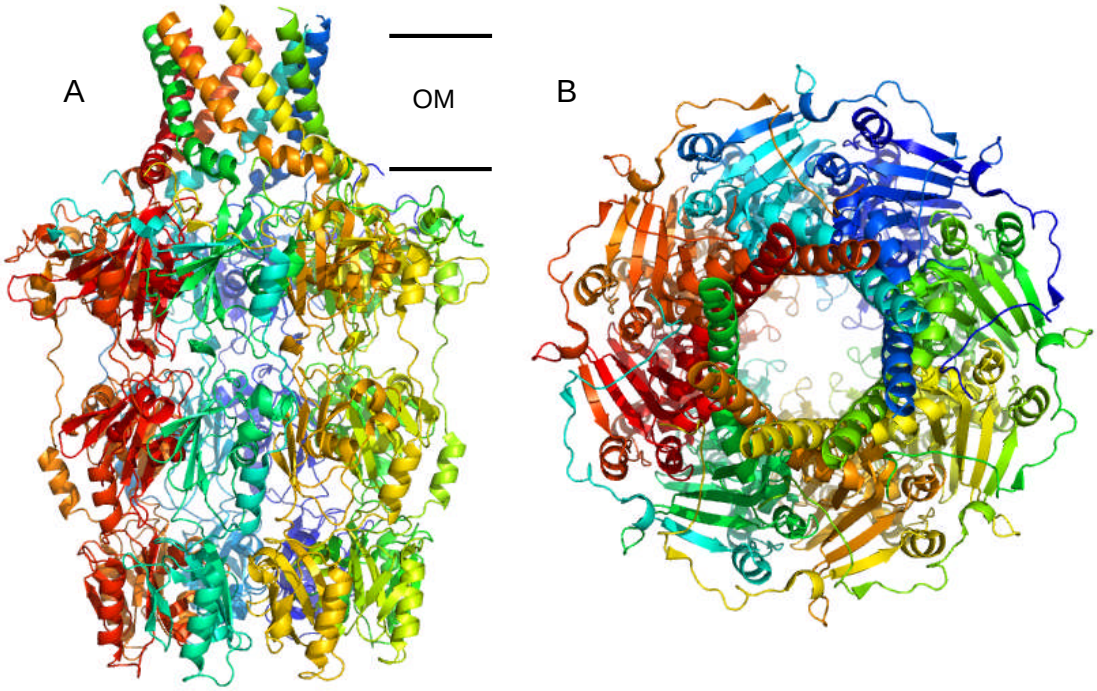

Figure 1.3.5.1 Structure of Wza (PDB code: 2J58). (A) Side view of Wza. The outer membrane (OM) position is marked. (B) The channel of Wza, viewed from outside of the cell.

The structure of Cytolysin A (ClyA) from *E. coli* K12 at its membrane state (Mueller et al., 2009) is the second example of α-helical outer membrane proteins. ClyA is a pore forming toxin (PFT). PFTs are produced as soluble proteins by their host organisms and can transform into the membrane integrated state (Parker and Feil, 2005). PFTs are of two kinds: α-PFTs or β-PFTs, depending on their types of pores integrated into the membrane

(Gouaux, 1997). The structure of ClyA is of cylinder shape comprised by 12 α-helical protomers (Mueller et al., 2009) (Figure 1.3.5.2). The crystal structure of ClyA in the membrane state is different from its soluble state, indicating an extensive conformational change have to take place (Mueller et al., 2009).

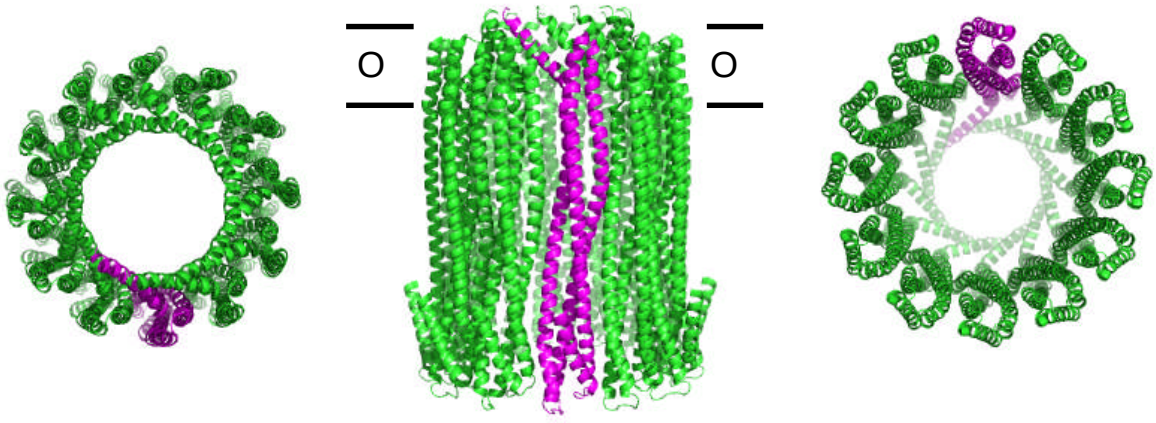

Figure 1.3.5.2 Structure of ClyA (PDB code: 2WCD). View from top (left). View from side (middle). The outer membrane (OM) position is marked. View from bottom (right). One protomer is colored magenta and the rest are green.

Chapter 2

The role of OmpC porin mutants in clinical drug resistance

Summary

Clinical (as opposed to laboratory) antibiotic resistance is a complex process in which numerous factors contribute. The clinical strains referred to in this study, were isolated from a patient with an *E. coli* infection of liver cysts and suffering from Caroli Syndrome (Low et al., 2001). The patient was treated by a variety of antibiotics over a period of four years from December 1994. The clinical strains, isolated from the last two years of the patient's life, progressively exhibited greater antibiotic resistance in which the last isolate showed resistance to a broad spectrum of antibiotic (Low et al., 2001). The later isolates all evolved from the first single focal infection with an *E. coli* strain which was deficient in OmpF expression and carried a unique *ompC* gene (OmpC20). While deciphering each factor that contributed to antibiotic resistance would be beyond the scope of our study, we wished to determine the role of OmpC mutants in the antibiotic resistance. We carried out the MTT assay in which a control strain of *E. coli* lacking OmpC was transformed with OmpC20 (isolated from the antibiotic sensitive strain) and OmpC33 (isolated from the antibiotic resistant strain) and their ability to uptake antibiotics was compared. Results suggested that OmpC does make contributions to the clinical antibiotic resistance.

2.1 Introduction

2.1.1 β-lactam antibiotics

Antimicrobial compounds are considered one of the most significant discoveries of the 20th century. They have been in wide application since the 1940's after Alexander Fleming discovered penicillin in 1920's. Ever since then, different antibiotics have been discovered and developed and they fall into several different classes, the most common of which are described below.

The β-lactam class are the most frequently used antibiotics in clinical practice and account for about 50% of antibiotic use world-wide (Livermore, 1998). β-lactam antibiotics can be divided into groups according to their chemical structure. They share the common structural feature of the four-membered β-lactam (azetidin-2-one) ring. The β-lactam class includes the penicillins and cephalosporins. Penicillins are N-acylated derivatives of 6-β-amino penicillanic acid as shown in figure 2.1.1.1. The basic structure of penicillins is a tripeptide intermediate which can be synthesed by two amino acids: valine and cysteine. The third amino acid (R in the diagram) of this tripeptide confers the diversity of penicillins and it also gives specific properties on different types of penicillins.

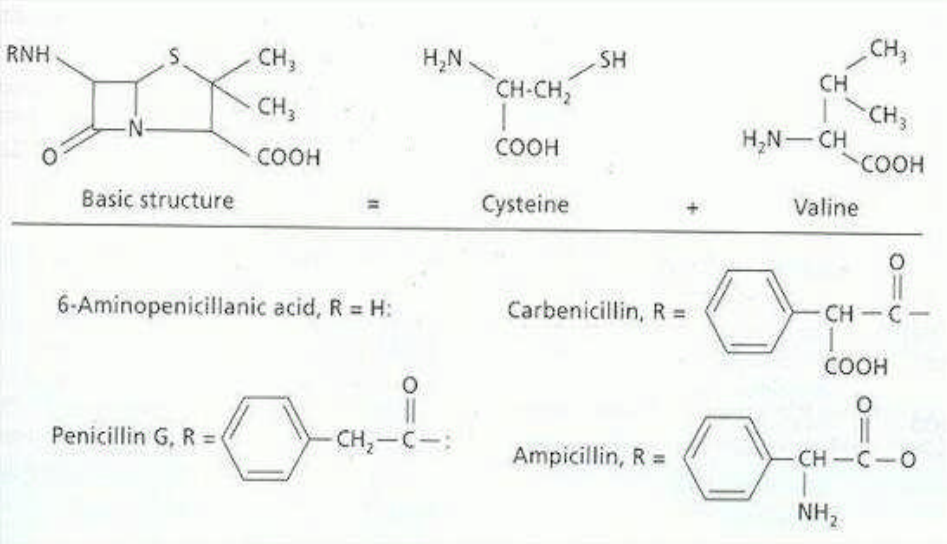

Figure 2.1.1.1 Molecular structures of some penicillin antibiotics (Diagram adapted from website http://helios.bto.ed.ac.uk/bto/microbes/penicill.htm).

Cephalosporins are N-acylated derivatives of 7-β-aminocephalosporanic acid. These compounds have the β-lactam ring fused to a 6-membered dihydrothiazine ring containing sulphur and a double bond (Figure 2.1.1.2). Two sites (marked as R and X in the diagram) can be modified, giving rise to a huge number of semi-synthetic derivatives. Cephalosporins are grouped into a series of generations (Babic et al., 2006). Early compounds such as cephaloridine are defined as the first generation; compounds resistant to β-lactamases such as cefuroxime are the second generation and compounds not only resistant to β-lactamases but also with enhanced antibacterial activity, such as cefotaxime, are the third generation cephalosporins. More recently, fourth and fifth generation

cephalosporins have been recognized and described (Babic et al., 2006). The newer cephalosporins generations have more enhanced Gram-negative antimicrobial abilities.

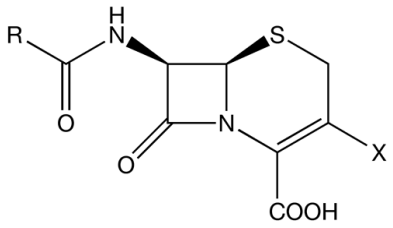

(a)

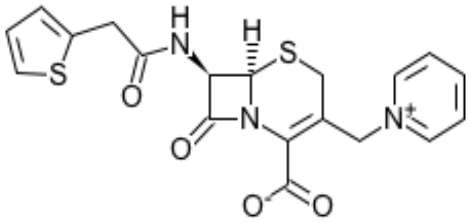

(b)

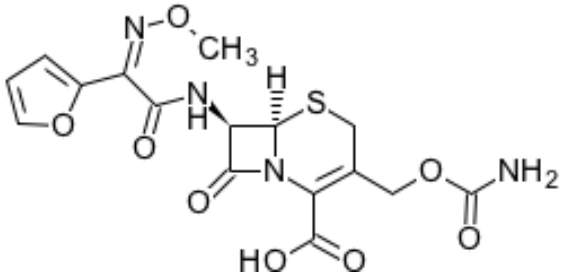

(c)

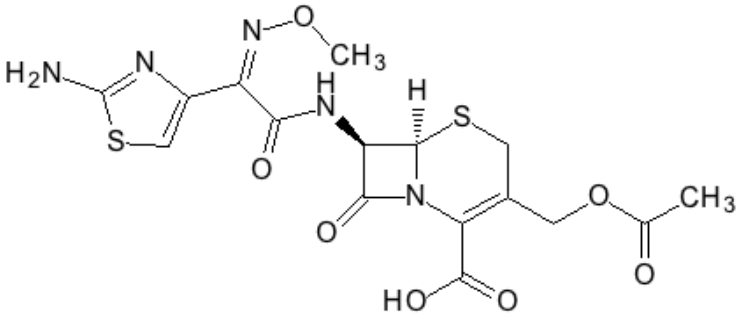

(d)

Figure 2.1.1.2 Structure of cephalosporin antibiotics. (a) cephalosporin backbone. (b) cephaloridine. (c) cefuroxime. (d) cefotaxime.

2.1.2 Antibiotic resistance

At the early days of antibiotic application, due to the effectiveness of the antibiotics, various bacterial diseases were considered to be defeated (Kumar and Schweizer, 2005). However, the widespread use and misuse of antibiotics has selected antibiotic-resistant pathogens, including the multi-drug resistant strains (Levy, 1998; Neu, 1992). These resistant bacteria are of two kinds: opportunistic and professional (Neu, 1992). These bacteria make use of a variety of ways to combat with antibiotics. They can degrade the drug, inactivate the drug by enzymatic modification, or alter the drug target (Davies, 1994). The resistance of Gram-negative bacteria to the β-lactam is a combination of β-lactamases, outer membrane permeability and efflux systems (Babic et al., 2006; Kumar and Schweizer, 2005; Lambert, 2005).

In Gram-negative bacteria, one important mechanism of resistance is the inactivation of β-lactam antibiotics by periplasmic enzymes called β-lactamases (Massova and Mobashery, 1998). Beta-lactamases are proposed to be descended from cell wall biosynthetic enzymes, the so-called penicillin-binding proteins (PBPs) (Medeiros et al., 1987). PBPs are present on the surface of the cytoplasmic membrane in almost all bacteria and they are essential enzymes that catalyze the peptidoglycan synthesis process. The structures of β-lactams are similar to one of the subunits that comprise peptidoglycan; therefore when PBPs use penicillin as the substrate mistakenly for cell wall synthesis, the following steps in cell wall synthesis are hindered and eventually bacteria killed (Babic et al., 2006). Beta-lactamases hydrolyze the β-lactam ring and inactivate the antibiotic before

it reaches the PBP target. The structural closeness between β-lactamases and PBPs allows β-lactamases to hydrolyze and inactivate the β-lactam (Massova and Mobashery, 1998).

The permeation of antibiotics through the outer membrane of Gram-negative bacteria is largely governed by porins (Nikaido, 2003) and altered porin properties have been observed in many drug resistant bacteria (reviewed in (Pages et al., 2008). It has been shown that loss of porin in *K. pnuemoniae* confers resistance to cephalothin and cefotaxime (Chevalier et al., 2000). Several studies reported the alteration of porin patterns contribute to the exclusion of antibiotics. In *K. pnuemoniae* strains highly resistant to a number of cephalosporins, there is an expression shift: the narrower-channel porin, OmpK36 (an OmpC homolog) is expressed in favor of the larger-channel porin, OmpK35 (an OmpF homolog) (Hernandez-Alles et al., 1999). It has been shown that *E. coli* resistant to certain β-lactam antibiotics have increased OmpC levels at the expense of OmpF, even at low osmolarity (Harder et al., 1981). There are also reports on mutations in the constriction zones in porins from pathogens to confer antibiotic resistance, such as *Enterobacter aetogenes* (Thiolas et al., 2004) and *Neisseria gonorrhoeae* (Olesky et al., 2002).

Active drug efflux systems in bacteria are believed to be another important mechanism of resistance. They can be divided into four families on the basis of supermolecular assembly, mechanism, and sequence homology (Nikaido, 1994a). These are the major facilitator family (MFS) (Marger and Saier, 1993), small mutidrug resistance family (SMR) (Grinius

et al., 1992), resistance-nodulation-division family (RND) (Saier et al., 1994), and ABC [adenosine triphosphate (ATP)-binding cassette] transporters (Nikaido and Saier, 1992). To pump out drugs, the first three families use a proton-motive force as a source of energy, whereas the ABC transporters utilize ATP. Some efflux pumps are selective and only pump out specific antibiotics. However, there are also multi-drug resistance (MDR) pumps that have the ability to remove a large number of unrelated and structurally diverse drugs from the cell (Lewis, 1994). It is well known that in Gram-negative bacteria, there are three-component export systems that contain a transporter which is a cytoplasmic membrane protein, an outer membrane channel and a periplasmic protein. Such systems have been identified and include: AcrAB-TolC (Figure 2.1.2.1) (Koronakis, 2003; Wandersman and Delepelaire, 1990), and mexA-mexB-oprK (Poole et al., 1993).

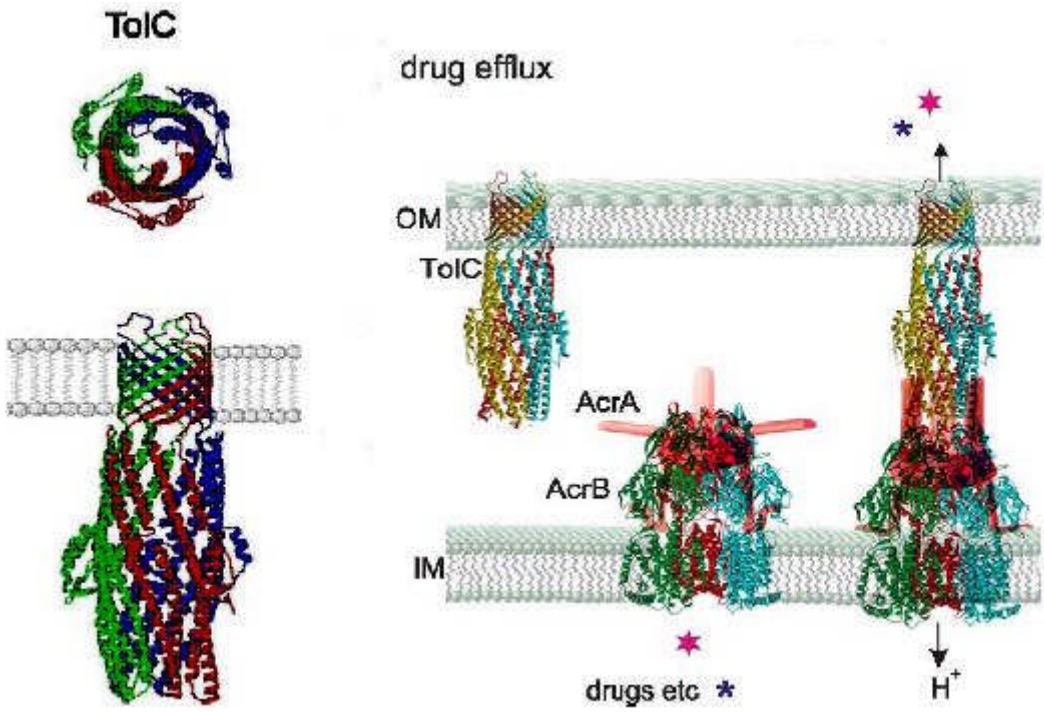

Figure 2.1.2.1 Structure of TolC and model of drug efflux. (Left) The structure of the outer membrane protein TolC. (Right) The drug efflux is achieved by TolC interacting with AcrA, a membrane fusion protein, and AcrB, an inner membrane efflux transporter (Okusu *et al.*, 1996) (Picture extracted from Koronakis, 2003).

2.1.3 MTT assay

MTT assay is one of the colorimetric assays used for measuring the activities of enzymes reacting with MTT. The key component, MTT, in this system is 3-[4,5-dimethylthiazol-2-yl]-2,5-diphenyl tetrazolium bromide (Figure 2.1.3.1 left). MTT is one of the tetrazolium salts that have various applications in cell biology (Berridge et al., 2005). At the core of the tetrazolium structure, four nitrogen atoms form a positively charged quaternary tetrazole ring (see the structure of MTT in figure 2.1.3.1), and this ring is usually surrounded by three aromatic groups (Berridge et al., 2005). Tetrazolium salts are water-soluble, after reduction, their colorless or weakly colored solutions can be transformed into intensively colored formazan precipitate. The dissolved formazan can be measured spectrophotometrically and the reaction has become the basis of biochemical application of tetrazolium salts.

Aqueous solutions of MTT are yellowish in color. Due to the presence of phenyl rings that provide the hydrophobic properties of the molecule, MTT is able to enter cells readily. It is believed that MTT is reduced by NAD(P)H-dependent oxidoreductases and dehydrogenases of metabolically active cells (Berridge et al., 2005). The reduction results in intracellular insoluble blue-magenta colored formazan crystals (Figure 2.1.3.1 right) which however can be dissolved in acidified isopropanol resulting in a purple solution (Denizot and Lang, 1986; Mosmann, 1983). The assay first described by Mosmann was used to measure cell proliferation and cytotoxicity (Mosmann, 1983). Since then, this essay

and its modified version have been used extensively to characterize the cell metabolic activity. The reduction takes place only when the cells are metabolically active; dead cells do not react with MTT (Berridge et al., 2005; Ulukaya et al., 2008) . Cytotoxic compounds damage or kill the cells, which result in the reduced ability for the reduction of MTT. Therefore this reaction is often used as a measure of living cells as higher number of live cells results in higher amount of MTT formazan hence higher spectrophotometerical absorbance. When the live cells are treated with an agent, say antibiotics, the resulting purple formazan can be compared with that produced by the control cells; the effectiveness of the antibiotics can be deduced from this difference.

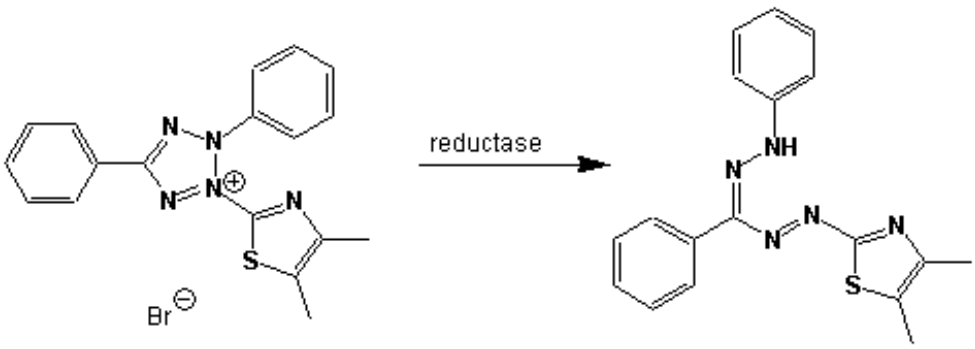

Figure 2.1.3.1 Yellow MTT (left) (3-(4,5-Dimethylthiazol-2-yl)-2,5-diphenyltetrazolium bromide, a tetrazole) can be reduced to purple formazan (right) in living cells.

2.1.4 Project background

This project has been in collaboration with Professor Ian Booth, University of Aberdeen. We have chosen to study naturally occurring mutants of the OmpC porin from a clinical *E. coli* infection. The OmpC mutants were isolated from a patient with an *E. coli* infection of liver cysts and suffering from Caroli Syndrome. The patient was treated by a variety of antibiotics over a period of four years from December 1994. *E. coli* isolates were collected, either from blood samples or directly from liver abscesses over a two year time period (Low et al., 2001). Measurement of the minimum inhibitory concentrations (MIC) for each of the antibiotics used during treatment of the patient had shown that the *E. coli* isolates had, in general, progressively greater antibiotic resistance (Figure 2.1.4.1). The last isolate shows broad spectrum antibiotic resistance (Low et al., 2001). The later isolates all evolved from the first single focal infection with an *E. coli* strain which was deficient in OmpF expression and carried a unique *ompC* gene (OmpC20) (Low et al., 2001). OmpC20 differs from the "standard" uropathogenic OmpCO6 (Welch et al., 2002) strain at 27 amino acids, and with an 8 residue deletion in loop L4 and 4 residue deletion in L7 (Figure 2.1.4.2). There is no data on when or where the changes between OmpCO6 and OmpC20 took place (may not have been in patient), our study is focused on the change from the first isolate (antibiotic sensitive containing OmpC20) to the final isolate (antibiotic resistant containing OmpC33). During the infection, the OmpC gene mutated to OmpC26 (mutation D18E), then to OmpC28 (additional mutation S271F), and finally to OmpC33 (additional mutation R124H) (Figure 2.1.4.2). These changes correlate with increase in clinical antibiotic resistance.

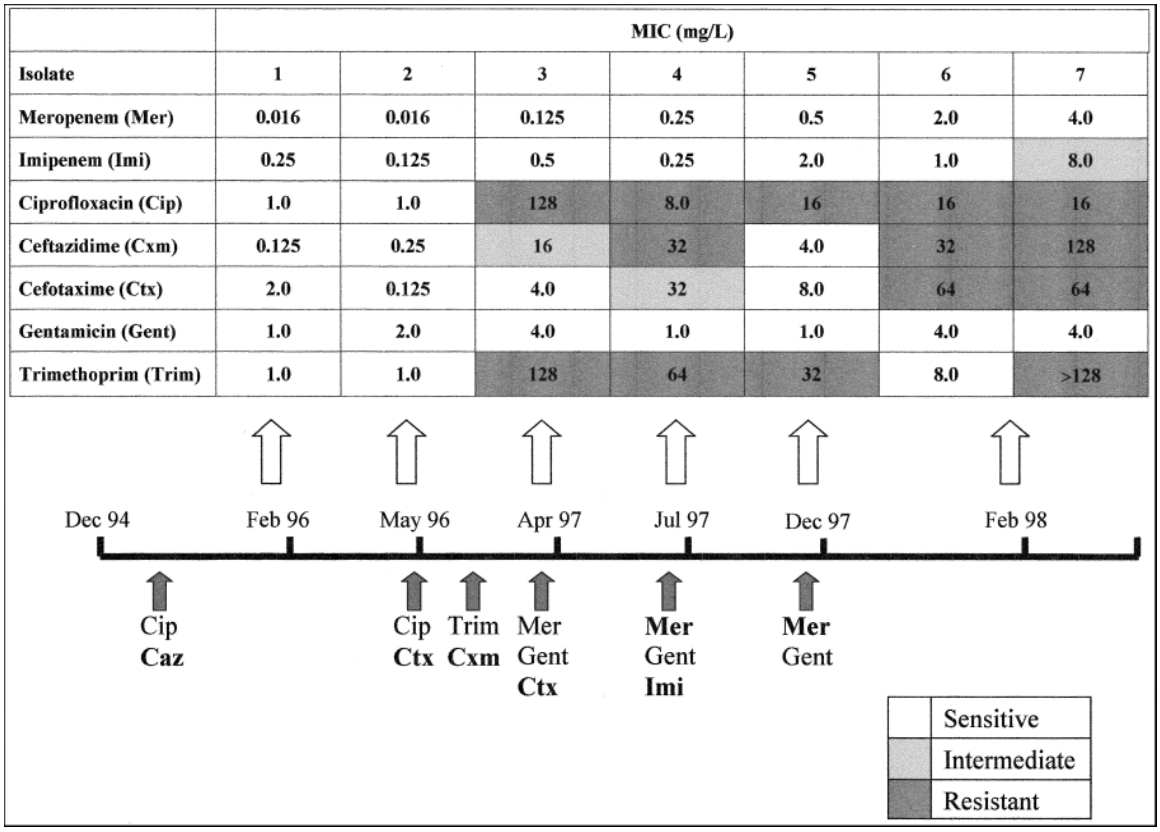

Figure 2.1.4.1 Antibiotic resistance in the seven isolates (Figure from Low *et al.*, 2001). The OmpC protein from clinical *E. coli* strain No. 1, 2 and 3 are denoted as OmpC20, isolate 4 as OmpC26, isolate 5 as OmpC28 while OmpC33 refers to isolate No.6 and 7. The antibiotic therapy received by the patient is indicated on a time line below the MIC table. Filled arrows indicate dates on which the antibiotic combination was changed. β-lactam antibiotics are indicated in bold. Open arrows indicate when each isolate was obtained.

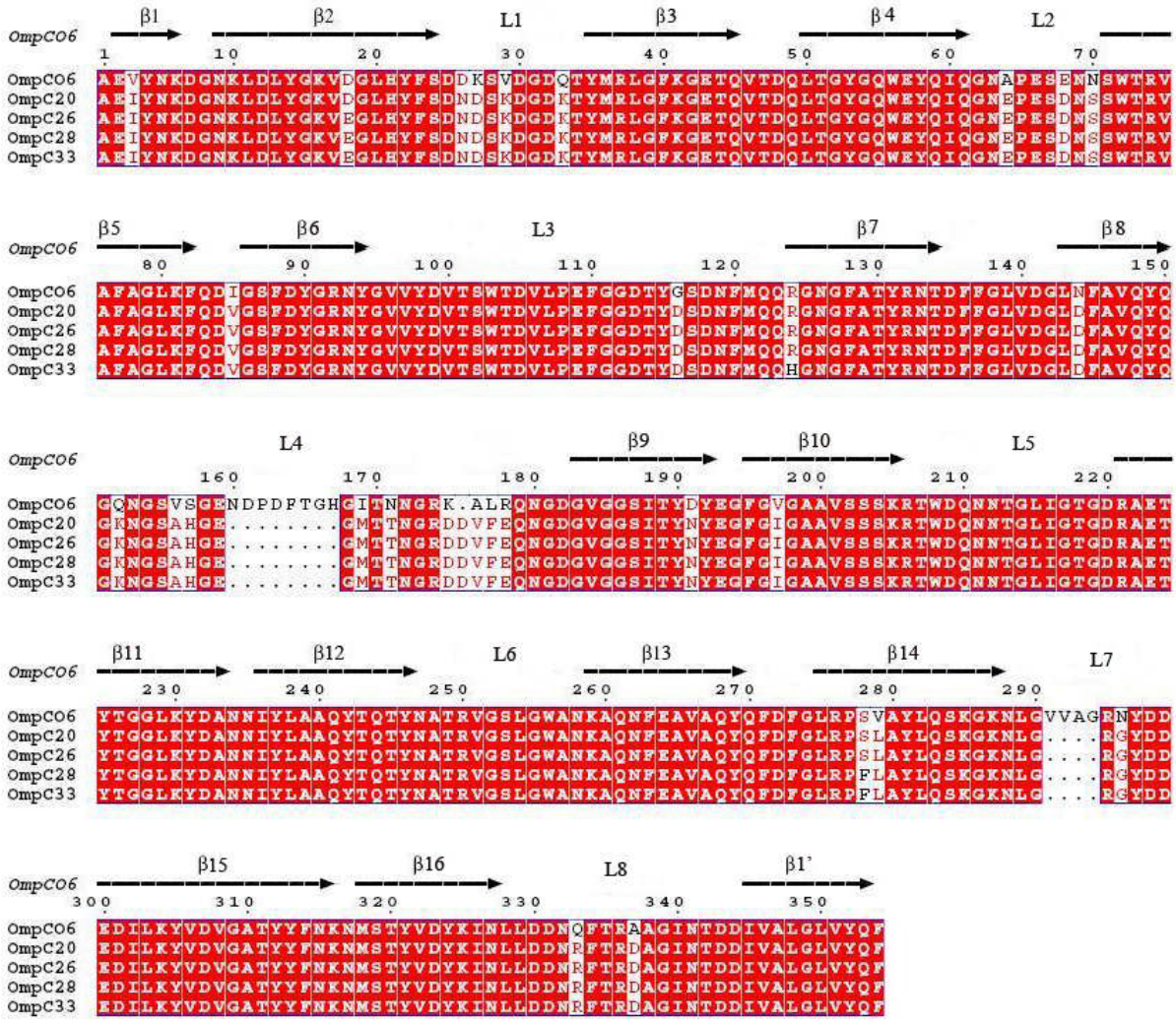

Figure 2.1.4.2 Sequence Alignment of OmpC from clinical isolates stated in Low *et al* 2001, and OmpCO6 from uropathogenic *E. coli* O6:H1 (accession no. Q8CVW1). The alignment was carried out in Multalin (Corpet, 1988). Above the alignment, the β-strands forming the barrel and the extracellular loops connecting the β-strands are numbered. The β-strands are labeled β1-β16 and β1', strand β1 from the N-terminal and strand β1' from the C-terminal are two parts of the same strand. The residue numbering is according to that of OmpCO6.

Clinical antibiotic resistance is often multifactorial and no single change in any protein can be said to "cause" its occurrence. In order to investigate the contribution of the OmpC porins to antibiotic resistance, the wild type *ompC* gene from *E. coli* K12 (OmpCK12) was expressed from the plasmid *pOmpCWT* in the first (containing OmpC20) and the last (containing OmpC33) clinical isolates, respectively. Results showed that in the first clinical isolate there were no significant differences in MIC in the presence or absence of OmpCK12. However, the last transformed clinical isolate recovered susceptibility to antibiotics, particularly for the two carbapenem antibiotics, meropenem and imipenem (Table 2.1.4.1, courtesy Professor Ian Booth) suggesting that mutations in OmpC33 are in part responsible for clinical antibiotic resistance.

Table 2.1.4.1. Minimum Inhibitory Concentrations of Antibiotics (µg / ml)

Strain	***Meropenem***	***Imipenem***	***Ciprofloxacin***	***Cefotaxime***	***Ceftazidime***
First clinical isolate (OmpC20)	0.062	0.25	1.0	0.5	0.5
First clinical isolate (OmpC20), *pOmpCWT*	0.031	0.25	1.0	0.125	0.5
Last clinical isolate (OmpC33)	2.0	4.0	8.0	32	64
Last clinical isolate (OmpC33), *pOmpCWT*	0.125	1.0	4.0	16	32

As the difference between OmpC20 and OmpC33 is only three residues, we wished to isolate the factor of OmpC porin and determine the role of mutation in the clinically observed resistance to the antibiotics.

2.2 Materials and methods

2.2.1 Expression of OmpC

The OmpC expression constructs were made by Professor Ian Booth, our collaborator, at the University of Aberdeen and Dr. Vicki Bamford who worked as a postdoc in our laboratory. The plasmid containing the variant *OmpC* genes were transformed into *OmpC* and *OmpF* minus *E. coli* HN705 cells (Sugawara and Nikaido, 1992).

The transformed HN705 cell cultures were stored in 10% glycerol at -80ºC. A small amount of cells were used to inoculate 10mL LB medium containing 30 µg / ml chloramphenicol and 0.5 % (w/v) glucose for inhibiting the LamB expression. For the growth of HN705 cells, no antibiotics were added during fermentation. Cells were grown at 37 °C and were harvested by centrifugation. To check the expression level of OmpC, 10-15µl intact cells were incubated with SDS at 100ºC for 15min and centrifuged to remove the unsolubilised cells before running the gel. Gels were run at 200V for 35mins in MES running buffer, pH 7.4, following the manufacturer's protocols (Invitrogen). Proteins were stained by Coomassie blue staining. Molecular weight values were estimated from the migration rates of Mark-12 markers (Invitrogen).

The intensity of the bands corresponding to OmpC protein was analyzed by the software ImageGauge V4.21. The corresponding bands were sent to Mass-Spec for the identity check.

2.2.2 MTT assay without antibiotics

2.2.2.1 Influence of cell numbers and the growth stage

MTT assay were carried out using a modified procedure for the Cell Growth Determination Kit (Sigma-Aldrich). MTT solution at concentration of 5mg/ml was directly from the manufacturer Sigma-Aldrich. Other solutions were from the manufacturer or made fresh in the lab and sterilised using 0.22μm membrane filter. To define the suitable concentration of cell culture reacting with MTT, cells at exponential phase (OD_{600} ~1.0)and stationary phase (OD_{600} ~2.0) were harvested, respectively. Cells were resuspended in sterilized phosphate buffered saline (PBS, pH 7.4) and were washed three times with PBS. A series of dilutions were made to give an OD_{600} value range of 0.1 to 1.0. The reaction took place at a cuvette (10mm wide) by adding 90 μl of resuspended cells along with 10 μl 5mg/ml MTT. After incubation for 4 hours at 20 ºC, 900 μl of 0.1N HCl (~36%, Fisher Scientific) dissolved in absolute isopropanol (99.9%, VWR International) was added to the cuvette to solubilise the formazans. Pipetting up and down was necessary to fully solubilise the formazans. The absorbance of each sample was measured at wavelength of 570 nm with the background absorbance at 690 nm subtracted. The solution for zeroing the background was 900μl 0.1N HCl dissolved in absolute isopropanol plus 100μl PBS solution. Each cell concentration was measured at least three times within an independent experiment.

2.2.2.2 Influence of added MTT amount

To measure the influence of the amount of MTT added to the cell culture, 5µl, 10µl, 15µl 5mg/ml MTT solution was added to 90µl cell culture, corresponding to ~5%, 10%, ~15% of the total reaction volume, respectively. Experiments were carried out triplicate at room temperature for 4 hours and following the protocol as described above.

2.2.2.3 Influence of cell viability

Cells at an OD_{600} 0.4 were killed by heating at 100 ºC for 1h. 10µl MTT solution was added to 90µl dead cell solutions and left at room temperature for reaction. MTT activity was checked by eye-observation after 24 hours.

2.2.2.4 Influence of incubation time with MTT

Cells growing to late exponential stage (OD_{600} ~1.0) were harvested and washed three times by PBS. Cells were diluted to give an OD_{600} 0.4. 10µl MTT solution was added to 90µl cell solutions and left at room temperature for reaction for a time period of 1h, 2h, 3h, 4h, 5h, 6h, 7h, 8h and 20h. Reading was recorded as described above.

2.2.3 MTT assay with antibiotics

2.2.3.1 The influence of antibiotic itself on MTT activity

Three antibiotics, gentamicin sulfate (Melford, UK), carbenicillin disodium (Melford, UK), cefotaxime sodium (Sigma, Germany) were tested for their reaction with MTT. Antibiotic solutions were made in PBS as 1M concentration as stock. The solutions were made fresh on the day of experiment. 10µl 5mg/ml MTT solution was added to 10µl antibiotic solutions along with 90µl PBS. The final concentration of antibiotics is approximately 100mM. After incubation for 4 hours at 20ºC, 890µl 0.1N HCl dissolved in isopropanol was added to the solution. Measurement was carried out using the spectrophotometer which used to measure the MTT activity with cells. The zeroing solution was 890µl 0.1N HCl dissolved in isopropanol plus 110µl PBS.

2.2.3.2 The control strain *E. coli* HN705

The metabolic activity of *E. coli* HN705 (*OmpC* and *OmpF* knocked out), was investigated by the MTT assay. Cells growing to the exponential stage and stationary stage were harvested, washed and diluted with PBS to give a series of OD value ranging from 0.1 to 1.0. The measurement was taken place as described in section 2.2.2.1.

2.2.3.3 MTT assay with antibiotics

Three antibiotics, gentamicin sulfate (Melford, UK), carbenicillin disodium (Melford, UK), cefotaxime sodium (Sigma, Germany), were tested for their cytotoxity to the cells of

HN705 transformed with OmpC20 (HN705-OmpC20) and cells of HN705 with OmpC33 (HN705-OmpC33), respectively. Cells were all grown to OD ~1.0 and harvested by centrifugation, washed with PBS three times and diluted into OD 0.4. Antibiotics dissolved in PBS at 1M stock were made fresh on the day of experiment or stored at -20^{o} C for future use.

We first tested a big range of antibiotic concentrations then zoom into a smaller scale for further tests. A series of 10µl antibiotic solutions along with 10µl 5mg/ml MTT were added to 90µl of resuspended cells. After 4 hours incubation at 20ºC the cells containing the resulting purple crystals were resuspended by addition of 890 µl of 0.1N HCl dissolved in isopropanol. The absorbance of each assay was measured at wavelength of 570 nm with the background absorbance at 690 nm subtracted. Each assay was performed at least with two independent experiments with each sample triplicate. The metabolic activity of cells without the addition of antibiotics was defined as 100%. After incubation with antibiotics, the metabolic activity of cells decreased. The metabolic inhibition rate is defined as the ratio of the amount of cell death to the total number of live cells. It is calculated from the 570nm absorbance mean value. For example, the mean value of 570nm absorbance of cells without any antibiotics is 0.8, the 570nm absorbance value of cells incubated with 25mM carbenicillin is 0.3, then by definition, the metabolic inhibition is (0.8-0.3)/0.8 *100%= 62.5%.

2.3 Results

2.3.1 OmpC expression

HN705 cells, the strain with *ompF* and *ompC* knocked out, was grown at the same LB medium as that for OmpC20 and OmpC33 cells but without antibiotics and glucose. HN705 cells were used as a control for the OmpC expression. Figure 2.3.1.1 shows the result of whole cell SDS-PAGE. It shows OmpC20 and OmpC33 are both expressed (indicated by the pointing arrow) with no significant difference on the expression level. Analysis by ImageGauge confirmed this observation with corresponding gel bands the same UV absorbance (indicated by the numbers listed). It is noticed that HN705 cells have a different expression pattern except for the OmpC protein (figure 2.3.1.1). The OmpC identity was confirmed by Mass-spec peptide mapping (data not shown).

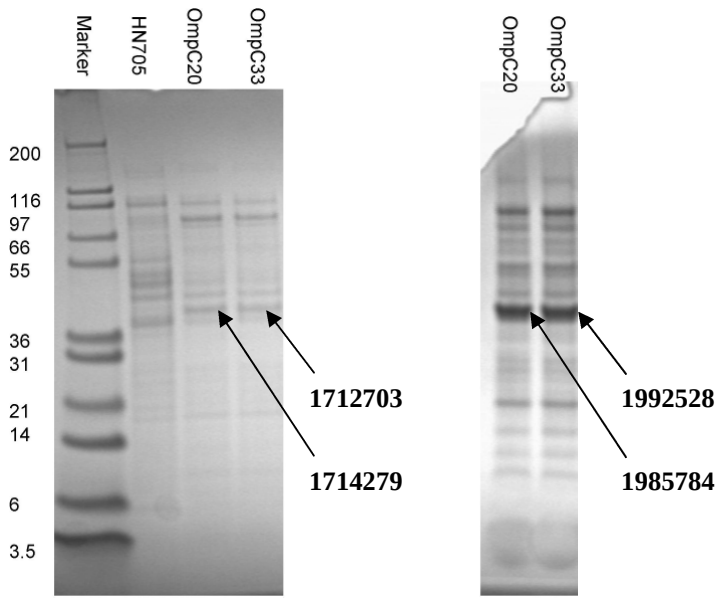

Figure 2.3.1.1 Comparison of expression level of OmpC20 and OmpC33 in HN705. Whole cells in two different batches were solubilized and analysed in separate gels (left, right). The lanes are marked as shown above the gel. The arrow indicates the location of OmpC which is absent in HN705 cells. The intensity of the corresponding bands were analysed by the software ImageGauge and the UV absorbance value was indicated.

2.3.2 MTT assay without antibiotics

2.3.2.1 Influence of cell numbers and growth stage

With a defined concentration, MTT must have a maximum ability to act on the cells. To find out the suitable cell concentration, a series of dilution from the concentrated cell culture were made and tested. Table 2.3.2.1a shows the MTT formazan absorbance from OmpC20 and OmpC33 exponential stage cells. Each reaction carried out at individual cuvette, the measured value at 570nm subtracting the measured value at 690nm is to exclude the difference factor of cuvette absorbance. It was noticed that at 690nm the absorbance value were negative, this was because the zeroing solution had a higher absorbance at 690nm. We define real 570nm absorbance value by the following equation:

Real 570nm absorbance = Measured 570nm absorbance – measured 690nm absorbance

We plotted the real 570nm absorbance against the cell OD_{600} values. Figure 2.3.2.1a shows the effect of cell numbers on the 570nm absorbance corresponding to the MTT reduction activity. It suggests before OD_{600} 0.4, the cell number dominates while after OD_{600} 0.4, MTT reaches its saturation level as a higher number of cells do not result in relatively higher activity.

In a similar manner, Table 2.3.2.1b shows the absorbance measured for OmpC20 and OmpC33 cells harvested from the stationary phase. Figure 2.3.2.1b showed a similar trend of 570nm absorbance values verses the cell numbers. The two independent experiments conclude that the best cell concentration reacting with 10µl 5mg/ml MTT is at OD_{600} 0.4.

OmpC20

OD_{600} value	570nm			690nm			570-690nm			570-690nm mean	error
0.1	0.157	0.158	0.158	-0.113	-0.108	-0.11	0.27	0.266	0.268	0.268	0.001
0.2	0.397	0.424	0.363	-0.073	-0.067	-0.11	0.47	0.491	0.473	0.478	0.006
0.3	0.513	0.525	0.489	-0.101	-0.065	-0.08	0.614	0.59	0.569	0.591	0.013
0.4	0.519	0.52	0.493	-0.062	-0.056	-0.074	0.581	0.576	0.567	0.574	0.004
0.5	0.467	0.452	0.463	-0.082	-0.096	-0.084	0.549	0.548	0.547	0.548	0.001
0.6	0.443	0.464	0.41	-0.078	-0.063	-0.099	0.521	0.527	0.509	0.519	0.005
0.7	0.448	0.454	0.41	-0.06	-0.078	-0.078	0.508	0.532	0.488	0.509	0.012
0.8	0.486	0.439	0.367	-0.046	-0.057	-0.074	0.532	0.496	0.441	0.489	0.026
1	0.474	0.458	0.476	-0.066	-0.073	-0.061	0.54	0.531	0.537	0.536	0.003

OmpC33

OD_{600} value	570nm			690nm			570-690nm			570-690nm mean	error
0.1	0.147	0.172	0.136	-0.094	-0.078	-0.106	0.241	0.25	0.242	0.244	0.003
0.2	0.383	0.317	0.352	-0.091	-0.111	-0.066	0.474	0.428	0.418	0.440	0.017
0.3	0.55	0.523	0.544	-0.089	-0.095	-0.081	0.639	0.618	0.625	0.627	0.006
0.4	0.556	0.599	0.604	-0.091	-0.088	-0.082	0.647	0.687	0.686	0.673	0.013
0.5	0.621	0.625	0.653	-0.046	-0.058	-0.061	0.667	0.683	0.714	0.688	0.014
0.6	0.63	0.598	0.645	-0.058	-0.086	-0.058	0.688	0.684	0.703	0.691	0.006
0.7	0.622	0.687	0.653	-0.081	0.011	-0.058	0.703	0.676	0.711	0.696	0.010
0.8	0.634	0.632	0.626	-0.048	-0.047	-0.065	0.682	0.679	0.691	0.684	0.004
1	0.638	0.59	0.591	-0.063	-0.055	-0.06	0.701	0.645	0.651	0.665	0.018

Table 2.3.2.1a Absorbance values for exponential stage OmpC20 and OmpC33 cells at varied concentration.

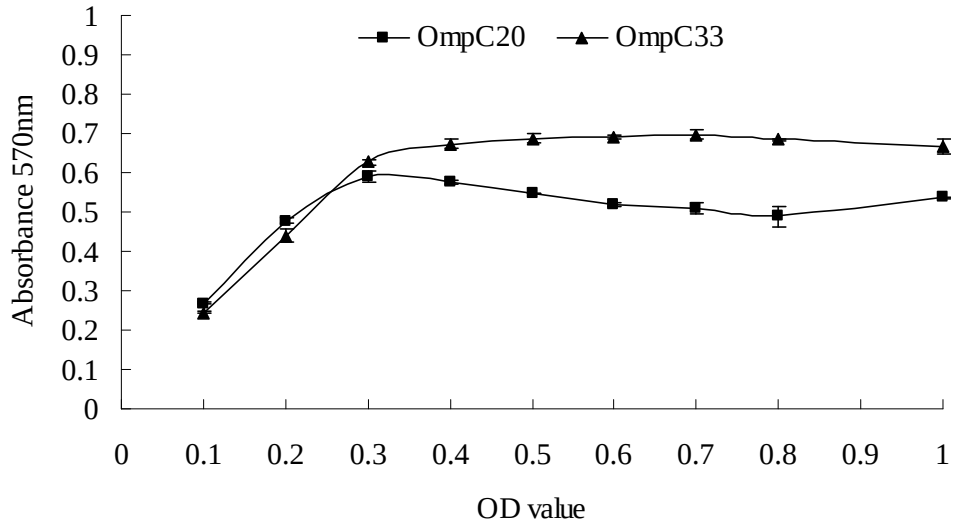

Figure 2.3.2.1a Influence of cell numbers on the absorbance measurement. OmpC20 and OmpC33 cells were growing at identical conditions to exponential phase (OD_{600} ~1.0). Sample was triplicate and standard (ST) error was indicated.

OmpC20											
OD_{600} value	570nm			690nm			570-690nm			570-690nm mean	error
0.1	0.044	0.059	0.033	-0.057	-0.037	-0.062	0.101	0.096	0.095	0.097	0.002
0.2	0.088	0.089	0.069	-0.05	-0.045	-0.067	0.138	0.134	0.136	0.136	0.001
0.3	0.11	0.122	0.118	-0.042	-0.048	-0.048	0.152	0.17	0.166	0.162	0.005
0.4	0.157	0.136	0.16	-0.044	-0.041	-0.02	0.201	0.177	0.18	0.186	0.007
0.5	0.163	0.16	0.175	-0.007	-0.021	-0.008	0.17	0.181	0.183	0.178	0.004
0.6	0.154	0.189	0.191	-0.003	-0.003	0.001	0.157	0.192	0.19	0.179	0.011
0.7	0.148	0.144	0.169	-0.02	-0.036	0.003	0.168	0.18	0.166	0.171	0.004
0.8	0.16	0.172	0.167	-0.022	-0.008	-0.011	0.182	0.18	0.178	0.18	0.001
1	0.351	0.305	0.3	0.061	0.017	-0.001	0.29	0.288	0.301	0.293	0.004
OmpC33											
OD_{600} value	570nm			690nm			570-690nm			570-690nm mean	error
0.1	0.098	0.087	0.112	-0.035	-0.06	-0.03	0.133	0.147	0.142	0.141	0.004
0.2	0.169	0.178	0.191	-0.046	-0.045	-0.023	0.215	0.223	0.214	0.217	0.002
0.3	0.249	0.249	0.274	-0.043	-0.043	-0.015	0.292	0.292	0.289	0.291	0.001
0.4	0.425	0.442	0.415	-0.004	0.002	-0.024	0.429	0.44	0.439	0.436	0.003
0.5	0.388	0.417	0.436	-0.041	-0.024	-0.01	0.429	0.441	0.446	0.438	0.005
0.6	0.425	0.426	0.427	-0.038	-0.014	-0.015	0.463	0.44	0.442	0.448	0.007
0.7	0.433	0.432	0.509	0.015	-0.009	0.019	0.418	0.441	0.49	0.449	0.021
0.8	0.422	0.433	0.433	-0.011	-0.002	-0.007	0.433	0.435	0.44	0.436	0.002
1	0.435	0.451	0.466	0.005	0.029	0.032	0.43	0.422	0.434	0.428	0.003

Table 2.3.2.1b Absorbance values for stationary phase OmpC20 and OmpC33 cells at varied concentration.

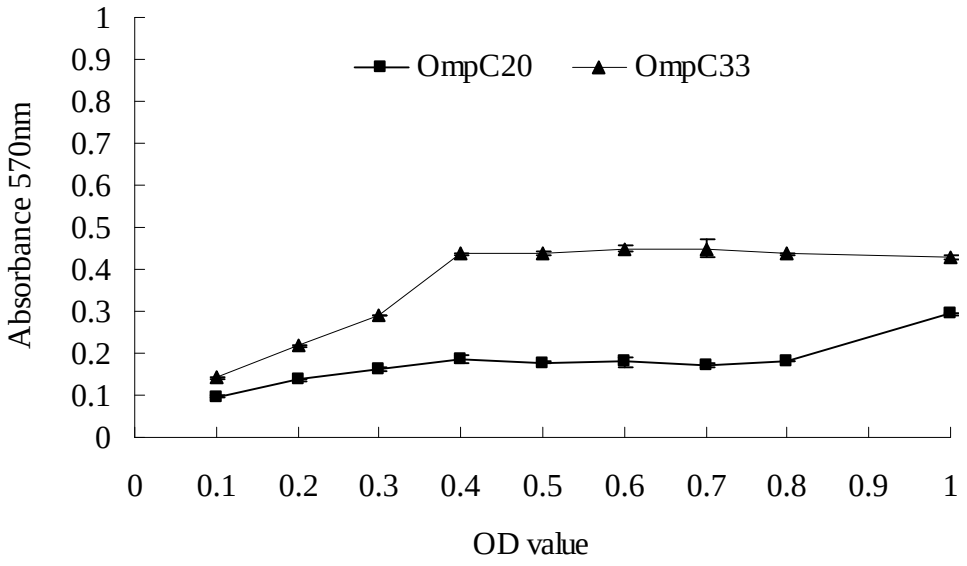

Figure 2.3.2.1b Influence of cell numbers on the absorbance measurement. OmpC20 and OmpC33 cells were grown at identical conditions to stationary phase. Experiments were done at least three times and standard error indicated.

It was noticed that cells at exponential stage have higher MTT activity than those from stationary phase, both for OmpC20 and OmpC33. During exponential stage, these two types of cells had similar activity, while at stationary stage, OmpC33 cells had higher activity than OmpC20 cells.

2.3.2.2 Influence of MTT amount

With a defined cell numbers, the influence of MTT amount added to the cell culture was studied with OmpC20 and OmpC33 cells grown to the exponential stage. Table 2.3.2.2 shows the absorbance value with different OD_{600} values when three different MTT

amounts were added to the solution. Figure 2.3.2.2 shows the results for OmpC20 and OmpC33 cells with three different OD_{600} values 0.3, 0.4, 0.5, respectively. It is shown that MTT added at a scale of 10% of the total solution (10µl) has its optimum activity with the cells. At a scale of 5% MTT (5µl) added to the cell culture at OD_{600} 0.3, 0.4, 0.5, the measured metabolic activity remained the same even though the cell numbers varied that varied metabolic activities would be expected. This implied that at this low MTT concentration all the MTT is consumed only by a portion of live cells, therefore at this MTT concentration, the metabolic activity does not correlate to the true cell numbers.

OmpC20												
OD_{600} value	MTT 5mg/ml	570nm			690nm			570-690nm			570-690nm mean	error
0.3	5ul	0.203	0.151	0.134	-0.051	-0.085	-0.07	0.254	0.236	0.204	0.231	0.014
0.4	5ul	0.13	0.131	0.063	-0.089	-0.088	-0.093	0.219	0.219	0.156	0.198	0.021
0.5	5ul	0.121	0.122	0.092	-0.096	-0.07	-0.074	0.217	0.192	0.166	0.191	0.014
0.3	10ul	0.48	0.491	0.49	-0.064	-0.091	-0.076	0.544	0.582	0.566	0.564	0.011
0.4	10ul	0.577	0.509	0.638	-0.082	-0.096	-0.067	0.659	0.605	0.705	0.656	0.028
0.5	10ul	0.669	0.741	0.625	-0.092	-0.044	-0.063	0.761	0.785	0.688	0.744	0.029
0.3	15ul	0.493	0.515	0.52	-0.054	-0.059	-0.066	0.547	0.574	0.586	0.569	0.011
0.4	15ul	0.697	0.731	0.709	-0.077	-0.068	-0.073	0.774	0.799	0.782	0.785	0.007
0.5	15ul	0.915	0.93	1.003	-0.037	-0.044	-0.053	0.952	0.974	1.056	0.994	0.031
OmpC33												
OD_{600} value	MTT 5mg/ml	570nm			690nm			570-690nm			570nm-690nm mean	Error
0.3	5ul	0.337	0.311	0.338	-0.085	-0.102	-0.078	0.422	0.413	0.416	0.417	0.002
0.4	5ul	0.37	0.347	0.359	-0.052	-0.057	-0.055	0.422	0.404	0.414	0.413	0.005
0.5	5ul	0.334	0.393	0.427	-0.083	-0.087	-0.058	0.417	0.48	0.485	0.460	0.021
0.3	10ul	0.59	0.58	0.528	-0.097	-0.06	-0.077	0.687	0.64	0.605	0.644	0.023
0.4	10ul	0.68	0.764	0.584	-0.083	-0.086	-0.084	0.763	0.85	0.668	0.760	0.052
0.5	10ul	0.854	0.871	0.904	-0.046	-0.041	-0.054	0.9	0.912	0.958	0.923	0.017
0.3	15ul	0.522	0.572	0.501	-0.077	-0.066	-0.094	0.599	0.638	0.595	0.610	0.013
0.4	15ul	0.618	0.679	0.768	-0.085	-0.078	-0.082	0.703	0.757	0.85	0.77	0.042
0.5	15ul	0.815	0.941	0.946	-0.094	-0.039	-0.064	0.909	0.98	1.01	0.966	0.030

Table 2.3.2.2 Influence of added MTT amount to the absorbance measurement. Cells were harvested from the exponential growth stage.

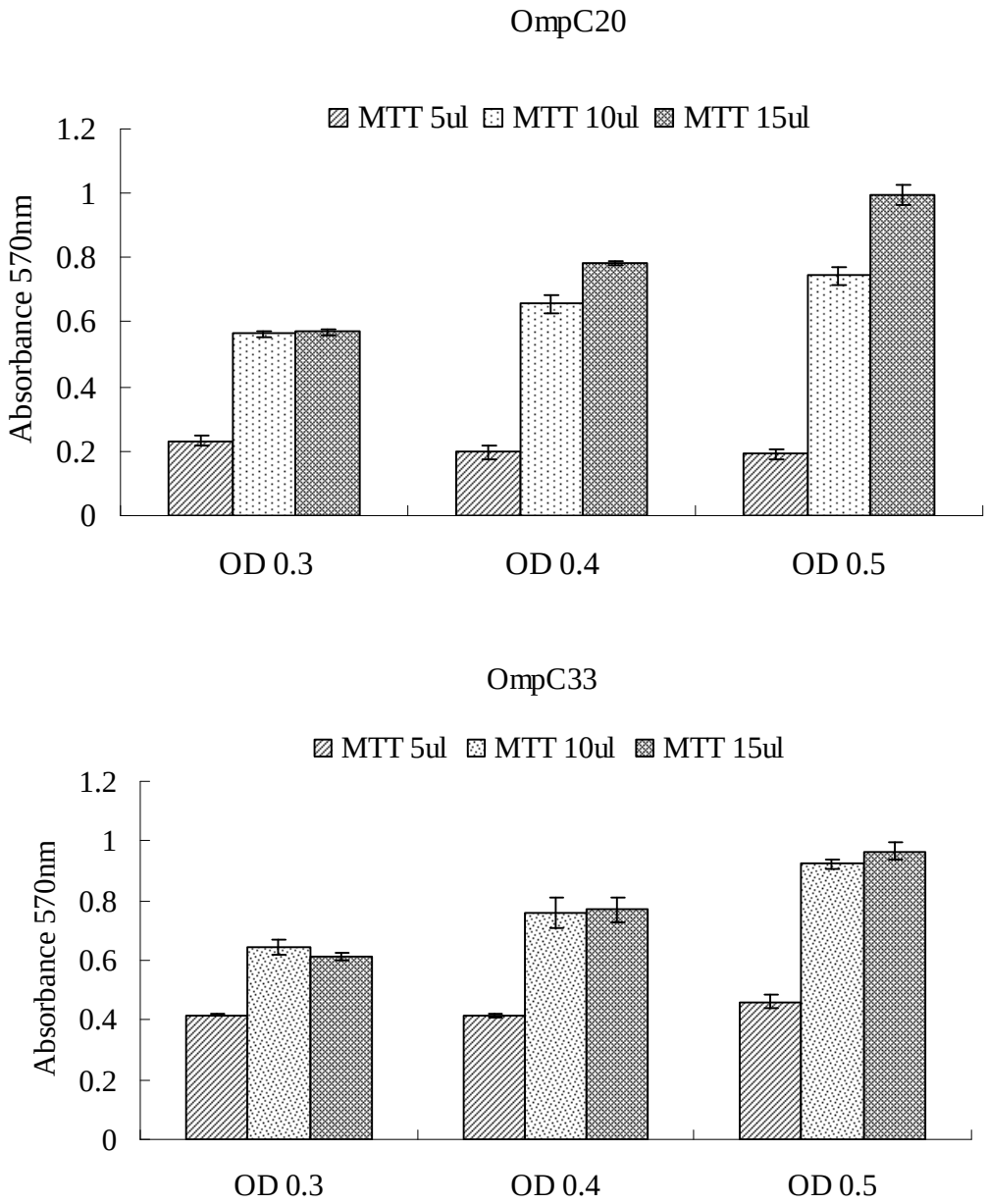

Figure 2.3.2.2 Influence of the amount of MTT added to the cell culture. OmpC20 and OmpC33 cells were growing to the exponential stage. Cells were diluted to give an OD 0.3, 0.4 and 0.5. MTT solution at the concentration of 5mg/ml was added to the cell solution at a volume of 5µl, 10µl, 15µl.

2.3.2.3 Dead cells do not react with MTT.

No visible reaction took place with the dead cells incubated with MTT after 24 hours. Figure 2.3.2.5 shows the comparable results of dead cells and live cells incubated with MTT. It is clear that dead cells do not react with MTT as no visible color change of the solution.

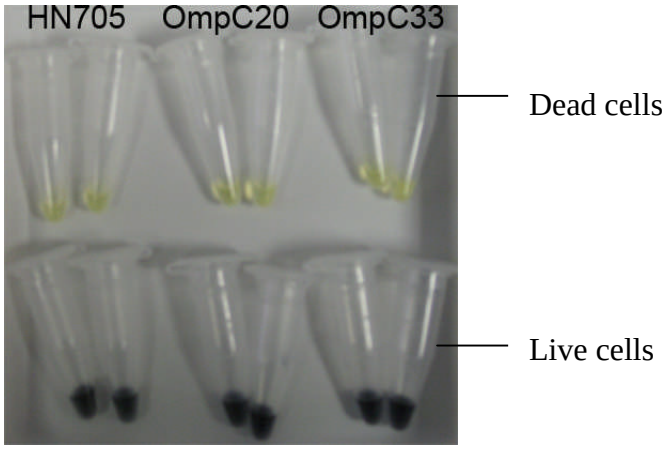

Figure 2.3.2.3 The difference of live cells (bottom layer) and dead cells (top layer) reacting with MTT. Live cells reacted with MTT resulting blue-magenta colored formazan. Dead cells did not react with MTT as the reaction solution didn't change the color.

2.3.2.4 Influence of incubation time

It is believed that MTT reduction to its formazan occurs inside the cell (Vistica et al., 1991). Since the production of formazan would be time-dependent, we wished to examine the effect of incubation time on the formazan production level. Table 2.3.2.4 shows the absorbance values measured at different time points. Figure 2.3.2.4 shows that at the first 5 hours of incubation, the MTT formazan production is almost linear like an exponential

stage. After 5-6h of incubation, the MTT formazan production reached its saturation level as longer incubation time does not result in much higher MTT formazan.

OmpC20

Incubation time (h)		570nm			690nm			570-690nm		mean	ST error
1	0.228	0.232	0.217	-0.028	-0.027	-0.027	0.256	0.259	0.244	0.253	0.004
2	0.493	0.507	0.545	-0.007	-0.004	0.023	0.5	0.511	0.522	0.511	0.006
3	0.697	0.669	0.712	0.052	0.024	0.035	0.645	0.645	0.677	0.655	0.010
4	0.724	0.728	0.768	0.025	0.017	0.017	0.699	0.711	0.751	0.720	0.015
5	0.891	0.902	0.946	0.035	0.066	0.083	0.856	0.836	0.863	0.851	0.008
6	0.864	0.903	0.905	0.024	0.048	0.042	0.84	0.855	0.863	0.852	0.006
7	0.891	0.918	0.903	0.03	0.017	0.032	0.861	0.901	0.871	0.877	0.012
8	0.883	0.906	0.891	-0.012	0.013	0.049	0.895	0.893	0.842	0.876	0.017
20	0.787	0.836	0.874	-0.035	-0.029	-0.028	0.822	0.865	0.902	0.863	0.023

OmpC33

Incubation time (h)		570nm			690nm			570-690nm		mean	ST error
1	0.339	0.374	0.342	-0.025	0.005	-0.028	0.364	0.369	0.37	0.367	0.001
2	0.585	0.606	0.57	0.005	0.03	0.01	0.58	0.576	0.56	0.572	0.006
3	0.759	0.777	0.743	0.049	0.05	0.027	0.71	0.727	0.716	0.717	0.004
4	0.873	0.797	0.804	0.053	0.025	0.041	0.82	0.772	0.763	0.785	0.017
5	0.893	0.902	0.847	0.052	0.067	0.025	0.841	0.835	0.822	0.832	0.005
6	0.888	0.865	0.86	0.018	0.046	0.014	0.87	0.819	0.846	0.845	0.014
7	0.916	0.907	0.908	0.025	0.016	0.024	0.891	0.891	0.884	0.888	0.002
8	0.915	0.894	0.886	0.029	0.011	-0.005	0.886	0.883	0.891	0.886	0.002
20	0.876	0.868	0.836	-0.005	-0.008	-0.027	0.881	0.876	0.863	0.873	0.005

Table 2.3.2.4 Influence of incubation time to the absorbance measurement. Cells were harvested from the exponential growth stage.

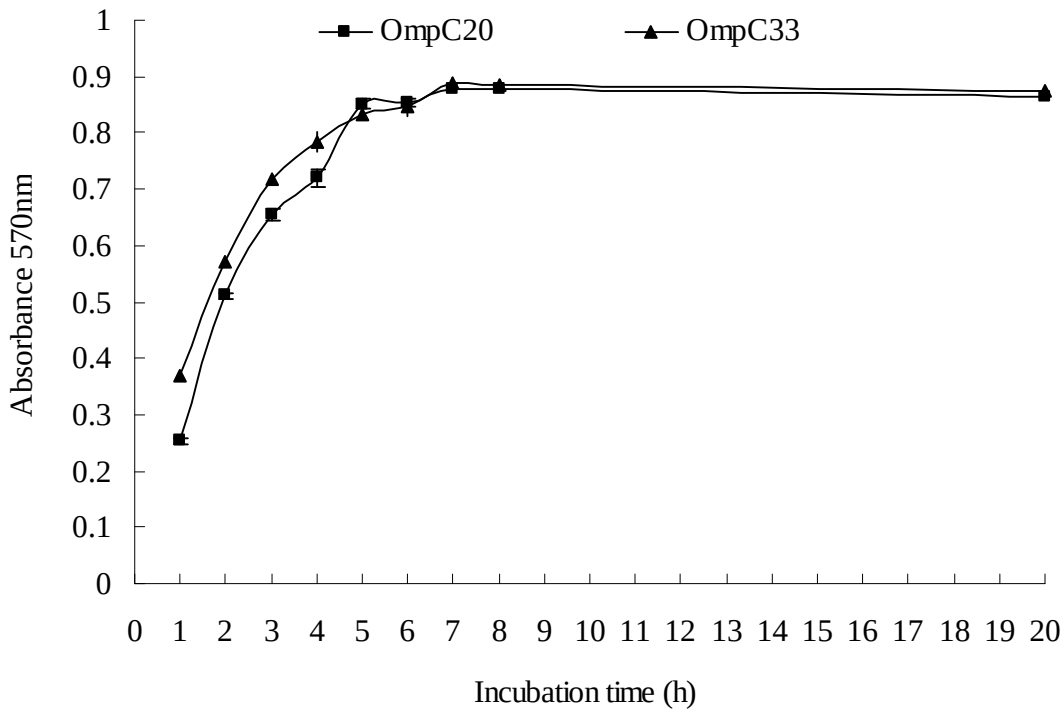

Figure 2.3.2.4 Influence of incubation time on the absorbance measurement of OmpC20 and OmpC33 that were harvested at the exponential stage. Errors were indicated as bars.

2.3.3 MTT assay with antibiotics

2.3.3.1 The effect of antibiotics on MTT

As a control experiment, we wished to investigate whether the drug itself reacted with MTT. Within the time of incubation (4h), there was no noticeable change. Table 2.3.3.1 shows the absorbance values measured for the three antibiotics tested. It is seen that the absorbance value change was minor, therefore the antibiotics have a neglectable effect on MTT.

Table 2.3.3.1 Effect of antibiotics on MTT

		570nm	690nm	570-690nm
0h	Gentamicin	0.134	0.087	0.047
	Carbenicillin	0.008	-0.004	0.012
	Cefotaxime	0.013	-0.002	0.015
4h	Gentamicin	0.093	0.09	0.003
	Carbenicillin	0.065	0.039	0.026
	Cefotaxime	0.02	0.005	0.015

2.3.3.2 The control strain HN705

As shown in figure 2.3.2.3, live cells of HN705 cells also reacted with MTT. This confirms that MTT can enter HN705 cells via pathway. To further quantify the metabolic activity of HN705 cells on MTT, the effect of cell numbers and the growth stages of HN705 was investigated. Figure 2.3.3.2 shows the effect of cell numbers and growth stage on the 570nm absorbance. As with OmpC20/33 cells, the exponential stage cells have higher activity than those from stationary stage cells. However, it does not show a saturation concentration with MTT as a higher number of cells result in higher value of absorbance.

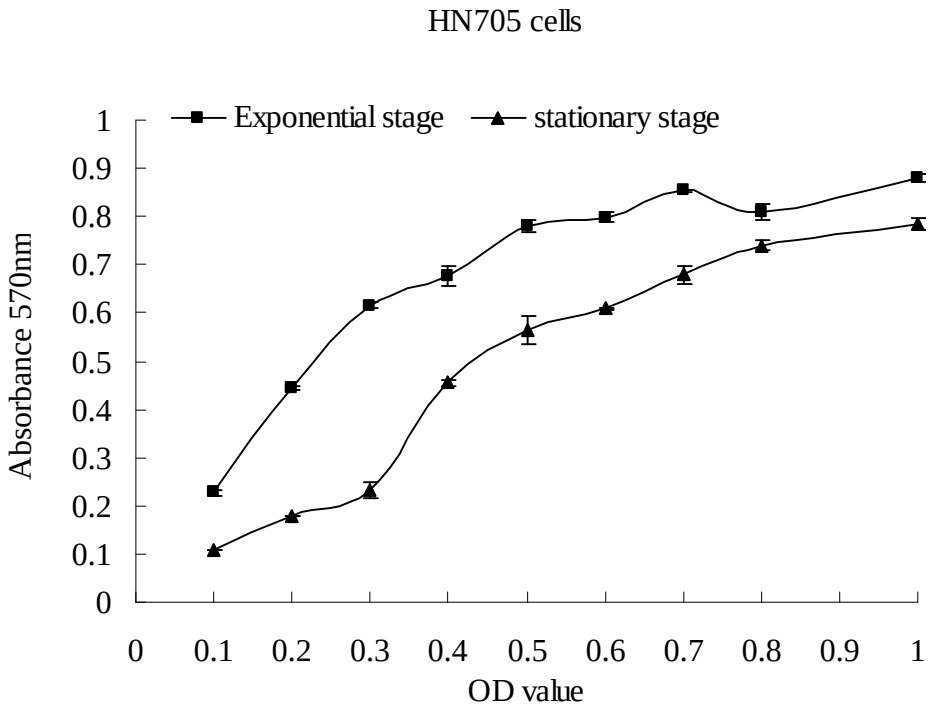

Figure 2.3.3.2 The effect of growth stage and cells numbers on the metabolic activity of HN705 cells.

2.3.3.3 MTT assay with three antibiotics

The antibiotic concentration was critical as at too high concentrations almost no cells would be expected to survive and at too low concentrations no cells would die. To verify this assumption, a series of concentrations for each antibiotic has to be tested to find out the effective range. Figure 2.3.3.3a shows the effect of antibiotic concentration on the cell metabolic activities. For all the antibiotics tested, cells have high metabolic activities at low antibiotics concentrations as the metabolic inhibition is close to zero. The metabolic inhibition rate increased along with the increase of antibiotic concentrations. In the case of

gentamicin, very high concentrations (100mM, 200mM) kill the cells as the metabolic inhibition rate is close to 100%. However, with the case of carbenicllin and cefotaxime, very high concentration still results in cell metabolic activities. This indicates that the uptake of these two antibiotics the cells is time-dependent. This initial test give indications that the effective concentration range for gentamicin was around ~100 μM, for carbenicillin was around 50mM, while for cefotaxime was >10mM.

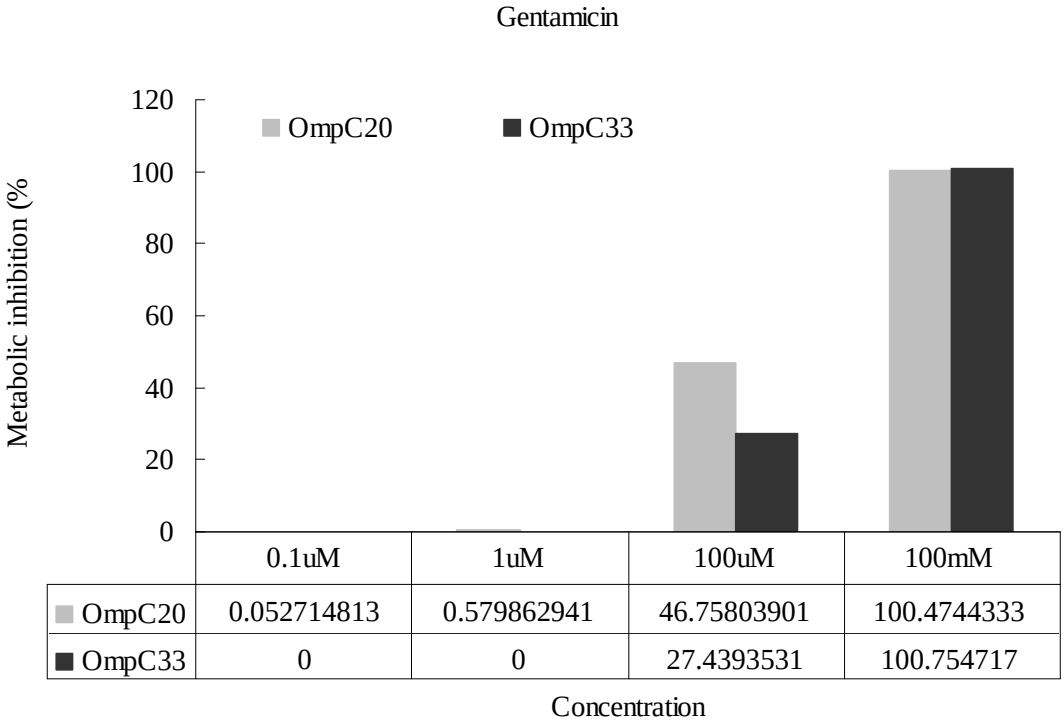

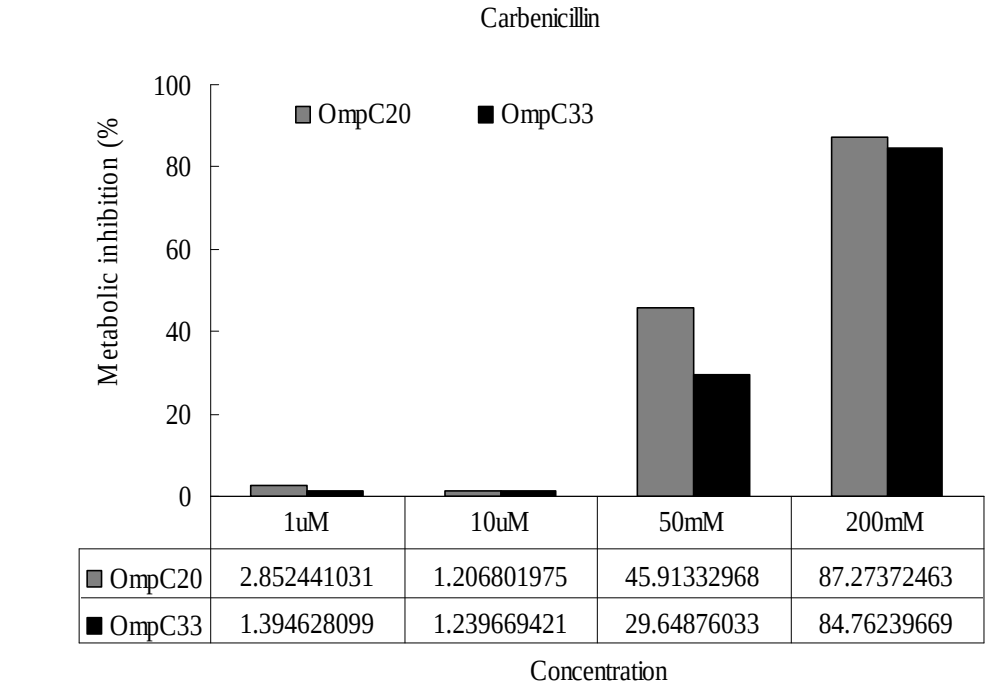

	1uM	10uM	50mM	200mM
OmpC20	2.852441031	1.206801975	45.91332968	87.27372463
OmpC33	1.394628099	1.239669421	29.64876033	84.76239669

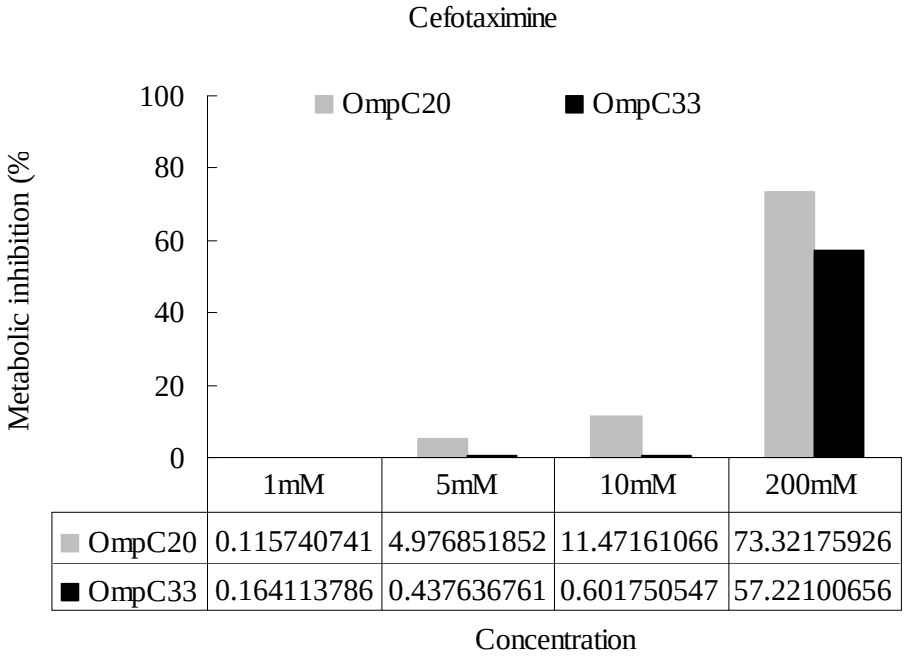

	1mM	5mM	10mM	200mM
OmpC20	0.115740741	4.976851852	11.47161066	73.32175926
OmpC33	0.164113786	0.437636761	0.601750547	57.22100656

Figure 2.3.3.3a The effect of antibiotic concentration on the metabolic activity of HN705 cells expressing OmpC20 and HN705 cells expressing OmpC33. The metabolic inhibition rate under each antibiotic concentration is listed on the table underneath the figure.

To further compare the cells' ability for the uptake of antibiotics, we tested the cells incubated with a series of intermediate antibiotic concentrations. Figure 2.3.3.3b shows the extent of metabolic inhibition rate of HN705 expressing OmpC20 and OmpC33 in the presence of three antibiotics: gentamicin, carbenicillin and cefotaxime, from two independent experiments. For all the tested antibiotics, HN705 cells expressing OmpC33 showed reproducibly lower metabolic inhibition rate (less antibiotic uptaking) than cells expressing OmpC20, consistent with other data that shows antibiotic resistance by OmpC33.

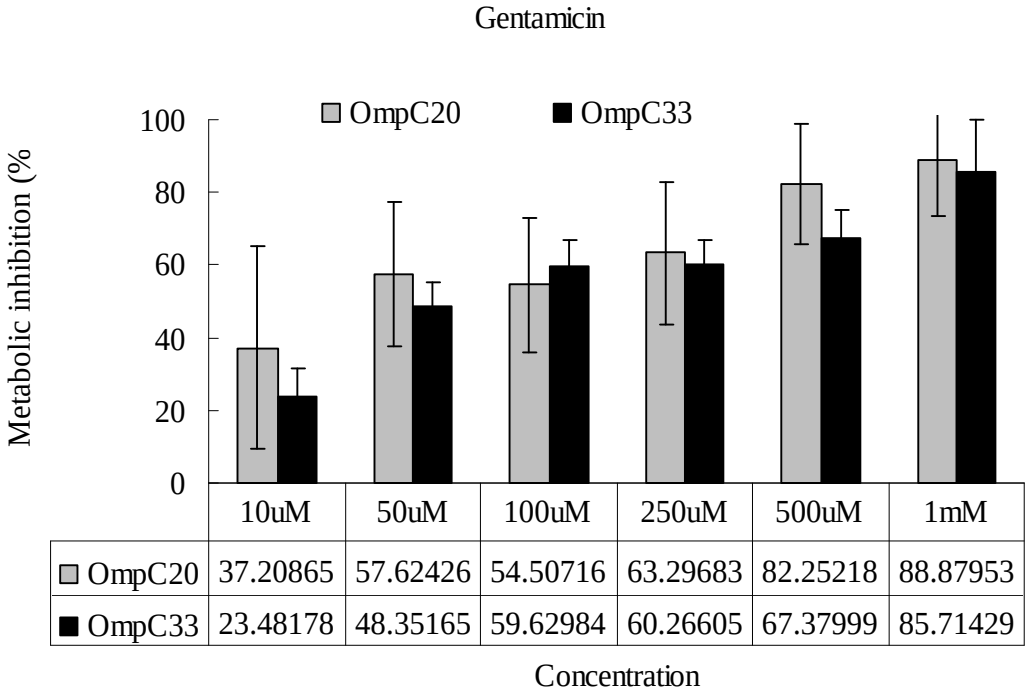

	10uM	50uM	100uM	250uM	500uM	1mM
OmpC20	37.20865	57.62426	54.50716	63.29683	82.25218	88.87953
OmpC33	23.48178	48.35165	59.62984	60.26605	67.37999	85.71429

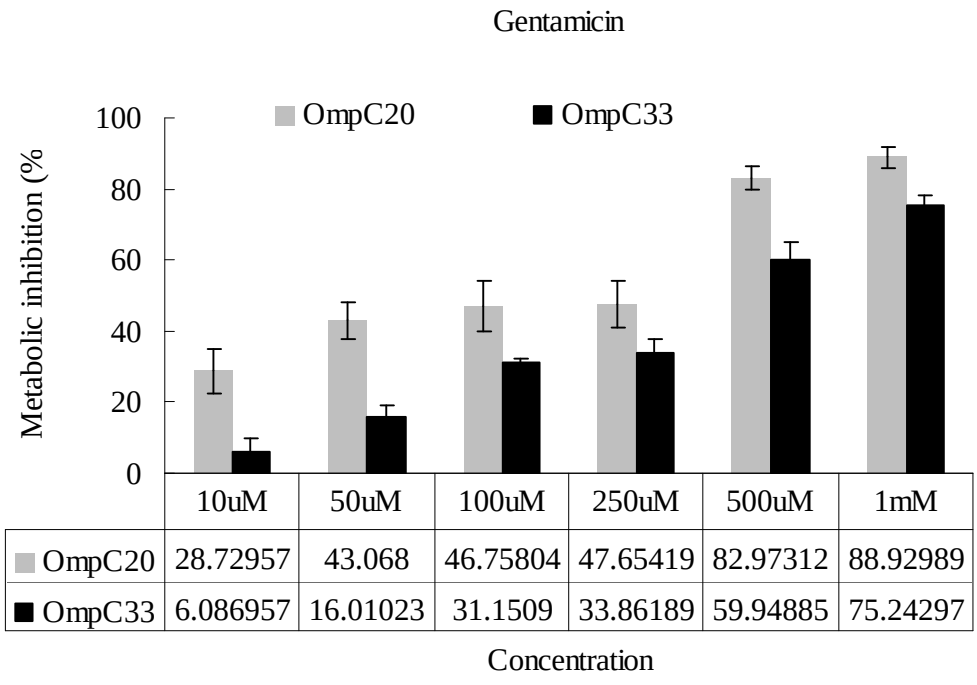

	10uM	50uM	100uM	250uM	500uM	1mM
OmpC20	28.72957	43.068	46.75804	47.65419	82.97312	88.92989
OmpC33	6.086957	16.01023	31.1509	33.86189	59.94885	75.24297

(Figure continues)

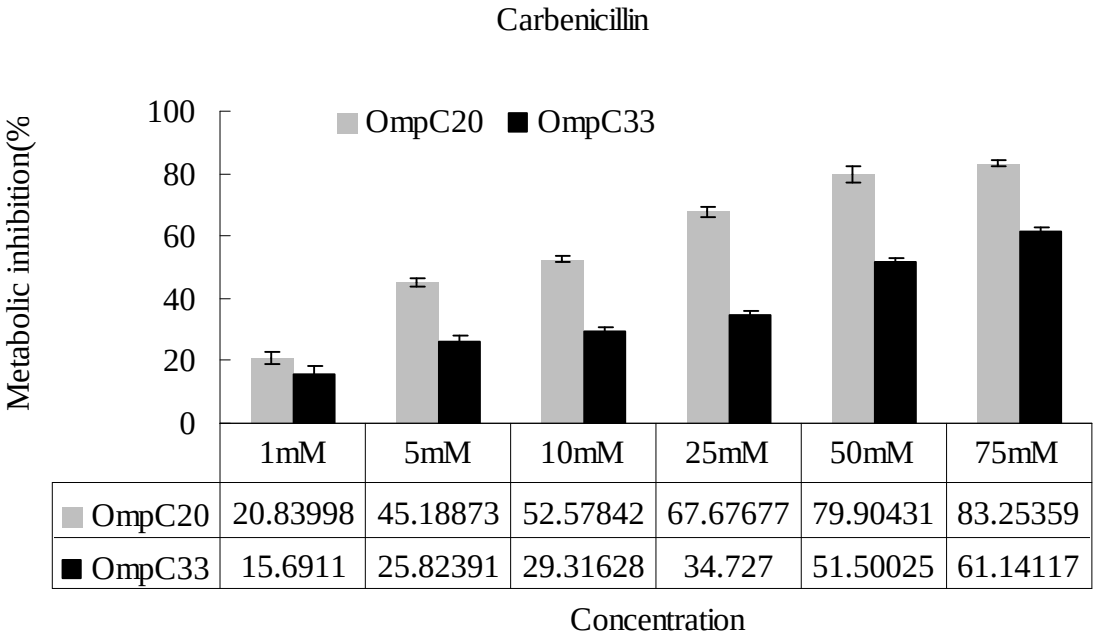

	1mM	5mM	10mM	25mM	50mM	75mM
OmpC20	20.83998	45.18873	52.57842	67.67677	79.90431	83.25359
OmpC33	15.6911	25.82391	29.31628	34.727	51.50025	61.14117

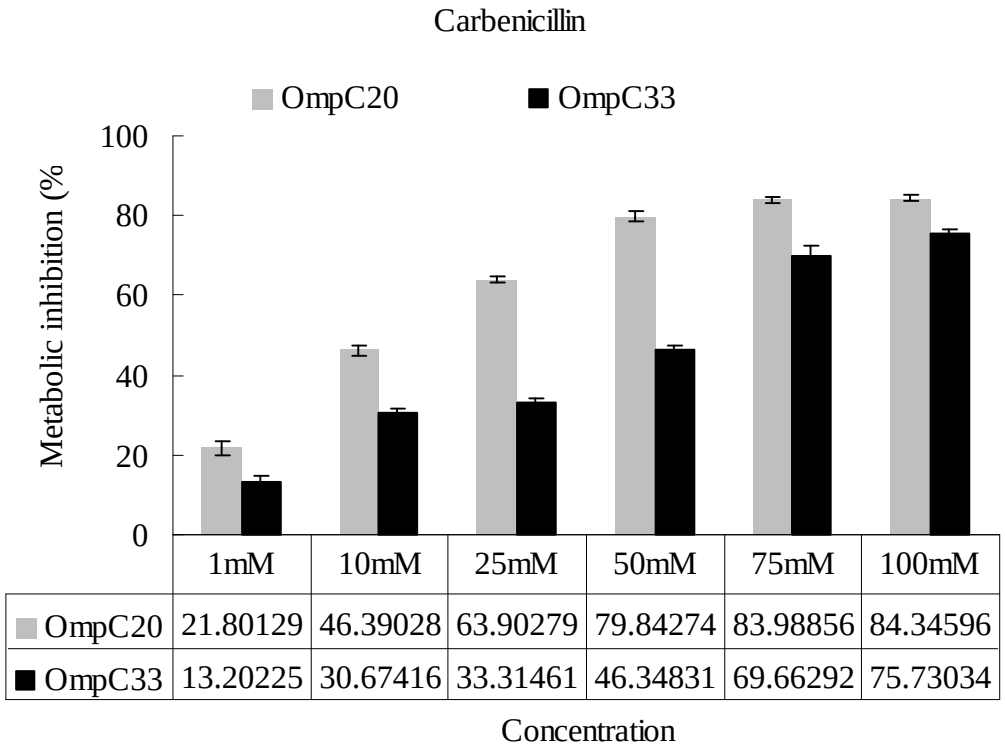

	1mM	10mM	25mM	50mM	75mM	100mM
OmpC20	21.80129	46.39028	63.90279	79.84274	83.98856	84.34596
OmpC33	13.20225	30.67416	33.31461	46.34831	69.66292	75.73034

(Figure continues)

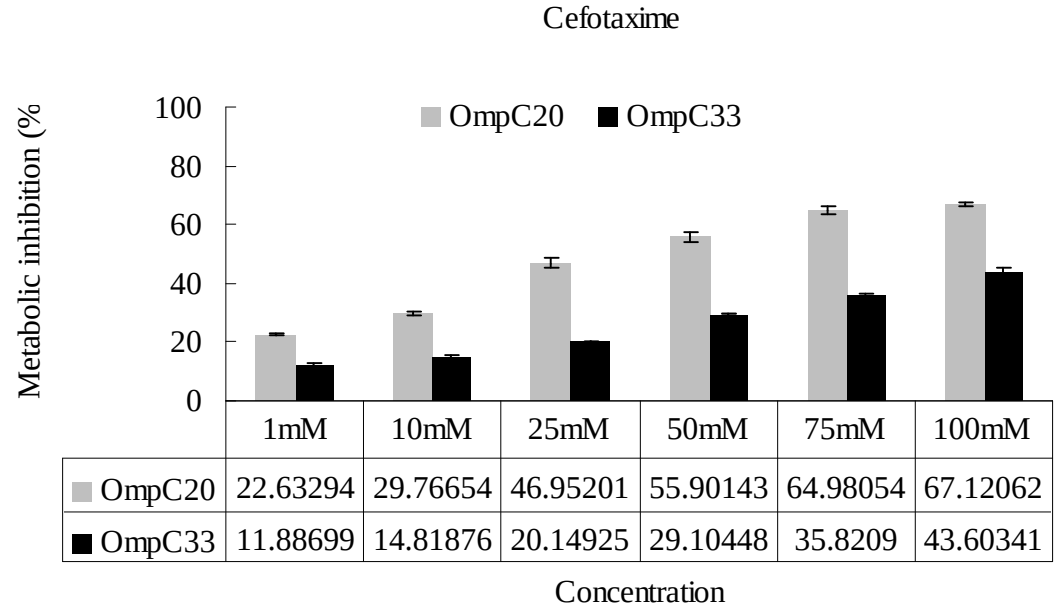

	1mM	10mM	25mM	50mM	75mM	100mM
OmpC20	22.63294	29.76654	46.95201	55.90143	64.98054	67.12062
OmpC33	11.88699	14.81876	20.14925	29.10448	35.8209	43.60341

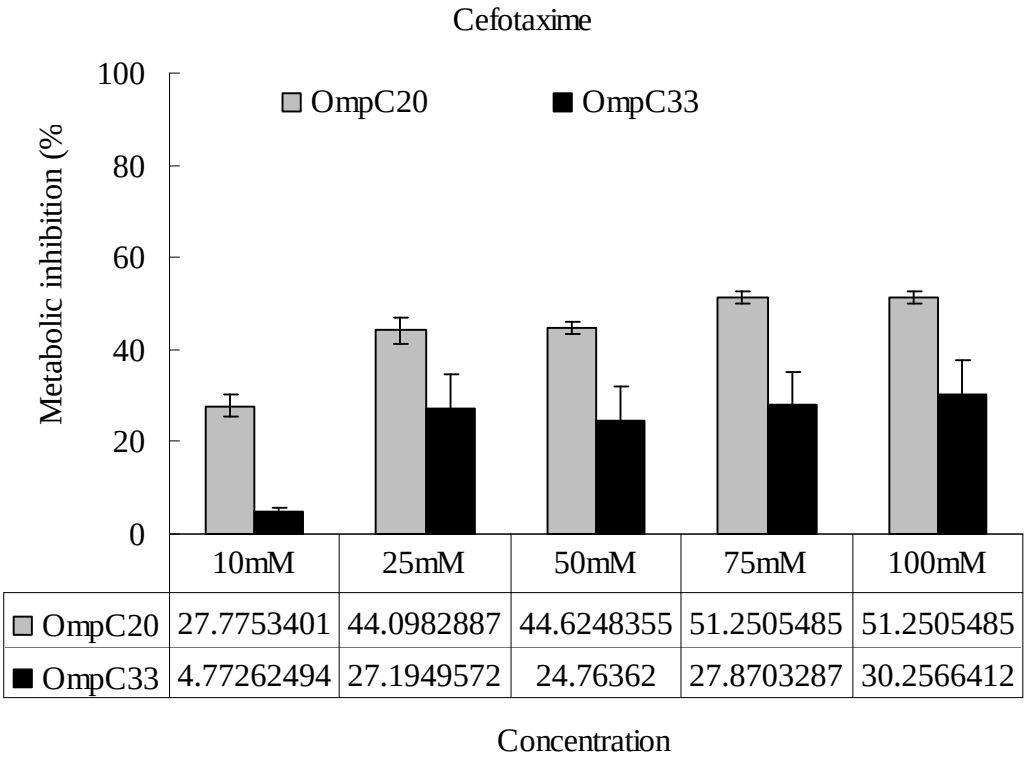

	10mM	25mM	50mM	75mM	100mM
OmpC20	27.7753401	44.0982887	44.6248355	51.2505485	51.2505485
OmpC33	4.77262494	27.1949572	24.76362	27.8703287	30.2566412

Figure 2.3.3.3b. The effect of antibiotic concentration on the metabolic activity of HN705 cells that express OmpC20 and OmpC33 respectively. A bar chart showing the extent of

metabolic inhibition in HN705 cells expressing OmpC20 and OmpC33 in the presence of antibiotics as indicated. Error bars are shown at their standard deviations.

2.4 Discussion and future work

The MTT assay has long been applied to test the metabolic activity of live cells since the first report from Mosmann (Mosmann, 1983). Growing bacterial cells go through several stages. Namely, lag phase when no obvious cell growth occurs and the metabolic activity is low; log phase (also termed as exponential phase) when cells are actively reproducing and the metabolic activity is most intense; stationary phase when the reproduction rate slows and so does the metabolic activity. After stationary phase, the bacterial cell population starts to shrink due to lack of nutrients. As the MTT assay measures the integrated metabolic activities of cells (Berridge et al., 2005), different MTT reduction activity would be expected from the different growth stage cells. In this study, it is confirmed that cells at exponential stage are more metabolic active than at stationary stage both for HN705-OmpC20 and HN705-OmpC33. Under the identical growth conditions, the gross metabolic activities at the exponential stage are similar for both HN705-OmpC20 and HN705-OmpC33 cells as the MTT formazan production are nearly identical. This indicates that the mutations on OmpC do not change the cell metabolic activity.

The MTT assay with antibiotics uses a defined cell line and is designed to isolate the changes in OmpC from other changes that are found in the clinical isolates. The assay establishes that mutations between OmpC20 and OmpC33 do contribute to increasing antibiotic resistance. This supports the initial proposal that the mutations in OmpC do alter

membrane permeability (Low et al., 2001). OmpC33, the last mutant to be isolated clearly restricts the uptake of antibiotics when compared to OmpC20. The clear cut nature of this result is surprising since there are only three residues differences between the proteins. The concentration of both β-lactams (~mM) is higher than gentamicin (μM) in order to get results comparable. This might be because besides the porin pathway, gentamicin also enters cell via a self-promoted pathway (Delcour, 2003) through the membrane. Gentamicin therefore kills the cell faster than those two β-lactams.

Clinical (as opposed to laboratory) antibiotic resistance is a complex process in which numerous factors contribute. The clinical strains referred to in this study, in addition to changes in OmpC sequence, exhibited progressively increased levels of β-lactamase expression with lower levels of OmpC expression (Low et al., 2001). Translocation across the outer membrane is the first and crucial step for Gram-negative bacteriocidal activity for any antibiotic. Many, but not all, antibiotics enter the cell via the outer membrane porin family which are responsible for small ion and nutrient flow though the outer membrane. Bacteria with multiple porin species may have an ecological advantage; loss of only one porin would allow the other porins to compensate in terms of nutrient flow but would remove the target site for phages and colicins (Harder et al., 1981; Pugsley and Schnaitman, 1978). The clinical strains here studied lack OmpF therefore OmpC would serve as the major routes for the uptake of essential nutrients.

Although the role of outer membrane proteins in antibiotic resistance has long been known, the molecular basis of mutations that occur in the clinic has not been addressed

previously.The simplest method of blocking antibiotic transport is to either delete the pore or render it non-functional. One can speculate that this is because having lost OmpF, the bacteria need to keep OmpC functional. For the future work, detailed structure information would help understand the molecular basis for the antibiotics resistance (which will be discussed in the next chapter). The data of MTT with antibiotics could be further solidified with HN705 untransformed cells and HN705 cells transformed with OmpCO6 as controls. Preliminary trials with HN705 untransformed cells growing in LB medium showed they have much lower inhibition rate to the antibiotics especially the two β-lactams (Figure 2.4.1). However, these HN705 untransformed cells were growing in LB medium without glucose supplement. It was noticed earlier that glucose does influence the protein expression on all the cells in this study (Figure 2.4.2) and in turn, it might influence the metabolic activity of the cells. The cells show a similar protein expression pattern when the growth conditions are identical. Since the cells of HN705-OmpC20 and HN705-OmpC33 were grown with glucose, the data of HN705 untransformed cells grown without glucose might not be valid as a real control. Cells of untransformed HN705 growing with glucose need to be tested on their antibiotic resistance.

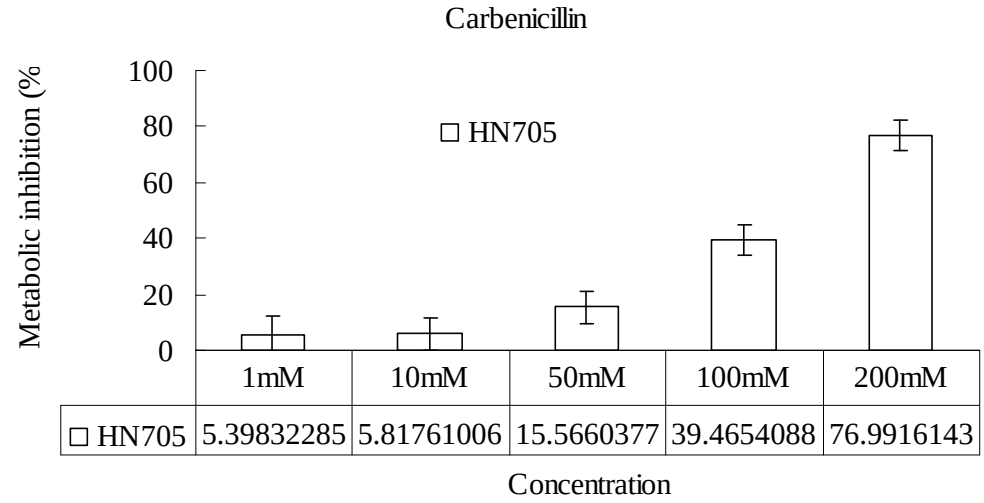

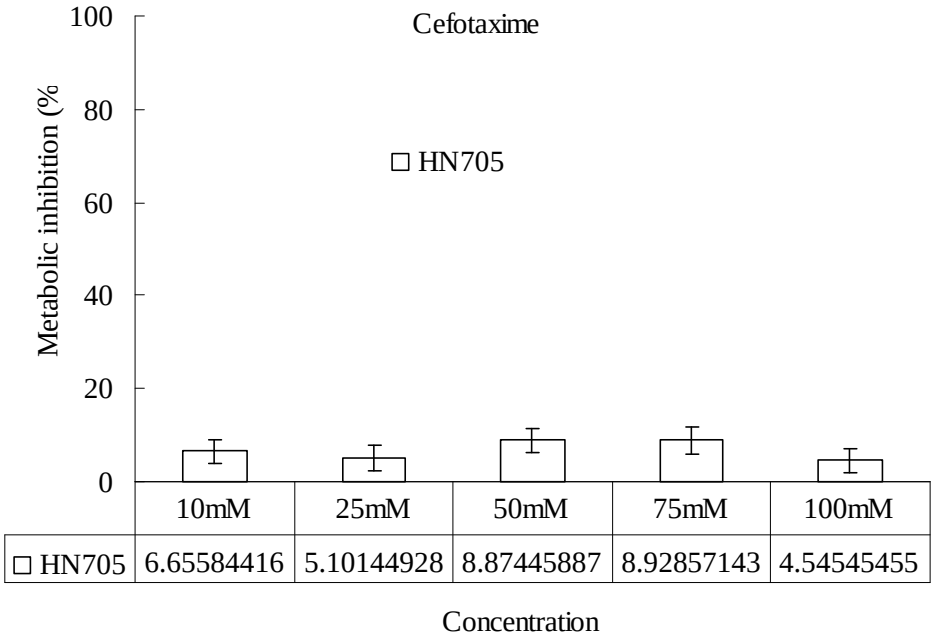

Figure 2.4.1 Effect of antibiotic concentration on the metabolic activity of HN705 untranformed cells. The antibiotics are stated. Sample was triplicated and the error bar is shown.

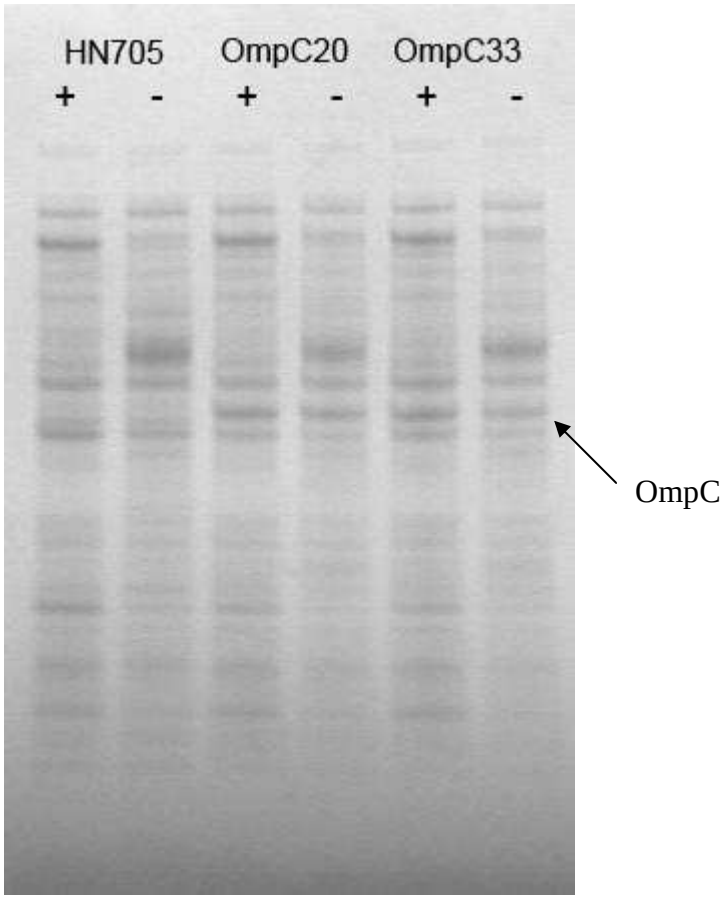

Figure 2.4.2 Influence of glucose on the whole cell protein expression of HN705 untransformed cells and HN705 cells expressing OmpC20 and OmpC33, respectively. The lanes are indicated above: + represents glucose being added in the growth medium, - represents no glucose added in the growth medium. The position of the target protein OmpC was indicated by the arrow.

Chapter 3

Crystal structures of clinical OmpC porin

Summary

This chapter dealt with Gram-negative bacterial outer membrane protein expression, purification, and crystallization. From the structural information, we wished to understand how mutations in the porin of a clinically isolated *E. coli* strain resulted in antibiotic resistance. Porins were among the first membrane proteins whose structures have been solved by X-ray crystallography. Porins occur naturally in abundance in the bacterial outer membrane. This, together with their robust structures made purification and crystallization relatively easier compared to other membrane proteins.

The structures of the first mutant OmpC20 along with its native type OmpCO6 were solved by Dr. Vicki Bamford in our lab. Three further OmpC mutants, denoted as OmpC26, OmpC28 and OmpC33 were solved to 2.28Å, 2.85Å and 3.55Å. The structures of these mutant proteins provide insights into the molecular mechanism of antibiotic resistance.

3.1 Materials and methods

3.1.1 Expression and purification of OmpC

The transformed HN705 cell cultures were grown at 310K for 18 hours in Luria-Broth (LB) containing 30 µg / ml chloramphenicol and 0.5 % (w/v) glucose. The cells were then pelleted by centrifugation at 6,000g (277K) for 15 mins. The cells were lysed by sonication in 50mM sodium phosphate, pH 7.5 and 50mM NaCl. The lysate was centrifuged at 100, 000g (277K) for 1 hour to collect the membranes. The disrupted membrane mixtures were resuspended in 2% (w/v) sodium N-lauroyl sarcosine and incubated at 293K for 2~4 hours with stirring. This step is to solubilise the inner membrane. The supernatant was ultracentrifuged (277K) at 100,000g for 1 hour again to collect the outer membranes (OM). The outer membranes were resuspended in 0.5% (w/v) 3-(N, N-Dimethylmyristyl-ammonio) propanesulfonate (SB 3.14, Sigma) and incubated overnight at 293K with stirring. Insoluble materials were removed by centrifugation at 100,000g (277K) for 1 hour.

The supernatant was applied to a POROS-HQ anion exchange column pre-equilibrated with 50mM sodium phosphate, pH 7.5, 50mM NaCl and 0.025% (w/v) SB3-14. Weakly bound proteins were eluted with 100mM NaCl before elution of OmpC with 1M NaCl. Fractions containing OmpC as determined by SDS-PAGE were pooled and diluted into low salt buffer (salt concentration about 50mM NaCl) in order to bind the protein to the

column again for detergent exchange to a mixture of 0.6% (w/v) 2-hydroxyethyloctylsulfoxide (HESO) and 0.1% (v/v) n-octylpolyoxyethylene (OPOE), or 1% *n*-octyl-β-D-glucopyranoside (βOG). Once the proteins were bound to the column, they were washed at a low flow rate of 1~5 ml/min with 100ml of the above detergents in 20mM Tris-HCl, pH 8.0. A further step of purification, gel filtration, was applied to remove the lipids and residual contaminants. The protein was loaded onto a gel filtration column (Superdex 200, Pharmacia) and eluted in 20 mM Tris-HCl pH 8.0 buffer containing the above detergents. The elution was performed with one column volume of 20mM Tris-HCl, pH 8.0 together with the detergents used in the last anion exchange step. The protein eluted as a trimer at around 120 kDa. Fractions containing OmpC were pooled and concentrated. The protein concentration was determined by UV absorbance using an extinction coefficient at 280nm of 69920 M^{-1} cm^{-1}. The theoretical value of extinction coefficient was obtained from online structure analysis tool (http://www.expasy.ch/tools/protparam.html). Protein purity was checked at all stages by SDS-PAGE (Fig. 2.3.1) and mass spectrometry at the end of purification.

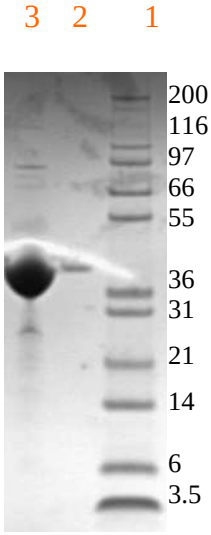

Figure 3.1.1.1 Coomassie blue stained SDS-PAGE gel of purified OmpC26 before crystallization. Lane 1 shows the molecular marker with the corresponding molecular weights (kDa) next to each band. Lane 2 corresponds to the purified OmpC26, Lane 3 is OmpC26 concentrated 100×more than that in Lane 2. It is shown that OmpC migrates as a major band at ~38 KDa (monomer) when the samples are heated in SDS-sample buffer at 373K prior to electrophoresis.

3.1.2 Crystallization of OmpC and optimization

Prior to crystallization experiments, the protein solution was subjected to ultracentrifugation (100,000g, 1hour, 277K) to remove aggregates. Initial crystallization trials were performed using the screens MemSys (Molecular Dimensions), MembFac (Hampton research) and Basic Kit for Membrane Proteins (Sigma). The protein concentration used for crystallization was 10-14 mg/ml. Sitting drop or hanging drop vapor diffusion technique was employed throughout the screening and optimization process, with protein drops of 1~3 µl and a 1:1 ratio of protein: precipitant set up against 100 µl of reservoir solution. The crystallization trials were set up both at cold room temperature (4°C) and room temperature (20°C). Crystals with different shapes appeared after a couple of days with sizes getting larger after up to a month of incubation (Figure 3.1.2.1).

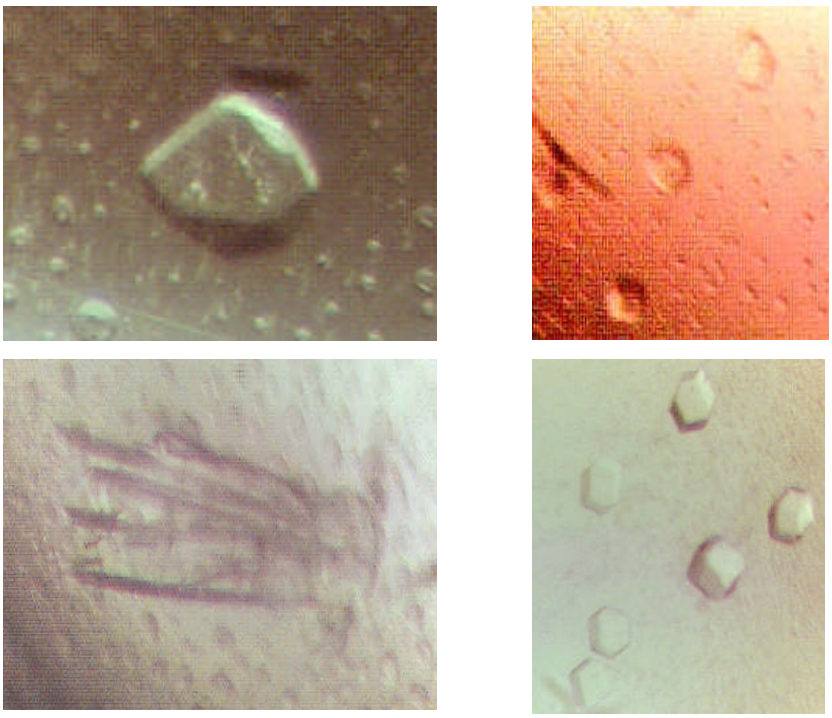

Figure 3.1.2.1 Crystal forms of OmpC grown in different crystallization conditions grown in one week (top two) up to one month (bottom two). From top left clockwise, the crystal was OmpC26, OmpC28, OmpC28 and OmpC26.

Crystals of OmpC26 were grown optimally using the detergent mixture of 0.6% HESO and 0.1% OPOE at room temperature (20°C). The best crystal of OmpC26 was grown from 0.1M ammonium sulfate, 0.1M 4-(2-hydroxyethyl)-1-piperazineethanesulfonic acid (HEPES)-sodium pH 7.5, 0.5M di-sodium hydrogen phosphate dihydrate, and 0.5M di-potassium hydrogen phosphate plus 0.1M carbenicillin di-sodium.

Crystals of OmpC28 and OmpC33 were obtained from conditions with 0.8~1% βOG both at 4°C and 20°C. Initial hits for OmpC28 and OmpC33 crystal were in a precipitant containing 0.8% βOG, 0.1M HEPES pH 7.5, 0.1M MgCl2, 18% PEG400 at 20°C and 4°C, respectively. These crystals diffracted to 4Å-5Å at our in house X-ray facility. To get higher resolution, we started optimization of the conditions as well as other parameters like temperature, concentration of the detergent and protein solutions, and additives. A further 48 optimized screening conditions were made as listed in Table 3.1.2.1.

Table 3.1.2.1 Optimization screen conditions for OmpC28

0.1M HEPES, pH 7.5						
PEG400 (v/v, %)	$(NH_4)_2SO_4$ (M)					
	0.05	0.075	0.1	0.15	0.175	0.2
15	1	1a	1b	1c	1d	1e
16.5	2	2a	2b	2c	2d	2e
18	3	3a	3b	3c	3d	3e
19.5	4	4a	4b	4c	4d	4e
21	5	5a	5b	5c	5d	5e
22.5	6	6a	6b	6c	6d	6e
24	7	7a	7b	7c	7d	7e
26	8	8a	8b	8c	8d	8e

The best OmpC28 crystal was grown from optimized condition 5c with 0.1M HEPES, pH 7.5, 0.15M $MgCl_2$, 21% PEG400 plus 50mM carbenicillin disodium at room temperature. The protein was purified in 1% βOG. Although many OmpC crystals grew under the optimized conditions, they didn't diffract to high resolution at our in-house X-ray facility. The best OmpC33 crystal was from 0.1M HEPES, pH 7.5, 0.075M ammonium sulfate, 22.5% PEG400 at room temperature, with detergent 1% βOG. All the crystals were cryoprotected for data collection at 100 K by increasing the PEG400 concentration to 31%. Because the crystals were extremely fragile, we used a step-wise soaking strategy for cryoprotection. We replaced the well solution with higher PEG400 concentration with several steps gradually up to the final cryoprotectant concentration. In some cases, the well solution was replaced by PEG400 and left overnight or even days before directly freezing the crystals.

3.1.3 Data collection and Structure determination

High resolution datasets for each protein crystal were collected on various beamlines at the European Synchrotron Radiation Facility (ESRF, Grenoble, France). Data collection parameters were shown in Table 3.1.3.1. Data were indexed and integrated using MOSFLM (Leslie, 2006). For the OmpC26 diffraction data, because several crystals stuck together resulting in multiple lattices (Figure 3.1.3.1), the strongest lattice at the high resolution range 3Å-2.28Å was selected for indexing and the whole diffracting range (30 Å-2.28 Å) was used for cell refinement. Other datasets were indexed as normal.

Table 3.1.3.1 Data collection for all the OmpC structures. Structures of OmpCO6 and OmpC20 solved by Dr. Vicki Bamford were also included for completeness. However, some information was not available to me as stated in this table.

Data collection					
Dataset	OmpCO6	OmpC20	OmpC26	OmpC28	OmpC33
ESRF beamline	ID14.1	ID14.3	BM14	ID14.1	ID14.3
Wavelength (Å)	0.934	0.931	0.976	0.934	0.931
Crystal to ditector distance (mm)	not available	not available	207.43	300.50	290.87
Oscillation range (°)	Not available	Not available	0.5	0.5	0.25
Temperature of data collection	100K	100K	100K	100K	100K
Exposure time per image	Not available	Not available	30s	5s	30s
Single crystal or Multiple crystals	Single	Single	Single	Single	Single*
Space group	P321	C2	P1	$P6_3$	$P2_12_12$
Unit cell dimensions a, b, c (Å) α, β, γ (°)	120.42, 120.42, 158.08 90, 90, 120	128.02, 74.20, 133.50 90, 124.75, 90	74.18, 93.68, 115.91 98.74, 108.79, 109.71	103.49, 103.49, 186.49 90, 90, 120	142.96, 164.64, 159.83 90, 90, 90
Resolution (Å)	2.5	2.7	30-2.3 (2.42-2.30)**	51.78-2.85 (3.0-2.85)**	30-3.55 (3.74-3.55)**
R_{merge} (%)	10.5 (51.6)	10.2(38.1)	8.4(45.2)	11.8(74.2)	9.8(32.7)
Completeness (%)	99.5(99.5)	99.9(99.6)	97.4(96.1)	96.5(97.4)	81.1(68.2)
$I/\sigma I$	14.3(3.4)	13.1(3.0)	9.9(1.8)	15.5(2.8)	12.8(2.7)
Redundancy	4.7(4.7)	3.7(3.6)	2.2(2.1)	8.1(8.1)	5.2(3.6)

*: It was a single crystal, however, the dataset was collected at 5 parts by shooting at different parts of the crystal.

**: Values shown in blackests were the outer shell resolution limits.

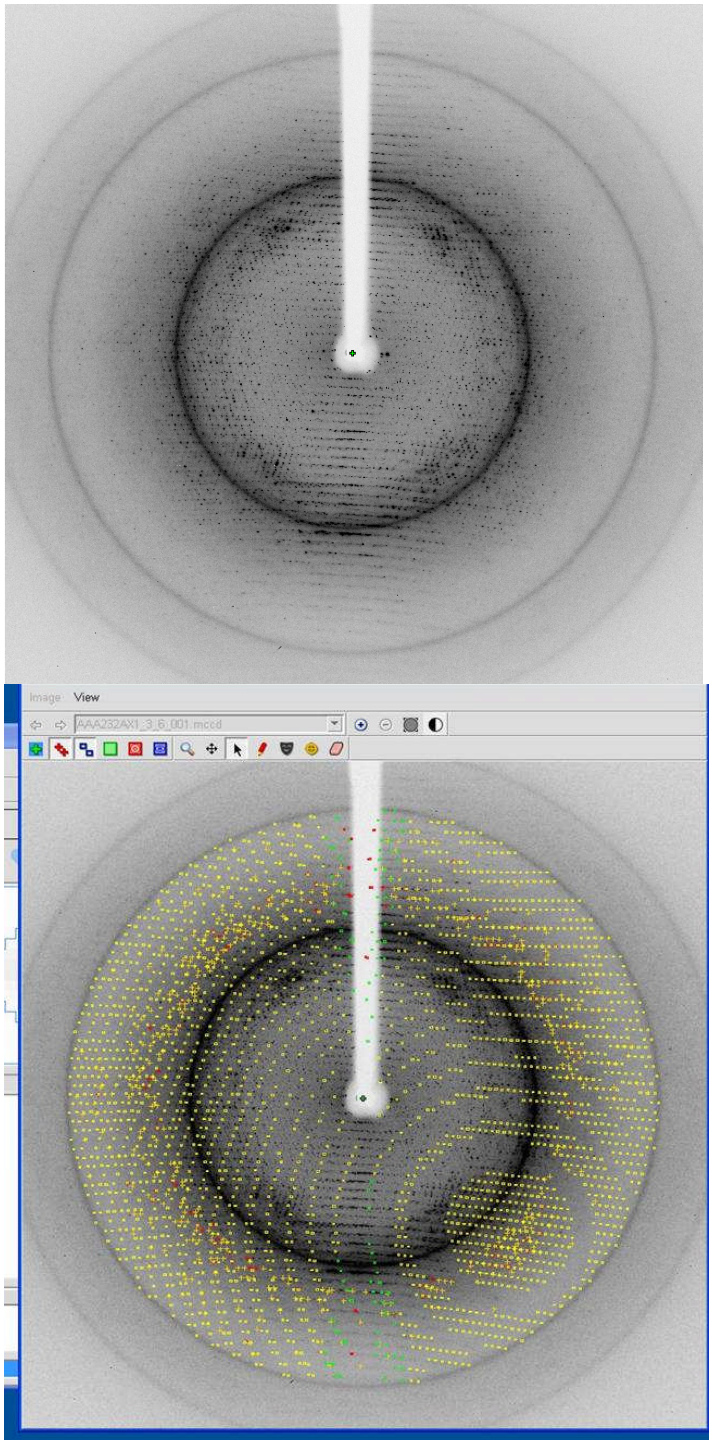

Figure 3.1.3.1 Data processing of OmpC26 by Mosflm. The multiple lattices can be seen after the main lattice (represented by yellow dots, bottom picture) was picked up.

The CCP4 program POINTLESS (Evans, 2006) was used to assign the correct space group. The POINTLESS results for OmpC26, OmpC28 and OmpC33 are showing below.

For OmpC26 data, POINTLESS output indicated the space group is P1:

Nelmt	Lklhd	Z-cc	CC	N	Rmeas	Symmetry & operator (in Lattice Cell)
1	0.943	9.40	0.94	90222	0.109	identity

Laue Group		Lklhd	NetZc	Zc+	Zc-	CC	CC-	Rmeas	R-	Delta	ReindexOperator
P -1	***	1.000	9.40	9.40	0.00	0.94	0.00	0.11	0.00	0.0	[-h,k,-h-l]

For OmpC28 data, POINTLESS strongly suggested the space group should be $P6_3$:

Nelmt	Lklhd	Z-cc	CC	N	Rmeas	Symmetry & operator (in Lattice Cell)
1	0.951	9.69	0.97	375648	0.095	identity
2	0.949	9.64	0.96	494054	0.109 ***	2-fold l (0 0 1) {-h,-k,+l}
3	0.054	1.42	0.14	475943	0.595	2-fold (1-1 0)
4	0.054	1.45	0.14	470903	0.580	2-fold (2-1 0) {+h,-h-k,-l}
5	0.055	1.47	0.15	493656	0.573	2-fold h (1 0 0) {+h+k,-k,-l}
6	0.054	1.45	0.14	470704	0.576	2-fold (1 1 0) {+k,+h,-l}
7	0.054	1.41	0.14	476945	0.593	2-fold k (0 1 0) {-h,+h+k,-l}
8	0.055	1.50	0.15	514887	0.598	2-fold (-1 2 0) {-h-k,+k,-l}
9	0.946	9.59	0.96	949231	0.121 ***	3-fold l (0 0 1) {-h-k,+h,+l} {+k,-h-k,+l}
10	0.946	9.58	0.96	957315	0.125 ***	6-fold l (0 0 1) {-k,+h+k,+l} {+h,+k,-h,+l}

	Laue Group		Lklhd	NetZc	Zc+	Zc-	CC	CC-	Rmeas	R-	Delta	ReindexOperator
> 1	P 6/m	***	0.993	8.17	9.62	1.45	0.96	0.15	0.11	0.59	0.0	[h,k,l]
2	P 1 2/m 1		0.003	6.14	9.66	3.52	0.97	0.35	0.10	0.45	0.0	[k,l,h]
- 3	P -3		0.003	6.12	9.64	3.52	0.96	0.35	0.11	0.45	0.0	[h,k,l]
4	P -1		0.000	5.49	9.69	4.20	0.97	0.42	0.09	0.41	0.0	[-h,-k,l]
5	C m m m		0.000	1.37	5.58	4.21	0.56	0.42	0.31	0.41	0.0	[-k,2h+k,l]

	Zone	Number	PeakHeight	SD	Probability	ReflectionCondition
1	screw axis 6(3) [c]	87	0.994	0.117	*** 0.917	00l: l=2n
1	screw axis 6(2) [c]	87	0.048	0.117	0.003	00l: l=3n
1	screw axis 6(1) [c]	87	0.039	0.117	0.003	00l: l=6n

For OmpC33 data, POINTLESS suggested the possible space groups can be $P222_1$ or $P2_12_12$, or $P2_12_12_1$. These space groups have been further tested when solving the structure by molecular replacement.

Nelmt	Lklhd	Z-cc	CC	N	Rmeas		Symmetry & operator (in Lattice Cell)
1	0.941	9.32	0.93	266896	2.046		identity
2	0.902	8.97	0.90	192635	2.482	***	2-fold l (0 0 1) {-h,-k,+l}
3	0.900	8.96	0.90	284328	2.344	***	2-fold h (1 0 0) {+h,-k,-l}
4	0.052	0.12	0.01	262715	3.494		2-fold (1 1 0) {+k,+h,-l}
5	0.949	9.52	0.95	190863	2.324	***	2-fold k (0 1 0) {-h,+k,-l}
6	0.049	0.34	0.03	160798	3.313		2-fold (1-1 0) {-k,-h,-l}
7	0.051	0.18	0.02	386363	3.435		4-fold l (0 0 1) {-k,+h,+l} {+k,-h,+l}

Laue Group		Lklhd	NetZc	Zc+	Zc-	CC	CC-	Rmeas	R-	Delta	ReindexOperator
> 1	P m m m ***	0.976	8.97	9.17	0.21	0.92	0.02	2.25	3.43	0.0	[-h,-l,-k]
2	P 1 2/m 1	0.012	5.64	9.39	3.74	0.94	0.37	2.13	2.96	0.0	[h,k,l]
3	P 1 2/m 1	0.006	5.49	9.17	3.68	0.92	0.37	2.18	2.94	0.0	[l,h,k]
4	P 1 2/m 1	0.006	5.79	9.15	3.36	0.92	0.34	2.17	3.03	0.0	[-h,-l,-k]
5	P -1	0.001	4.84	9.32	4.48	0.93	0.45	2.05	2.87	0.0	[-h,-l,-k]
6	P 4/m	0.000	1.34	6.09	4.75	0.61	0.47	2.52	2.80	1.7	[-l,-k,-h]
7	P 4/m m m	0.000	5.38	5.38	0.00	0.54	0.00	2.66	0.00	1.7	[-l,-k,-h]
8	C 1 2/m 1	0.000	-0.34	5.15	5.49	0.52	0.55	2.53	2.74	1.7	[k-l,-k-l,-h]
9	C 1 2/m 1	0.000	0.85	5.97	5.13	0.60	0.51	2.37	2.81	1.7	[-k-l,-k+l,-h]
10	C m m m	0.000	-0.75	5.05	5.80	0.51	0.58	2.64	2.69	1.7	[-k-l,-k+l,-h]

	Zone	Number	PeakHeight	SD	Probability		ReflectionCondition
1	screw axis 2(1) [a]	No observations					
2	screw axis 2(1) [b]	106	1.039	0.205	0.940	***	0k0: k=2n
3	screw axis 2(1) [c]	No observations					

Choosing between possible best groups:

Space group	Point group	Reindex
P 2 2 21	P 2 2 2	[-k,-h,-l]
P 21 21 2	P 2 2 2	[-h,-l,-k]
P 21 21 2	P 2 2 2	[-l,-k,-h]
P 21 21 21	P 2 2 2	[-h,-l,-k]

SCALA was used for scaling and merging of the data. The resolution limit was determined by the data statistics and the Wilson plot. The program XTRIAGE was applied to check the data quality and reflection outliers were deleted for OmpC26 dataset. OmpC26, OmpC28 and OmpC33 datasets were also checked for the anisotropy by submitting to the Diffraction Anisotropy Server (http://www.doe-mbi.ucla.edu/~sawaya/anisoscale/). OmpC26 data shows slight anisotropy (data not shown) while OmpC33 data shows severe anisotropy. Figure 3.1.3.2 shows the diffraction pattern of OmpC33 and its anisotropy detected by the software. Ellipsoidal truncation and anisotropic scaling was performed for

data of OmpC26 and OmpC33 datasets (Strong et al., 2006). Approximately 20% of measurements were removed for OmpC26 data and 15% for OmpC33.

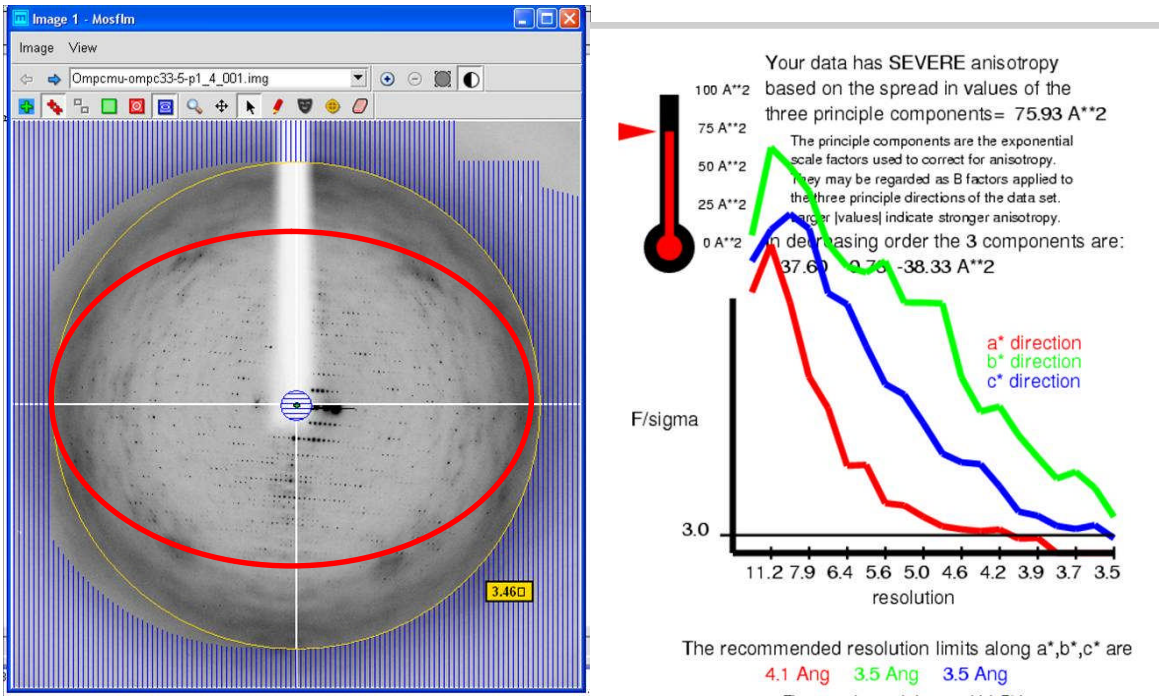

Figure 3.1.3.2 Diffraction pattern of OmpC33 (left) and its anisotropy detected by the Diffraction Anisotropy Server (http://www.doe-mbi.ucla.edu/~sawaya/anisoscale/). The red oval circle indicated the anisotropic diffraction pattern.

The structure of OmpC26 was solved by molecular replacement using the refined 2.7 Å OmpC20 structure as the search model with the program MOLREP (Murshudov et al., 1997) in the CCP4 program suite (CCP4, 1994). Caculation of the Matthews coefficient suggested the presence of two trimers in the asymmetric unit with a coefficient value of 3.00 and water content of 59.0% based on a molecular weight of 38000 Da per monomer.

Using a trimer search model and data in the resolution range 30 - 3 Å, clear solutions for the two trimers in the asymmetric unit were obtained. The crystal packing was examined as shown in Figure 3.1.3.3. The two trimers are associated loop-to-loop via hydrophilic interactions. For further refinement, a 2 times 3-fold NCS restraints for each trimer and TLS refinement for the two trimers were employed. In the last three rounds of refinement, tight NCS restraints except for the residue 131, 284, and 322-326 was applied and 4 TLS groups were assigned (1-50, 51-150, 151-275, 276-343, figure 3.1.3.4) according to the TLSMD server (http://skuld.bmsc.washington.edu/~tlsmd/) (Painter and Merritt, 2006). The 4 segments were generated by the program according to their structure flexibility (Painter and Merritt, 2006).

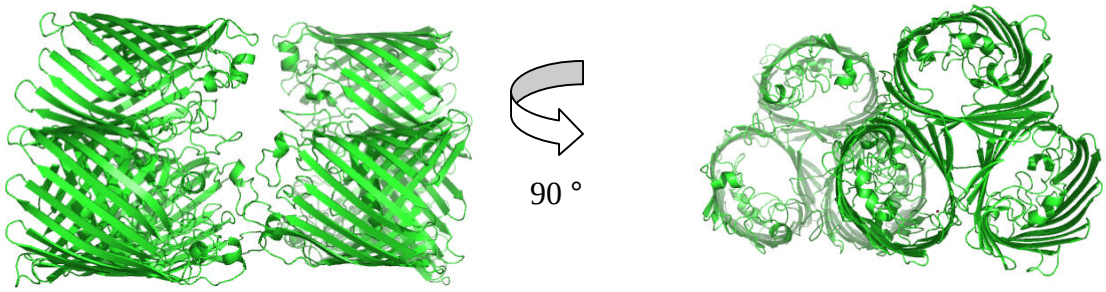

Figure 3.1.3.3 Crystal packing of OmpC26 after molecular replacement.

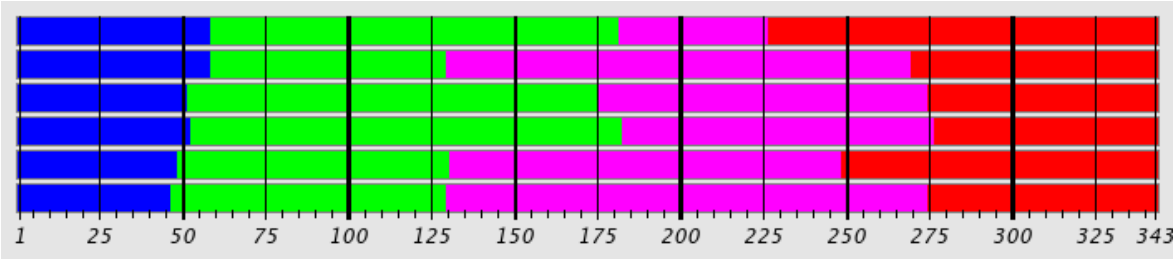

Figure 3.1.3.4 TLS groups assigned by TLSMD server (http://skuld.bmsc.washington.edu/~tlsmd/).

The structure of OmpC28 was solved by MOLREP using the OmpC26 monomer as the search model. Although there are two monomers in the asymmetric unit, symmetry application resulted in a trimeric structure and the symmetry of space group resulted the trimer structure (Figure 3.1.3.5).

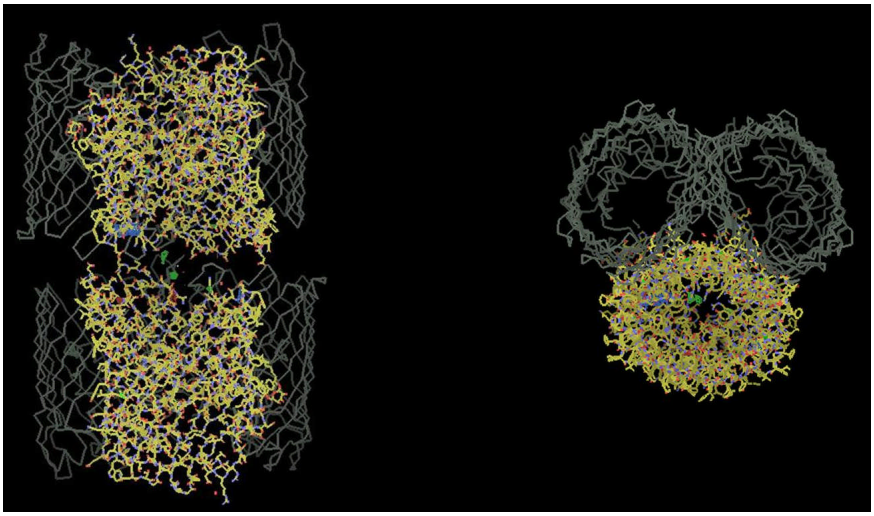

Figure 3.1.3.5 Crystal packing of OmpC28 after molecular replacement.

Refinement proceeded in the same way as for OmpC26. The model was refined with 2-fold NCS restraints and TLS. The map clearly shows the mutation site of S271F (Figure 3.1.3.6)

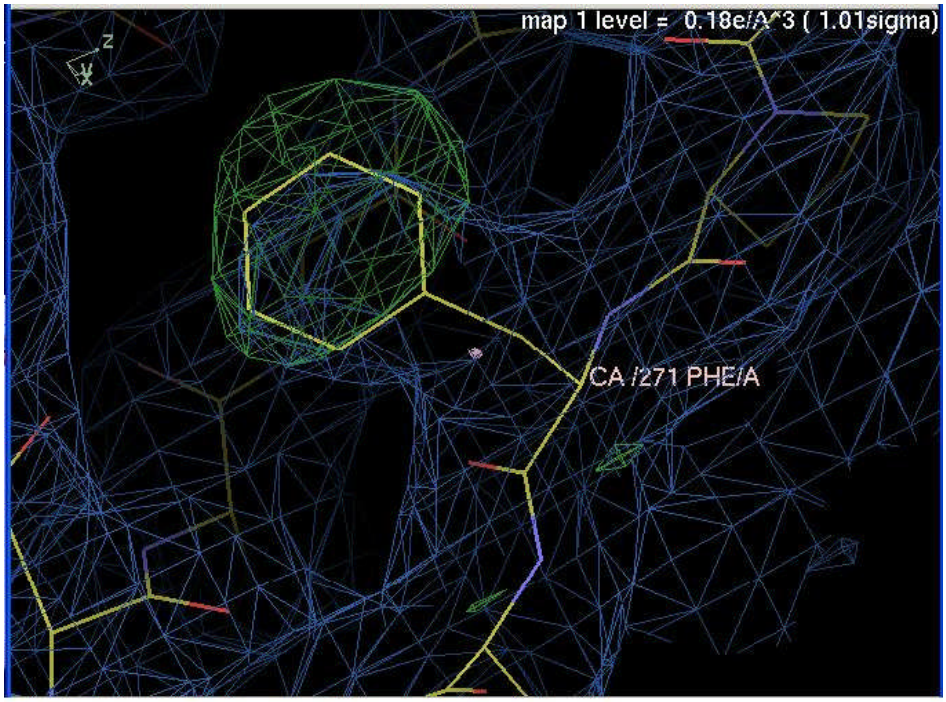

Figure 3.1.3.6 Electron density map of the mutation site of S271F in OmpC28 at 1σ level and difference map at 3σ level.

The structure of OmpC33 was solved by PHASER using the refined 2.3Å OmpC26 structure (trimer) as the search model. To verify the structure, we used the OmpC26 monomer as the search model and it gave the same molecular arrangement. Figure 3.1.3.7 shows the crystal packing of OmpC33. Because of the low resolution, no water molecules can be assigned. By applying NCS and TLS following one round of manual building in Coot, both R_{fac} and R_{free} improved from 48.8% to 39.2% and 41.7%, respectively.

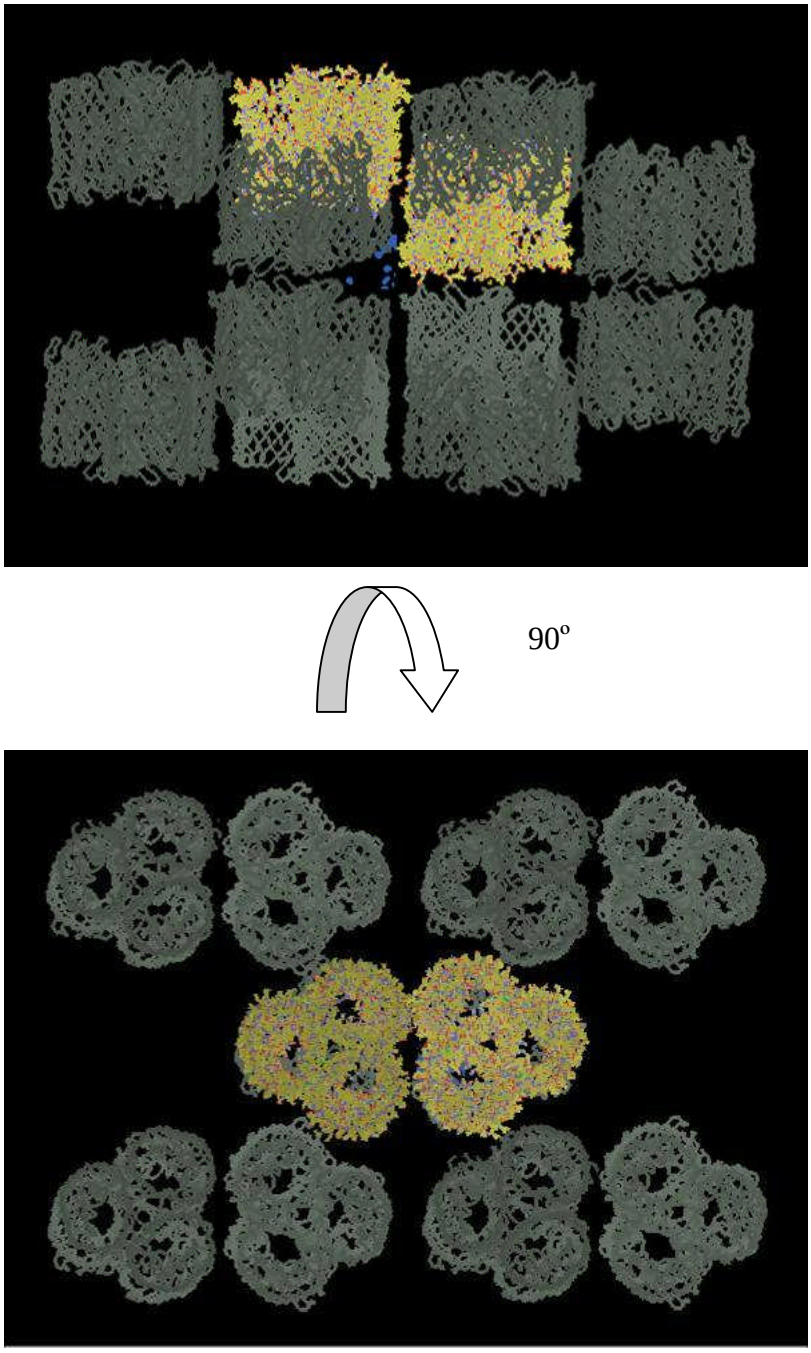

Figure 3.1.3.7 Crystal packing of OmpC33 after molecular replacement.

The stereochemical quality was analysed using MolProbity. Figure 3.1.3.8 shows the Molprobity score for the OmpC26, OmpC28 and OmpC33 structure validation.

OmpC26:

Summary statistics

All-Atom Contacts	Clashscore, all atoms:	9.65	94th percentile* (N=356, 2.03Å - 2.53Å)
	Clashscore is the number of serious steric overlaps (> 0.4 Å) per 1000 atoms.		
Protein Geometry	Rotamer outliers	0.42%	Goal: <1%
	Ramachandran outliers	0.00%	Goal: <0.2%
	Ramachandran favored	95.01%	Goal: >98%
	Cβ deviations >0.25Å	0	Goal: 0
	MolProbity score	1.85	94th percentile* (N=8883, 2.03Å - 2.53Å)
	Residues with bad bonds:	0.00%	Goal: <1%
	Residues with bad angles:	0.00%	Goal: <0.5%

* 100th percentile is the best among structures of comparable resolution; 0th percentile is the worst.

OmpC28:

Summary statistics

All-Atom Contacts	Clashscore, all atoms:	6.86	100th percentile* (N=97, 2.6Å - 3.1Å)
	Clashscore is the number of serious steric overlaps (> 0.4 Å) per 1000 atoms.		
Protein Geometry	Rotamer outliers	1.08%	Goal: <1%
	Ramachandran outliers	0.00%	Goal: <0.2%
	Ramachandran favored	96.48%	Goal: >98%
	Cβ deviations >0.25Å	0	Goal: 0
	MolProbity score	1.63	100th percentile* (N=4562, 2.6Å - 3.1Å)
	Residues with bad bonds:	0.00%	Goal: <1%
	Residues with bad angles:	0.00%	Goal: <0.5%

* 100th percentile is the best among structures of comparable resolution; 0th percentile is the worst.

(figure continues)

OmpC33:

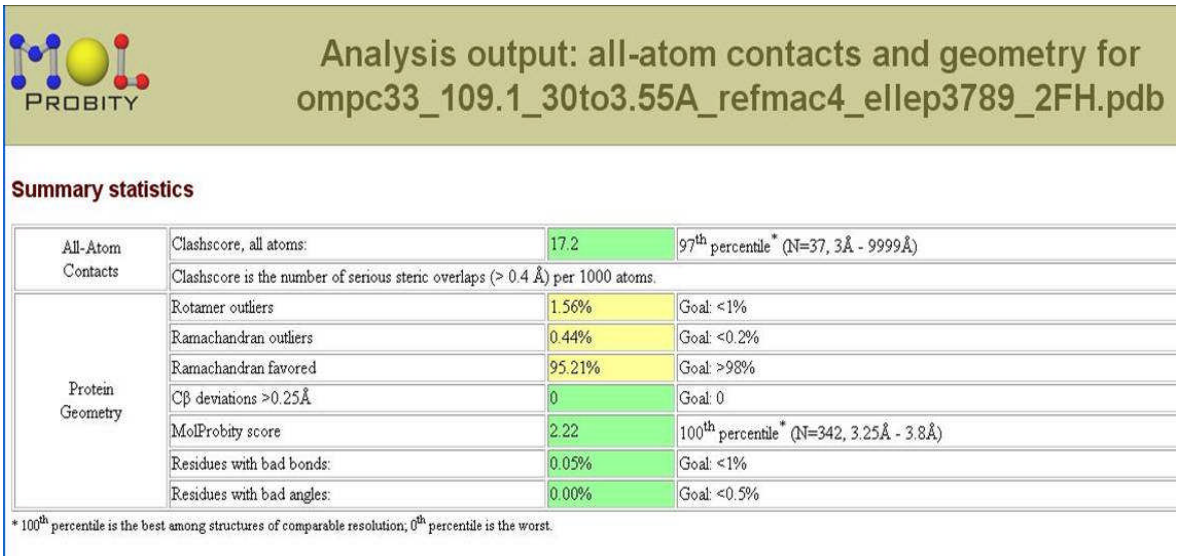

Analysis output: all-atom contacts and geometry for ompc33_109.1_30to3.55A_refmac4_ellep3789_2FH.pdb

Summary statistics

All-Atom Contacts	Clashscore, all atoms:	17.2	97th percentile* (N=37, 3Å - 9999Å)
	Clashscore is the number of serious steric overlaps (> 0.4 Å) per 1000 atoms.		
Protein Geometry	Rotamer outliers	1.56%	Goal: <1%
	Ramachandran outliers	0.44%	Goal: <0.2%
	Ramachandran favored	95.21%	Goal: >98%
	Cβ deviations >0.25Å	0	Goal: 0
	MolProbity score	2.22	100th percentile* (N=342, 3.25Å - 3.8Å)
	Residues with bad bonds:	0.05%	Goal: <1%
	Residues with bad angles:	0.00%	Goal: <0.5%

* 100th percentile is the best among structures of comparable resolution; 0th percentile is the worst.

Figure 3.1.3.8 Molprobity score for OmpC26, OmpC28 and OmpC33.

3.2 Results and discussion

3.2.1 Overall structure of OmpC

Data statistics of all the OmpC structures were shown in Table 3.2.1.1. All mutant OmpC crystal structures determined in this study share the same 16-stranded antiparallel β-barrel with a central pore first reported for OmpC from *E. coli* K12 (Basle et al., 2006). The β-strands are connected by 8 short turns (2 - 8 residues in length) on the periplasmic side and 8 long loops (L1 to L8 of 9 - 30 residues in length) on the extracellular face. As previously observed for the parent OmpC L3 is not exposed on the cell surface, but folds back into the lumen of the barrel forming the constriction zone at middle of the channel. The trimer interface is formed by the packing of hydrophobic residues on the outer edges of strands β1 to β5 and further stabilised by L2 which reaches into the neighboring monomer. In the trimer, the outside surface resembles a fully enclosed bowl with the walls of the bowl formed by the loops 1, 4, 5, 6, 7 and 8 from each monomer. All of the amino acid side chains in contact with the lipid bilayer on the outside of the OmpC trimer are hydrophobic. This hydrophobic band is bordered by two rings of aromatic residues, 20 – 25 Å apart which lie at the interface between the lipid bilayer and the lipid head groups. The outer facing ring consists predominantly of tyrosine residues with the hydroxyl group pointing away from the bilayer towards the solvent. The inner facing ring consists of both tyrosine and phenylalanine residues with the tyrosine hydroxyl groups again pointing towards the solvent.

Tabel 3.2.1.1 Refinement of OmpC structures. Structures of OmpCO6 and OmpC20 solved by Dr. Vicki Bamford were also included for completeness.

dataset	OmpCO6	OmpC20	OmpC26	OmpC28	OmpC33
Refinement					
Resolution range (Å)	50-2.5	50-2.7	30-2.3	50-2.85	30-3.55
No. of unique reflections	43736	27027	118130	25455	37636
Refined structure	2 monomers (2 x 354 residues), 367 H_2O, 2 ADA	1 trimer (3 x 343 residues), 340 H_2O, 4 HESO	Two trimers (2 x 3 x 343residues), 389 H_2O, 1HESO, 2OPOE, 34 acetyl chain as part of detergents, 6 SO_4^{2-}, 1partial HEPES	Two monomers, 2βOG, 32 H_2O	Two trimers
R_{work}/R_{free} (%)	18.6/22.0	23.1/28.5	24.0/27.5	22.1/24.6	39.2/41.7
R.M.S deviations					
Bond length (Å)	0.016	0.005	0.008	0.005	0.011
Bond angles (°)	1.626	0.829	1.051	0.858	1.044

The structure of OmpC from K12 and the OmpC clinical mutants are superimposable with a root mean square deviation (r.m.s.d) of OmpC from K12 and OmpC26 of 0.34Å over 320 Cα atoms excluding the residues of L4. On the amino acid level there are many differences that a direct comparison was unhelpful to identify changes which might be responsible for increased antibiotic resistance. We therefore decided to use the OmpCO6 structure as a closer native, as sequence alignment suggests OmpC20-33 are derived from it. The crystal structure of OmpCO6 was obtained at 2.5Å resolution. The OmpCO6 structure can be superposed with OmpC26 with an r.m.s.d of 0.3Å over 320 Cα atoms excluding the residues of L4. In OmpCO6 the L4 overhangs the lumen of the bowl and protrudes to the entrance of the trimer funnel (Figure 3.2.1.1). In the clinical OmpC mutants, the L4 is shorter resulting in a reduced overhang (the interactions with L1 are conserved). As a result of a number of sequence changes, the entrance to the pore of the clinical OmpCs has a more negative electrostatic surface than OmpCO6 (Figure 3.2.1.1). The negative electrostatic surface extends from the overhung loops to the bottom of the entrance funnel.

The amino acids lining the constriction zone are conserved between OmpCO6 and the clinical OmpCs. The strong transverse electrical field at the constriction zone of the channel is generated by a cluster of basic residues, K16, R37, R74 and R124 on the barrel wall facing acidic residues, D105 and E109 on L3 for OmpCO6. This cationic cluster is stabilised by hydrogen bonds between two residues on strand β4, Q59 and E57 and the NE atoms of R37 and R74 respectively. The residues that form this field are conserved in OmpC20, 26, 28, and 33.

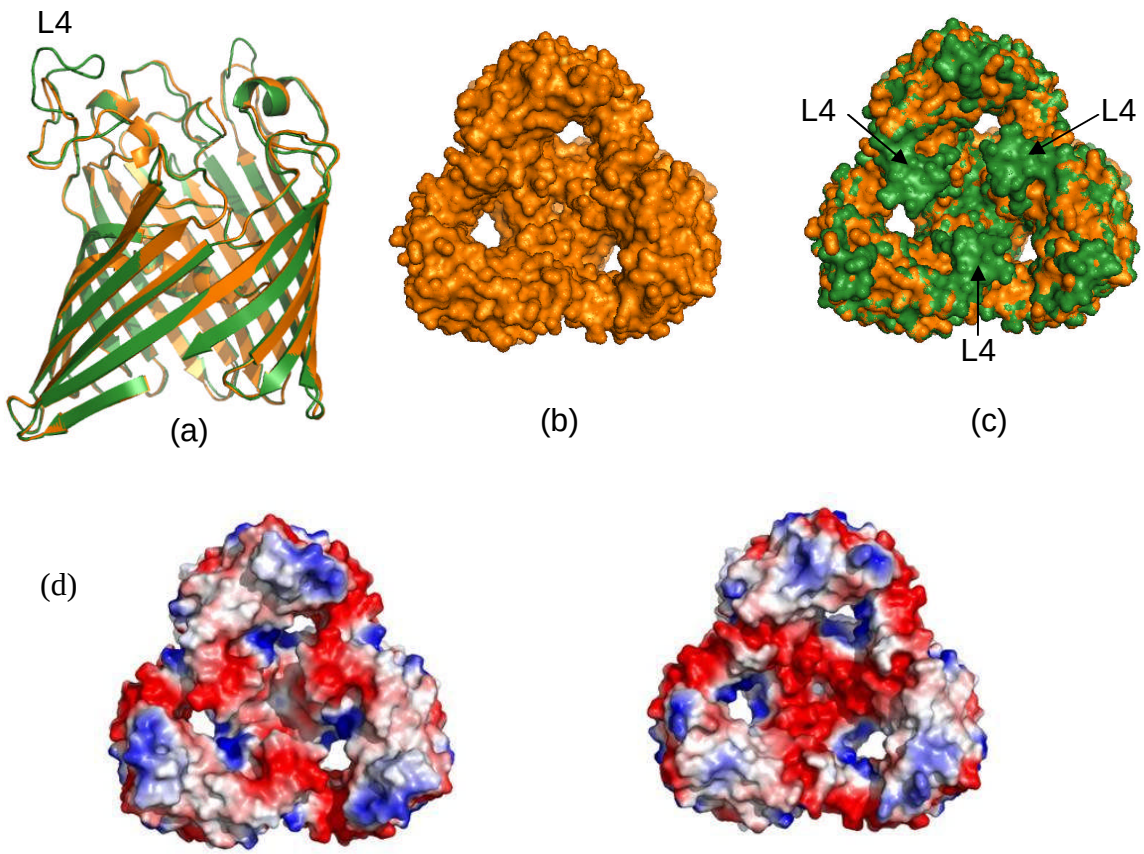

Figure 3.2.1.1 Structure comparison OmpCO6 with OmpC20. (a) A superposition of the OmpCO6 monomer shown in green with the OmpC20 monomer in orange. The main difference is Loop4 as labeled. (b) The molecular surface of OmpC20 view from extracellular side. (c) A superposition of OmpCO6 trimer in green and OmpC20 in orange. The longer L4 in OmpCO6 contributes to narrowing the pore entrance. (d) Extracellular surface of OmpCO6 (left) and OmpC20 (right). Acidic charged surface is coloured red and basic charged surface is coloured blue. These figures were generated by PyMol.

3.2.2 The mutation sites

The high resolution data of OmpC26 enabled us to probe the structure in detail especially the constriction zone. Surprisingly, the basic residues at the constriction zone of OmpC26 monomer all have bound molecules larger than water. We modeled SO_4^{2-} and a partial HEPES molecule into the electron density of one particular monomer, respectively (Figure 3.2.2.1). The basic cluster residues K16, R37, R74 and R124 were involved in binding while the acidic residues in L3 all have water bound. Investigation of the constriction zone also reveals that there is room for only one HEPES-size molecule. It was initially suggested that the constriction zone of OmpF monomer can accommodate one ampicillin molecule regardless of the dissolvation (Nestorovich et al., 2002). Here, we provide the first direct experimental evidence for substrate binding in the constriction zone of general porins.

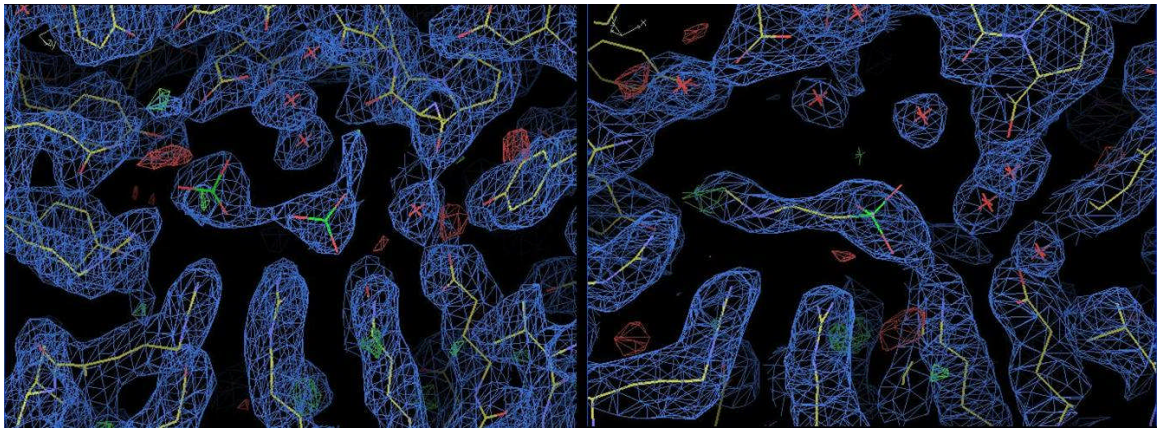

Figure 3.2.2.1 The constriction zone of OmpC26 channel. Left shows two SO_4^{2-} bound to R124, R74, R37 and K16. Right shows a partially modeled HEPES molecule binding to the basic cluster. The red crosses represent water molecules bound to residues in L3.

The clinical OmpC structures are identical except for the 3 mutations (D18E, S271F and R124H) which are all located inside the pore (Figure 3.2.2.2A). In OmpC26 (which has the D18E mutation) the longer side chain of glutamate protrudes into the lumen, thus slightly narrowing the constriction zone. The carboxyl group of E18 is hydrogen bonded to K16, an interaction not seen in OmpC20. Although the hydrogen bond of D18 with Y310 is retained in E18, however a water molecule bound to the carboxyl group of E18 makes a hydrogen bond network with E109 and Y310 (Figure 3.2.2.2B). In OmpC28 the S217F mutation results in replacement of a water molecule that was bound to the hydroxyl of S271 (Figure 3.2.2.2C). In the high resolution data of OmpC26, a water molecule bound to S271 is at the center of a complicated hydrogen bond network between L3 and the barrel wall. Q261, D296 and D312 were all hydrogen bonded to the residues at the tip of L3. The bulky side chain of F271 not only disrupted the hydrogen bond network but also pushed the tip of L3 slightly further (1 Å) into the constriction zone. In OmpC33, R124 is mutated to a histidine residue. Due to the limited resolution of this structure, we cannot identify side chain conformations, water structure or subtle perturbations in main chains of OmpC33. However, the resolution is sufficient for us to be sure that the overall structure has not changed and there is no large re-ordering of the constriction zone. In all other OmpCs, R124 forms a strong salt bridge with E66 from L2 and hydrogen bonds to Y94 and S117 (Figure 3.2.2.2D). In OmpC33 the shorter side chain H124 will disrupt these interactions. Since the experimental structure is unreliable for side chain position, we modeled H124 as a common rotamer. Overall the mutations do not change the channel shape or size appreciably.

Investigation into the size and shape of the constriction zone revealed that although the mutations do not change the channel shape, it is slightly narrower (Figure 3.2.2.3). Thus it appears that the mutant proteins create or disrupt existing H bond networks within the channel which might lead to the fundamental antibiotic resistance.

(A)

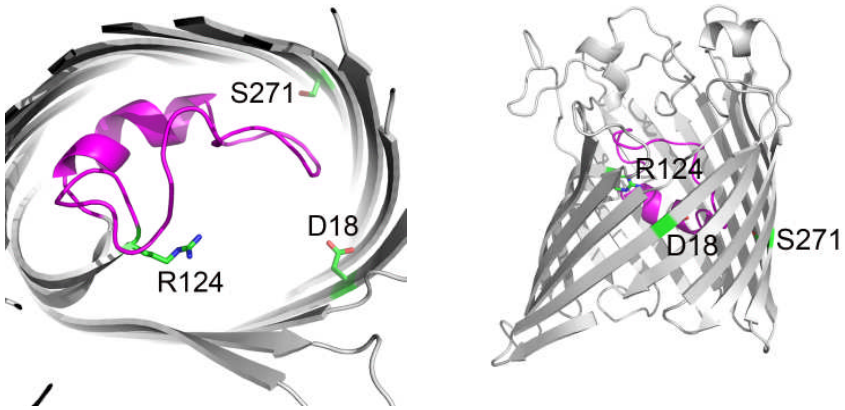

(B)

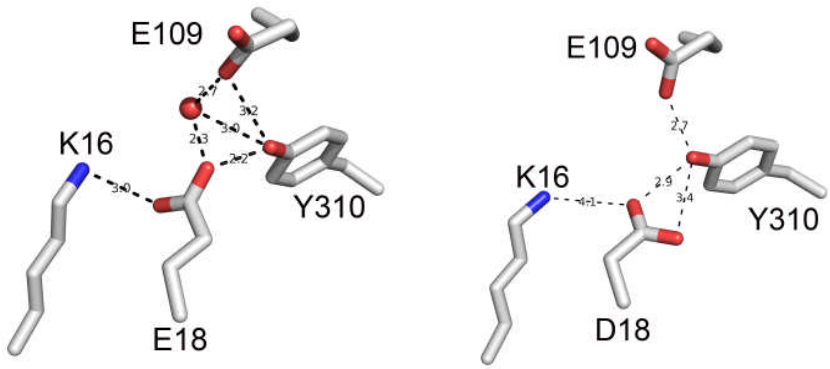

(figure continues)

(C)

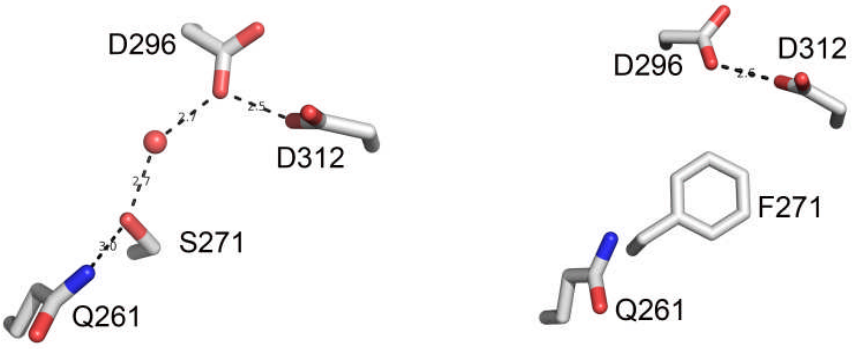

(D)

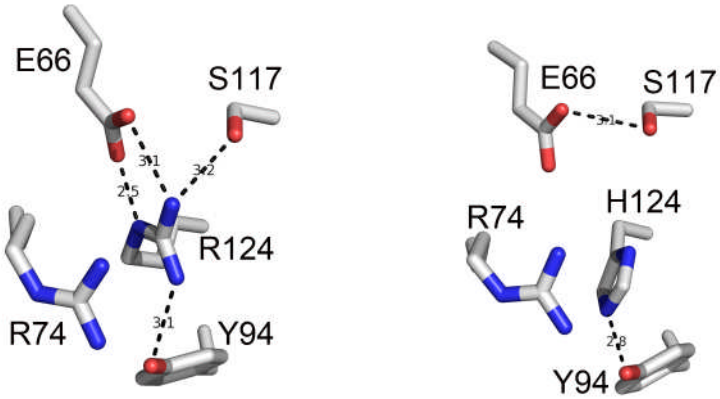

Figure 3.2.2.2. The 3 mutation sites (D18E, S271F and R124H) in the clinical OmpCs. (A) the location of the mutation sites, view from the extracellular side (left) and from side of membrane (right). L3 is colored purple. (B) mutation D18E. (C) mutation S271F. (D) mutation R124H. The residue labeling here is according to the amino acids sequence of OmpC20, not OmpCO6 as did in the sequence alignment in Figure 2.1.4.2.

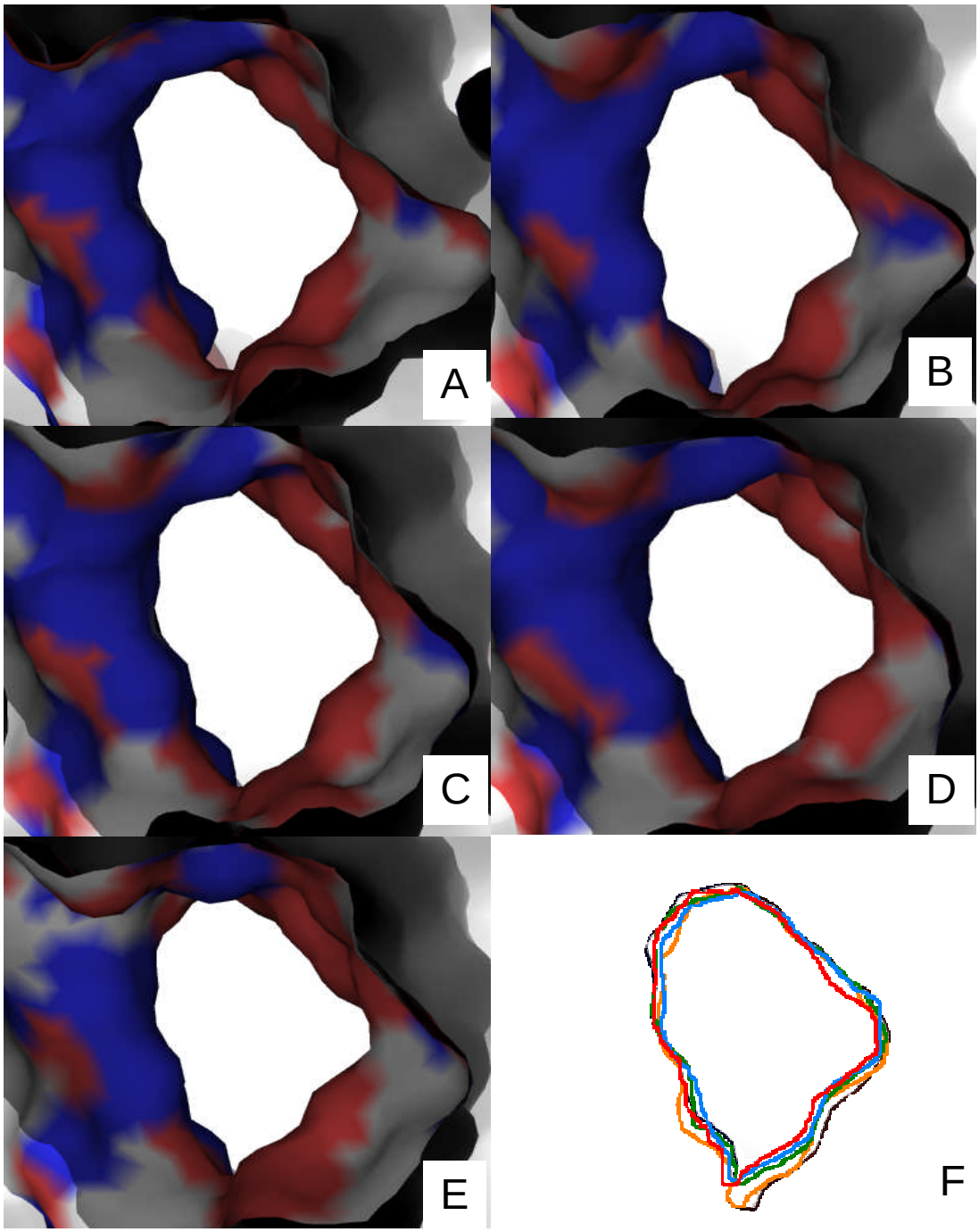

Figure 3.2.2.3 Constriction zone of variant OmpCs (A-E) and schematic representation of the constriction zone (F). A is OmpCO6 shown as black in F, B is OmpC20 shown as yellow in F, C is OmpC26 shown as green in F, D is OmpC28 shown as blue in F and finally F is OmpC33 shown as red in F.

3.3 Discussion

Porins were among the first outer membrane protein structures being solved, due to their redundant presence and their robust barrel nature. Porins are also believed to be important in clinical antibiotic resistance (Pages et al., 2008) as numerous mutations are found. However, no X-ray crystal structures have been reported on antibiotic resistant porins. Here, for the first time we solved a series of OmpC porin structures.

Comparing the structure of the clinical OmpCs and the wild type OmpCO6 revealed the size and shape of the channel is largely unchanged. The mutation of OmpC20 to OmpCO6 resulted in a more open access bowl and an increased electrostatic surface which might facilitate the solute uptake.

It was proposed (Karshikoff et al., 1994; Liu and Delcour, 1998) that in OmpF the position of L3 was controlled by a hydrogen bond network between the tip of L3 and the barrel wall, salt bridges at the root of L3 and electrostatic interactions between the positive cluster at the barrel wall and the negatively charged residues on L3. In S271F, the mutation disrupts the hydrogen bond network and directly affects L3. The loss of the water molecule in S271F will increased the hydrophobicity of the environment between the L3 and the barrel wall. It has been reported that disrupting the hydrogen bond network between L3 and the barrel wall by site directed mutagenesis in OmpC (from *E. coli* K12) increases the flexibility of L3 and closure events (Liu and Delcour, 1998). D18E makes a salt bridge with K16 whilst R124H breaks a salt bridge with E66. It also reduces the net charge which

sits across from the cluster of negative charges on L3. The structural work then supports a model in which L3 is destabilized.

The passage of large charged molecules through OmpC requires that they are first desolvated. Four basic residues cluster together (K16, R37, R74, R124) opposite the negatively charged residues (D105 and E109) create a powerful transverse electric field found in all porins (Simonet et al., 1996). It is this transverse electric field that governs the desolvation energy and hence transport efficacy for large polar molecules (Saint et al., 1996; Van Gelder et al., 1997). The use of charged residues to stabilize the desolvation process is well known, for example in potassium ion channels (Doyle et al., 1998). The mutations D18E and R124H directly change the transverse electric field altering the position of charge and reducing the charge itself. We suggest that these modifications will decrease the ability of the protein to stabilize desolvation, this will particularly affect large highly charged polar molecules.

In summary, the structures suggest that the clinical isolates *E. coli* have evolved a subtle strategy to perturb the stability and electrostatic field of OmpC. This strategy might allow the bacteria to take up nutrients but to decrease their sensitivity to antibiotics (further discussed in next chapter). Although studies of deliberately introduced antibiotic resistance provide very clear results, clinical situations are always more complex but cannot be ignored. In this case other changes in the *E. coli* strain are clearly involved in the manifestation of clinical resistance. However, this study presents molecular evidence for

and a rationale of how changes in OmpC contribute to clinically observed antibiotic resistance. These findings should help us understand how antibiotic resistance develops.

Chapter 4

Channel properties of the clinical OmpC mutants

Summary

We wished to characterize the functional properties of the clinical OmpC mutants, especially the first mutants OmpC20 (from antibiotic sensitive strain) and the last mutant OmpC33 (from antibiotic resistant strain). Single channel measurements of ion conductivity of the channels were carried out. We also tested the interaction of an antibiotic with OmpC20 and OmpC33. With these data and the structural information described in Chapter 3 we propose a novel strategy that bacteria developed during antibiotherapy: it is the changes in the transverse electric field not pore size that underly the clinically observed resistance to the antibiotics.

4.1 Introduction

The planar lipid bilayer technique is often referred to “black lipid membranes” or “BLM’s”. This technique is widely used in the electrophysiology lab nowadays to probe channel-forming proteins to reveal their channel properties. As illustrate in figure 4.1.1, two symmetrical chambers are separated by a Teflon film. In the middle of the Teflon film there is a small hole with a diameter of ~100 μm. The chambers are normally filled with buffered KCl or NaCl solutions usually at 1M concentrations. Two Ag/AgCl electrodes are immersed into the salt solutions and fixed voltages can be applied through these electrodes. The electrodes are connected to signal amplifier which in turn connects to signal filter and eventually connected to computer program which monitor the signals.

The core of the technique is to form an artificial planar lipid bilayer across the hole in the film connecting two chambers (about 3 x 5 cm size). Lipids, usually 1, 2-diphytanoyl-*sn*-glycero-3-phosphocholine (DPhPC), dissolved in pentane were added to each chamber that is filled with salt solutions. Because of the nature of the air-water interface (hydrophobic/hydrophilic), lipids forms a monolayer at the air-water interface after the pentane evaporated. By slowly lowering and raising the water level at the chamber, the lipids move towards to the Teflon film and a bilayer can be eventually formed at the hole (Montal and Mueller, 1972). Once the bilayer is formed, the optical properties of the membrane will appear to be black, hence the name of the technique. In the

absence of added channel proteins, the conductance is very very low and well under detection level.

(A)

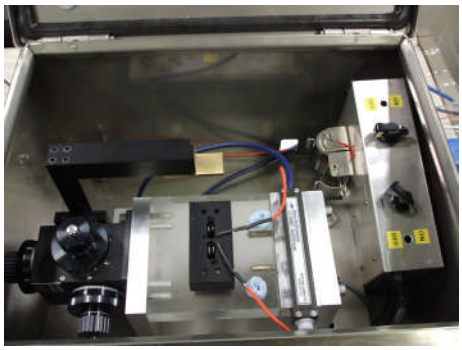

(B)

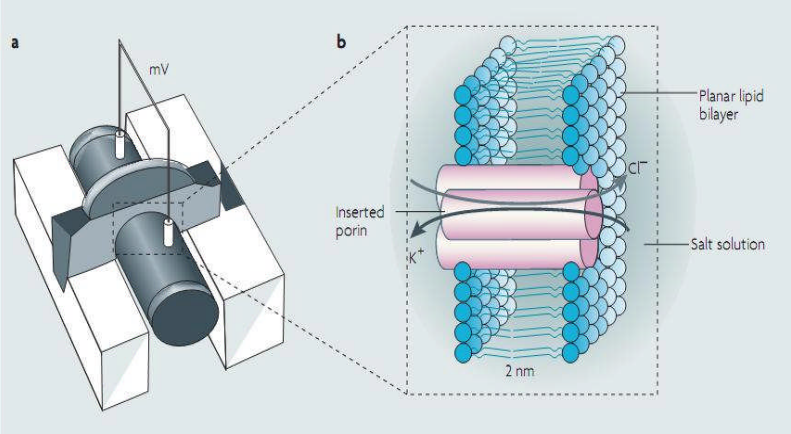

Figure 4.1.1 The core of the planar lipid bilayer technique. (A) Chamber and the connected electrodes, picture taken from Prof. Hagan Baylay's lab at the University of Oxford. (B) Schematic drawing of the chamber. Part a (left) shows the two symmetrical chambers connected together, part b (right) shows an expanded view of an inserted porin within the lipid bilayer. When applied with a certain voltage, cations and ions start follow at opposite directions. (Picture adapted from Pages, 2008)

One side of the chamber is connected to ground hence the potential is zero. Usually the zero potential side is defined as *cis* side and the other as *trans* side. The purified protein is often added to the *cis* side of the chamber, and spontaneous insertion can be seen over the time. Most often, people apply a transmembrane voltage to facilitate the insertion. As channels insert into the membrane, small ions find their way to cross the membrane and therefore an increase in electrical current can be detected across the membrane. A typical electrical current trace is shown in Figure 4.1.2a. The conductance values follow a Gaussian distribution (Fig. 4.1.2b). The fit to this distribution yields an average conductance which is used as the conductance value for a given channel.

(a)

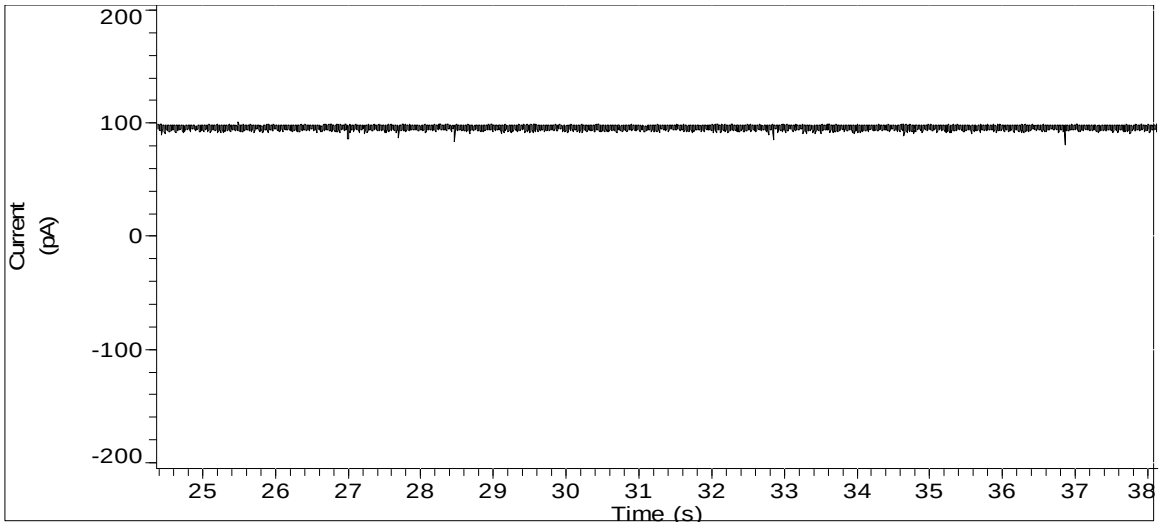

(figure continues)

(b)

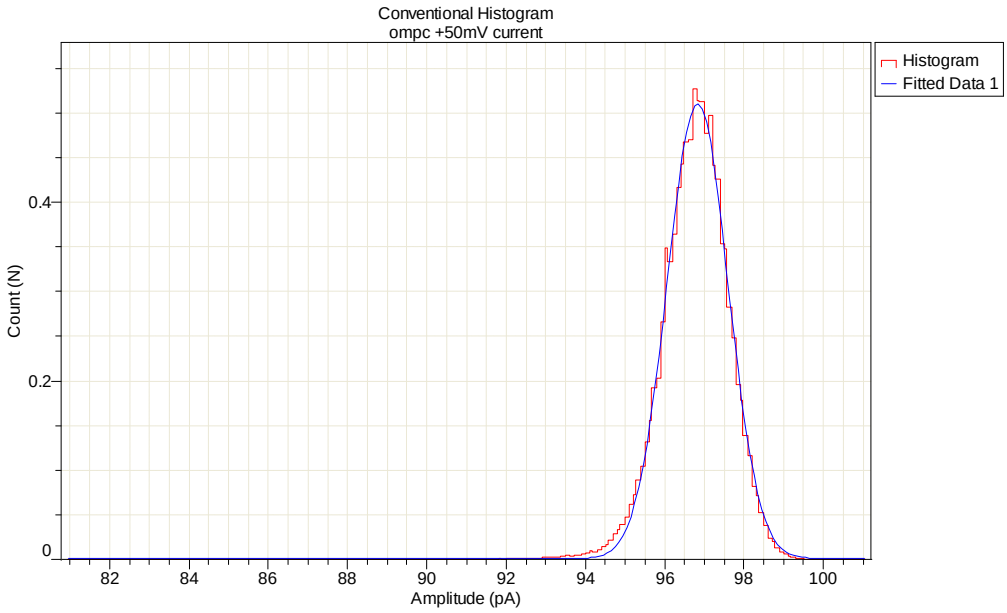

Figure 4.1.2 (a) Current trace of one trimeric OmpC20 channel reconstituted into planar lipid bilayer under +50mV. Membrane bathing solutions contained 1M KCl (pH8). (b) The histogram corresponding to the current trace above shows the value is around 97 pA.

A number of groups have investigated the flux of ions and small molecules through OmpF and OmpC (Danelon et al., 2006; Delcour, 2003; Iyer and Delcour, 1997). Small ion conductance measurements suggest that the pore size of OmpF and OmpC is approximately 1nm (Danelon et al., 2006; Pages et al., 2008), with the trimeric conductivity of OmpF measured in 1M KCl as 4.2nS (Basle et al., 2004; Danelon et al., 2006). Site directed mutagenesis studies have indicated that there is no simple correlation between the measured size of the pore at the constriction zone and the conductance of ions (Bredin et al., 2002; Kleivdal et al., 1999; Phale et al., 2001).

In recent years, the interaction of antibiotics with porin channels is increasingly investigated by the technique of planar lipid bilayers (Danelon et al., 2006; James et al., 2009; Nestorovich et al., 2002). Using the inserted porin channel as a control, addition of antibiotics resulted in ion current fluctuation and analysis of the noise provide information on the channel properties (Nestorovich et al., 2002). Figure 4.1.3 gives a nice example of ampicillin interacting with an OmpF channel that is inserted into the lipid bilayer (figure from Nestorovich et al., 2002).

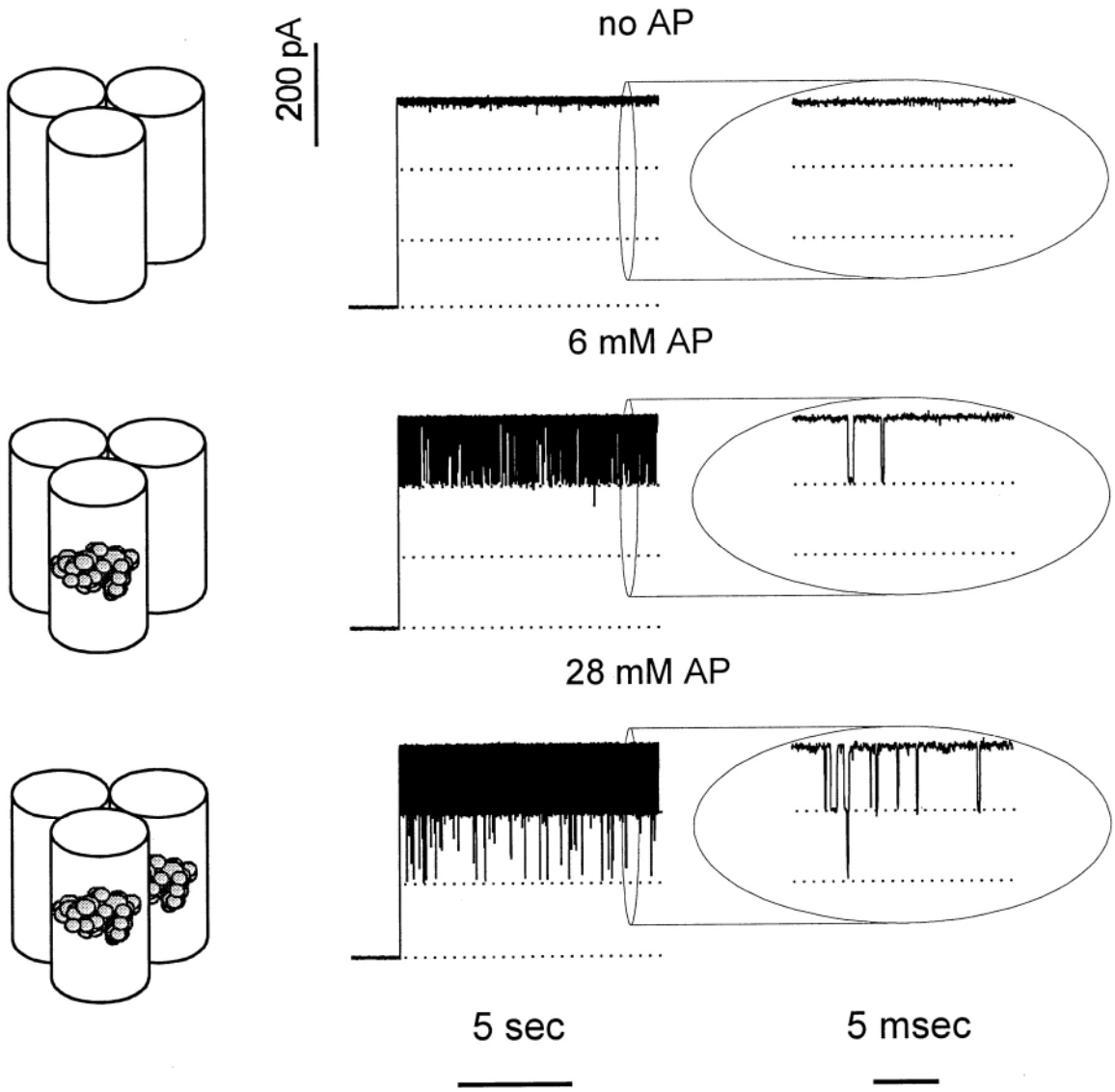

Figure 4.1.3 Ampicillin interact with a single OmpF channel that is inserted into the planar lipid bilayer. (Top) Control experiment without addition of ampicillin, the current is peaceful. (Middle) By addition of 6mM ampicillin, the current become extremely noisy and one of the monomers gets blocked. (Bottom) Increasing the concentration of ampicillin results in an increase of noise and two of the monomers get blocked. (Figure adapted from Nestorovich et al., 2002).

4.2 Materials and methods

4.2.1 Single channel conductance experiments

Single-channel recordings on planar lipid bilayers were carried out as described previously (Movileanu et al., 2000). Briefly, a 25-μm-thick Teflon film (Goodfellow) with a 100 μm diameter hole partitioned two 1.5-ml chambers. The orifice was pretreated with ~5μl 10% (v/v) hexadecane dissolved in high-purity pentane. Each chamber was filled with 1 ml 10 mM Tris-HCl, pH 8.0, 1M KCl. A solution of 10 μl 10% (v/v) 1, 2-diphytanoyl-*sn*-glycero-3-phosphocholine (Avanti Polar Lipids) dissolved in pentane was added to each bath and monolayer formed after the pentane evaporated. By lowering and raising the solution, two lipid monolayers formed a lipid bilayer at the orifice, which was confirmed by its resistance and capacitance. The transmembrane potential was applied through the two Ag/AgCl electrodes immersed in each bath. The *cis* chamber was connected to ground so the potential will always be zero. A positive current is one in which cations flow from the *trans* to the *cis* side and anions flow from the opposite way. Experiments were conducted at room temperature around 20°C.

Single-channel current was amplified with an Axopatch 200B patch-clamp amplifier (Axon Instruments), and filtered at 2 kHz with a built-in low-pass Bessel filter. Signals were digitized with a Digidata 1200 A/D converter at a sampling rate of 20 kHz and recorded by Clampex 9.2 software (Axon). The data were analyzed with the software pClamp 6.03 (Axon) and Origin (Microcal Software Inc.). OmpC purified in 1% βOG at a

final concentration of 0.5-1 μg/ml or the OmpC protein crystals were added to the *cis* compartment. Trimeric channels were inserted into the bilayer by applying electrical potentials of 250-300 mV and were stabilized for recording by lowering the voltages below 250mV.

Studies of the interaction of a range of antibiotics with OmpC were performed at Tris-HCl buffer, pH 8.0, 0.5M KCl instead of 1M KCl as in the single channel conductance measurement, because we observed that the OmpC channels were less noisy at lower salt concentration in the single-channel current recording. Antibiotic stock solution was added to the cis/trans chamber to the desired final concentration after a single channel insertion. Signals were filtered by the built-in low-pass Bessel filter at 10kHz and data saved at a sampling rate of 100kHz.

4.2.2 Thermal stability test

SDS-PAGE was performed to determine the thermal stability of the OmpC mutants. Protein purified in 1% βOG was added to NuPAGE sample buffer (Invitrogen), and incubated for 10min at various temperatures (35 ºC- 100 ºC, in steps of 5 ºC). After the heat treatment, protein samples were immediately transferred to ice before loading onto the NuPAGE 4-12% Bis-Tris gels (Invitrogen). Gels were run at 200 V for 35mins in MES running buffer, pH 7.4, following the manufacturer's protocols. Proteins were stained by Coomassie blue staining. MW values were estimated from the migration rates of Mark-12 markers (Invitrogen).

4.3 Results and discussion

4.3.1 Single channel measurements

The effect of mutation on the ion conductance was probed by single channel current recording. Initial investigation was done based on 20-30 independent experiments for each OmpC mutant. We observed that all the OmpC mutants have a broad range of conductance value ranging from ~0.6nS to ~3.0nS (Figure 4.3.3.1). The conductance at positive and negative potential is slightly different depending on the voltage polarity. This is a consequence of the direction of ion flow in an inherently asymmetric structure.

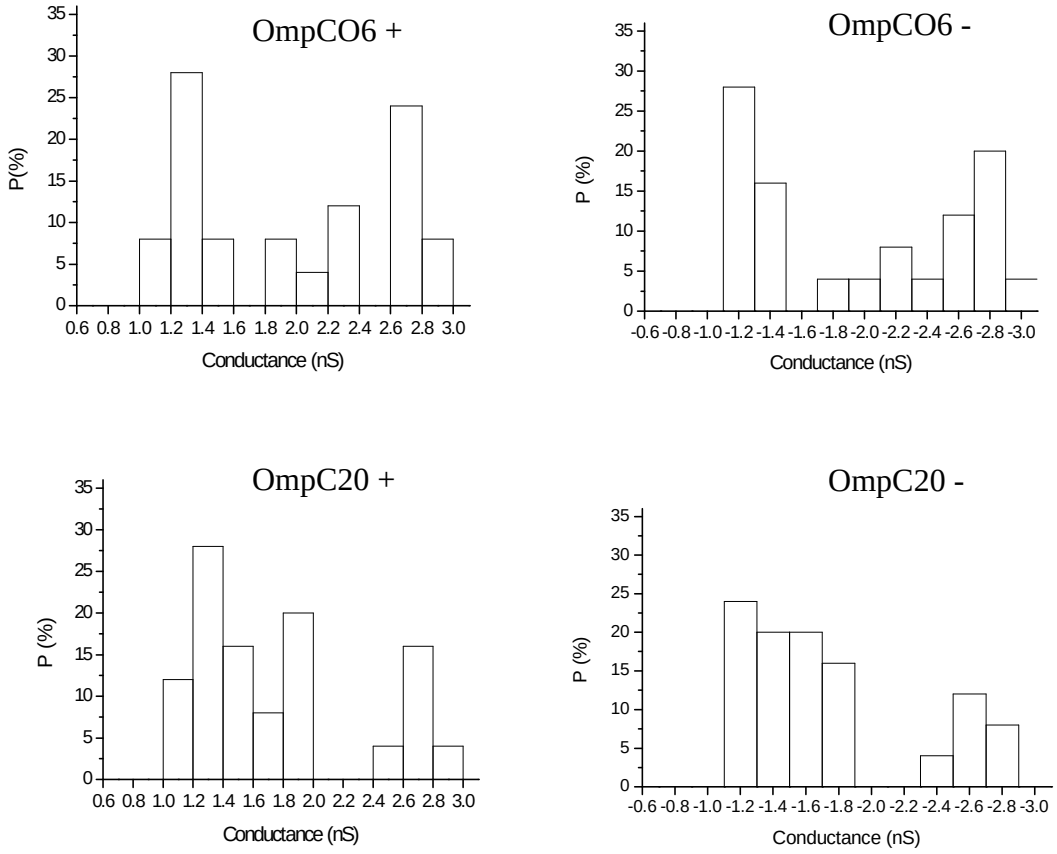

(figure continues)

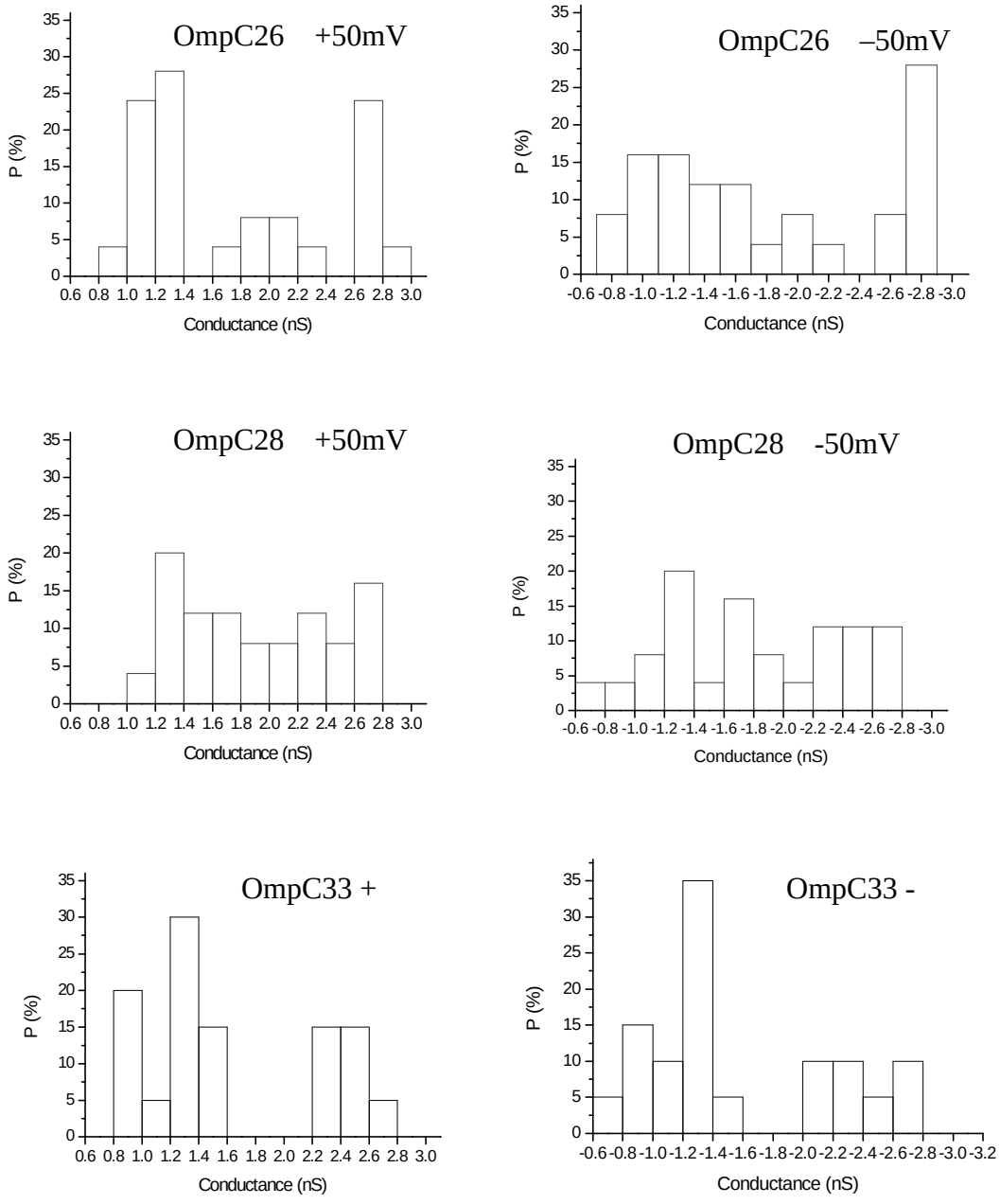

Figure 4.3.1.1 Distributions of the conductance calculated from the current recording under + and -50mV. The bathing solutions contained 1M KCl (pH8) on both side of membrane. The respective mutants with the positive/negative voltage applied are indicated above each

chart. The conductance is in nS, the percentage of events in one of the bins is given as P (%). Only the data with steady traces acquired for at least 30 seconds were analysed and counted.

In order to ensure these varied conductance states are derived from a single trimeric OmpC channel rather than contamination, we repeated the experiments using proteins dissolved from the crystals. The results were the same. In order to get a statistically valid result, we performed more than 70 independent experiments for OmpC20 and OmpC33 respectively. Figure 4.3.1.2 shows the distribution of single trimeric conductance in 1M KCl of OmpC20 and OmpC33 measured under the voltage of ±50mV. On average, OmpC20 has a conductance of 2.1nS (±0.68nS) while OmpC33 has 1.9nS (±0.65nS); the largest conductance for OmpC20 was 3.3nS while for OmpC33 was 3.0nS. These values are bigger than what has been reported for OmpC trimeric conductance (Bishop et al., 1996; Mobasheri and Lea, 2002), under different experimental conditions. However, it is in good agreement with OmpF measured in similar conditions (Nestorovich et al., 2002; Schmitt et al., 2006). The mutations appear to have almost no effect on small ion transport.

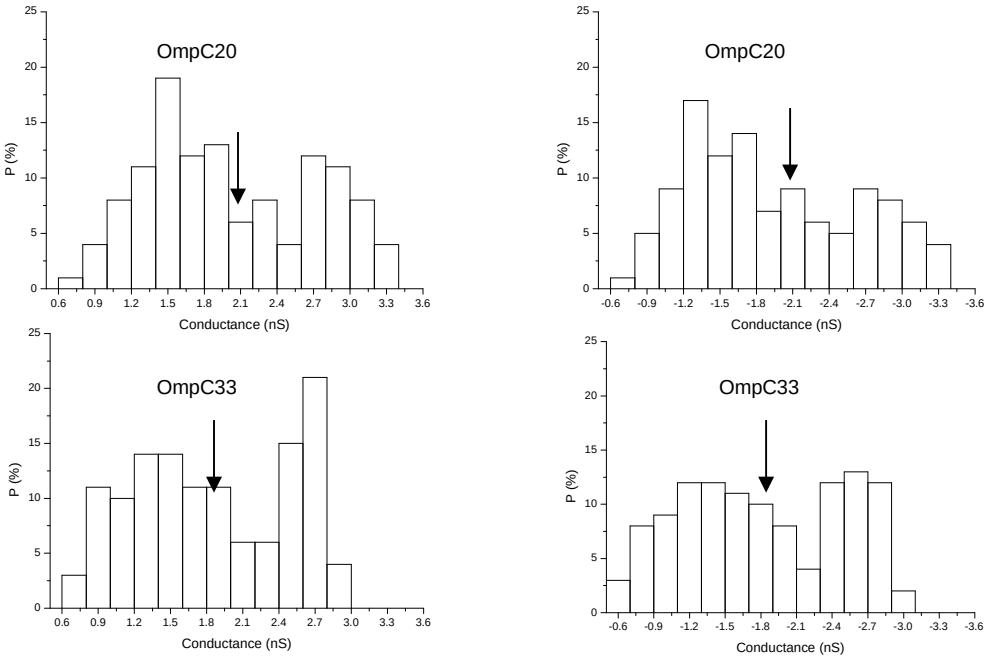

Figure 4.3.1.2 Distribution of ion conductance calculated from the current recording under +-50mV (B). The buffer used is 1M KCl (pH 8) on both side of chamber. Only the data with steady traces acquired for at least 30 seconds were analysed and counted. Each plot was based on 100-130 experiments. The downward arrow represents the average conductance value with OmpC20 of 2.0nS while OmpC33 of 1.9nS.

The variation in conductivity was unexpected and was investigated further to exclude artifacts. The highest conducting state of OmpC (3.3 nS) reproducibly undergoes three step closure at voltages >200mV as shown in figure 4.3.1.3. We interpret this as sequential closure of the monomers within the trimer and that the maximum value as all three monomer channels in the trimer being open. In order to evaluate genuine variation in conductivity, single channel conductance was measured at 50mV, the voltage was then

increased to 250mV for around 30s then the voltage decreased to 50mV (Figure 4.3.1.3). After this process when the voltage is set to 50 mV, the current does not always return to the same value even for the same protein. We suggest this demonstrates that there is genuine variety of conducting states even for a single trimeric OmpC channel.

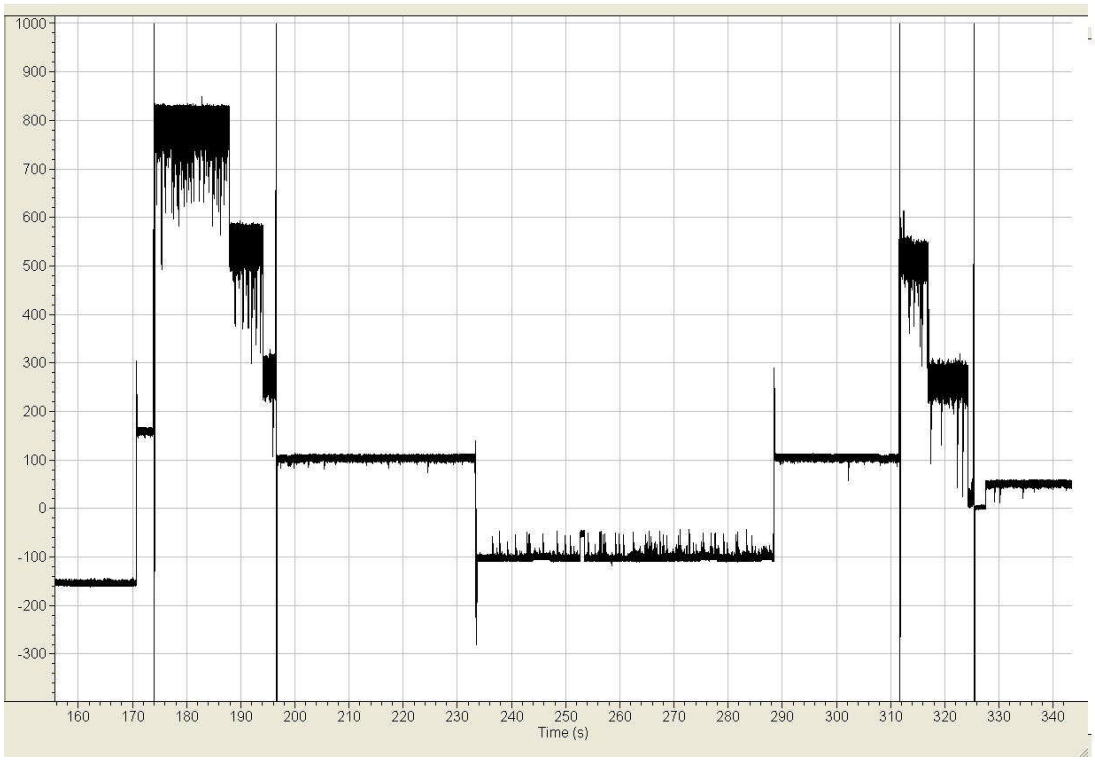

Figure 4.3.1.3 Experiment of single channel conductance measurement with varied voltages. At time before 170s, the voltage was set to -50mV, following by +50mV, then the voltage was jumped to +250mV where sequential steps closure took place. When the voltage was set back to +50mV, the current was no longer as the same as at previous +50mV (100pA), as well as did at -50mV.

Porins are also known to oscillate spontaneously between open and closed states at low voltages (Delcour, 2002). In a detailed examination of the fully open traces of OmpC20 and OmpC33, we observed a slightly different pattern of short-lived events at -50mV (Figure 4.3.1.4). In OmpC33 there is an additional closure event corresponding to around 28% of conductivity (both OmpC33 and OmpC20 show a 9% closure event). This short lived event is not seen for OmpC20 suggesting that the OmpC33 trimer is more conformational flexible than OmpC20.

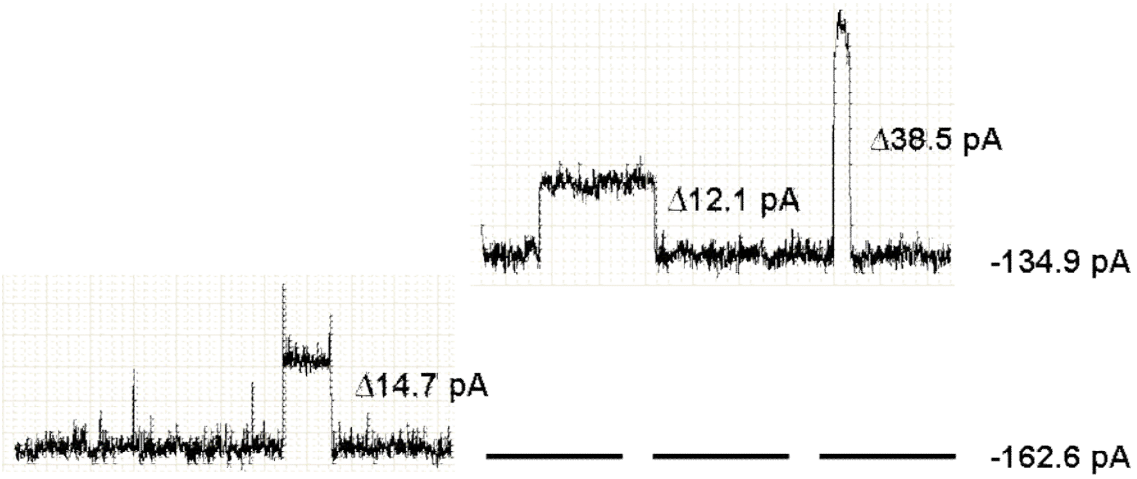

Figure 4.3.1.4 Traces of open channels of OmpC20 (bottom) and OmpC33 (above) under -50 mV shows different short-lived transition events. In OmpC20, the closing current is about 9% (Δ14.7pA) of original; in OmpC33, the closing current is either 9% (Δ12.1pA) or 29% (Δ38.5pA).

4.3.2 Antibiotic (gentamicin) interaction with OmpC20 and OmpC33

Once the picture of trimeric conductance is clear, we wished to investigate the interaction of antibiotics with OmpC20 and OmpC33. Molecular dynamics study suggested there is only one ampicillin molecule moving through the monomeric channel of OmpF (Nestorovich et al., 2002); our structure OmpC26 with partial HEPES molecule bound supported this suggestion (see Chapter 3). Therefore, before carrying out the experiment, it is known that only one antibiotic molecule can pass through the OmpC monomeric channel.

We used the single channel conductance measurement as the control. A series of antibiotics were tested to see the interaction (data not shown) and only gentamicin gave clear signals. We preceeded with the experiment with gentamicin. It is worth mentioning that gentamicin itself does not penetrate nor break down the bilayer. Experiments with gentamicin at a concentration of 300μM added to the *cis* chamber solution (no porin addition) showed no interaction with a stable bilayer within 10 minutes of stirring, the traces after adding gentamicin therefore reveal the interaction of gentamicin and OmpC channel.

When a porin was inserted into the bilayer, gentamicin induces closure of a single open OmpC20 pore (Figure 4.3.2.1). It triggers several types of closing events. In a completely open pore, the most time-enduring events are about 25% closure of original current. Double blockages decreasing the current by nearly two thirds can be also seen (Figure

4.3.2.1). We interpret this type of event as gentamicin passing through the monomers as seen on the report with ampicillin interact with OmpF (Nestorovich et al., 2002).

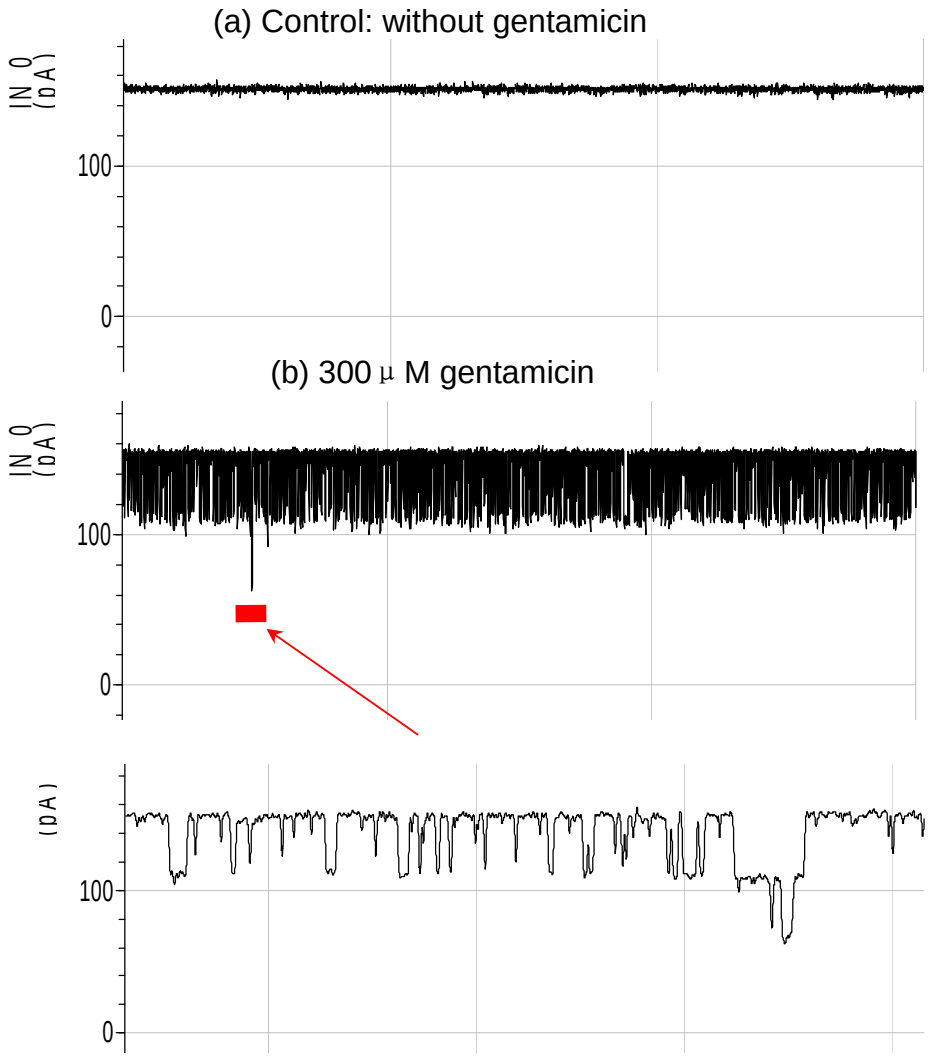

Figure 4.3.2.1 Gentamicin interacting with an open pore of OmpC20. Measurement was under +50mV. Time scale is 3s for both (a) and (b). (c) is 3000X zoom in of the red part of (b). (a) without gentamicin, the current trace was stable; (b) With gentamicin addition, there's increased noise (spikes) among which the majority is about 1/3 current reduction

that corresponding to one monomer blockage. There's also 2/3 current reduction which indicates two monomers blockage.

Investigation on the interaction of OmpC33 with gentamicin is largely hindered because of the noisy traces of OmpC33 itself. Most ofen, the channel disappeared from the bilayer after a short while, therefore recording the data became extremely difficult. Comparing to the traces of OmpC20 interacting with gentamicin, OmpC33 rarely has double blockages (Figure 4.3.2.2). This suggests that it is harder for gentamicin to get through OmpC33 than OmpC20.

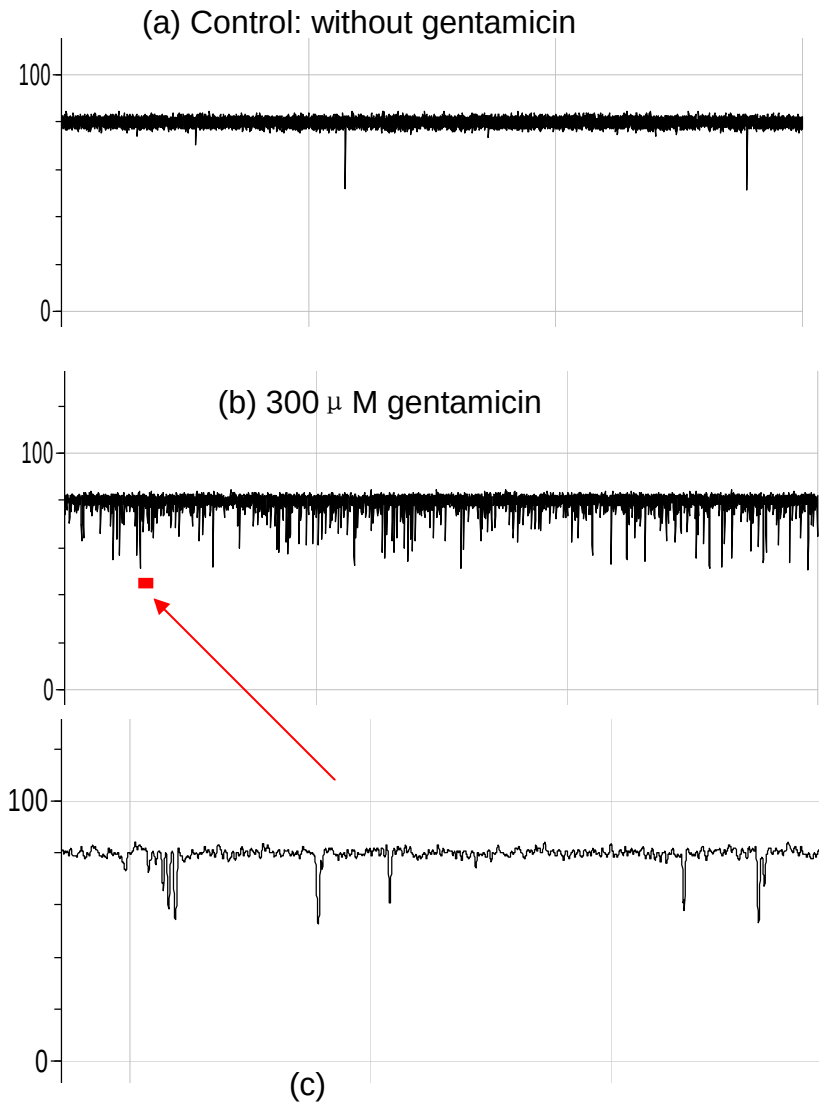

Figure 4.3.2.2 Gentamicin interacts with an OmpC33 open pore. Measurement was under +50mV at room temperature. (a) In the control experiment (without gentamicin added), the pore itself has short-time closure corresponding to nearly one third of the whole channel conductance. (b) Gentamicin induces channel closure in many forms, however, no double blockage was observed as with OmpC20. (c) zoom in the red part of (b).

4.3.3 Thermal stability

From the single channel experiment, particularly the experiment of gentamicin interaction with OmpC channel, we observed that OmpC33 might not be as stable structurally as OmpC20. To test this hypothesis, we tested the thermal stability of trimers. Using SDS-PAGE (see methods) we observed that OmpC33 runs as a monomer (rather than trimer) at above 60 ºC whereas the equivalent transition for OmpC20 is around 70 ºC (figure 4.3.3.1).

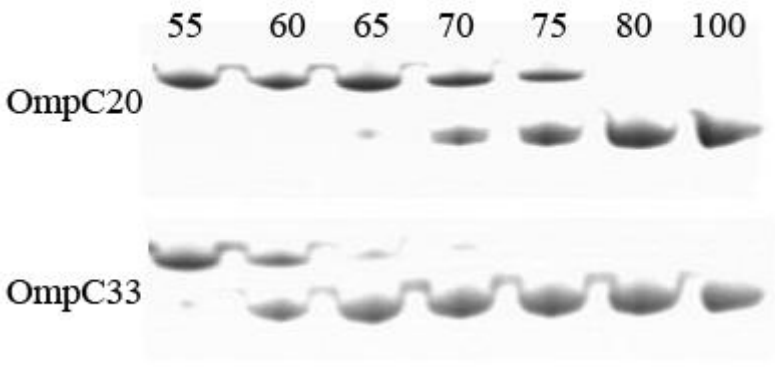

Figure 4.3.3.1. Comparison of thermal stability between OmpC20 and OmpC33. The temperatures (ºC) are indicated at the top.

4.4. Discussion and Conclusion

In this chapter, single ion conductance measurement was carried out to characterize the channel properties of the OmpC mutants; gentamicin interaction with OmpC20 and OmpC33 was also investigated. The small ion flow through OmpC20 and OmpC33 are very similar suggesting that the pore size is unaffected by mutation. This would seem to disfavour a mechanism of simply narrowing to explain antibiotic resistance. The conductivity experiments show the existence of conducting sub-states in OmpC20 and OmpC33. Evidence for such states had been reported in OmpF (Basle et al., 2004; Buehler et al., 1991).The molecular mechanism by which porins open and close is not clear. Some outer membrane protein crystal structures show the inward directed loop to have different conformations under different pH (Yildiz et al., 2006) or upon ligand binding (Ferguson et al., 2002b; Ferguson et al., 1998; Locher et al., 1998; Yue et al., 2003) suggesting that the inward directed loop is flexible. Many have suggested that conformational changes in this loop underpin the changes in channel conductance. OmpC33 compared to OmpC20 exhibits a short lived but significant (approx 30%) closure event. Our interpretation of this result is that L3 in OmpC33 is more conformationally dynamic than in OmpC20. Recent modelling studies have proposed that the involvement of L3 in voltage-dependent closure of porins (Delcour, 2008). The redistribution of ions within the pore change the electrostatics that bind the L3 loop to the barrel wall (Delcour, 1997) might lead to changes in L3 structure and closure of the channel.

Experiments of gentamicin interaction with OmpC20 and OmpC33 show that this antibiotic triggers closures of OmpC channels. Although gentamicin does not depend on the OmpC pathway to go through the outer membrane, the molecular size (~477Da) is well within porin's limitation to take up hydrophilic nutrients (~600Da). Gentamicin may serve as a model molecule to study the interaction of other antibiotic with OmpC. It is intriguing that with OmpC20 gentamicin seems to go through the channel as similar interaction pattern was found in ampicillin interacting with OmpF (Nestorovich et al., 2002). However, OmpC33, with only 3 amino acids change from OmpC20, undergoes a different interation pattern as no double closure was observed which indicates the difficulty for gentamicin go through this porin. The flexibility of OmpC33 structure might play an important role to protect the cell when encountering deadly foreign compounds.

That OmpC33 might be less conformational stable was also seen in a crude test of protein stability. The OmpC33 trimer breaks down into monomers in SDS gel loading buffer at 10ºC lower than OmpC20. Although the 60ºC temperature at which this happens, and the presence of SDS are not biologically relevant, it does point to a quite significant perturbation in stability.

In summary, with the data of structural information, the results showed molecular evidence for a rationale of how changes in OmpC contribute to clinically observed antibiotic resistance. Bacteria may have clever strategy to cope with harsh environment by developing subtle changes within some important proteins. The study here presents the

channels are functional but block the drugs. These findings should help us understand how antibiotic resistance develops.

Chapter 5

Crystallization of a new outer membrane protein Wzi from *E. coli*

Summary

This project dealt with a new outer membrane protein that is involved in the biosynthesis and translocation mechanism of K30 antigen from *E. coli*. The mechanism is a complicated process that requires several proteins including outer and inner membrane proteins. In order to gain insight into the mechanism it is essential to solve the structures of the proteins and understand how they interact with each other. In this study, Wzi, a new outer membrane protein was investigated. The protein was successfully expressed, purified and crystallized. Initial crystals were tested and diffracted to 15 Å. A robust optimization process was established and better quality crystals were obtained. A crystal which diffracted to 2.4Å has been obtained.

5.1 Introduction

5.1.1 *E. coli* Capsules

E. coli residing in the human gastrointestinal tract in general are not harmful, however, they sometimes can be toxic causing a number of diseases including gastro-intestinal and urinary tract infections, meningitis, and septicemia (Corbett and Roberts, 2008). The reason for this transition is that toxic *E. coli* are capable of expression of a polysaccharide capsule or K antigen which is a strong virulence factor. The capsule is a layer of high-molecular-weight acidic polysaccharides that are tightly attached to the cell surface (Whitfield, 2006). There are about 80 different K antigens in *E. coli* with varying sugar compositions and polysaccharide linkages. Recently the capsules are divided into four groups based on their genetics and biosynthesis (Whitfield and Roberts, 1999). Only group 1 and 4 are synthesized and assembled via the Wzy-dependent pathway (Whitfield, 2006). Our laboratory is particularly interested in the biosynthesis of group 1 capsules and we are focusing on the *E. coli* K30 serotype which is the prototype.

5.1.2 Wzy-dependent pathway

In the Wzy-dependent pathway (Figure 5.1.2.1), undecaprenol pyrophosphate (und-PP)-linked repeat units are compiled by glycosyltransferases at the cytoplasmic face inside the inner membrane (Drummelsmith and Whitfield, 1999). The inner membrane protein Wzx, a putative flippase, facilitates the transport of the repeat units across the inner membrane (Whitfield, 2006). These repeat units are then polymerized by Wzy at the

periplasmic face. Wzy is an enzyme that transfers the polymer chain to the incoming und-PP-linked repeat unit. The next step involves Wzc, an inner membrane protein with tyrosinase autokinase activity. Wzc is only active when its C-terminal tyrosine residue is phosphorylated (Whitfield, 2006). The level of phosphorylation of Wzc has some impact on the capsular polysaccharides production (Paiment et al., 2002). Subsequently, Wzb, a phosphatase enzyme that dephosphorylates Wzc, also takes part in the polymer expression. After polymerization, Wza, the α-helical octameric outer membrane lipoprotein acts as an export channel for the glycopolymer (Dong et al., 2006). Wzi is the last protein in the Wzy-dependent pathway and has been shown to play a late role in the capsular assembly pathway (Rahn et al., 2003).

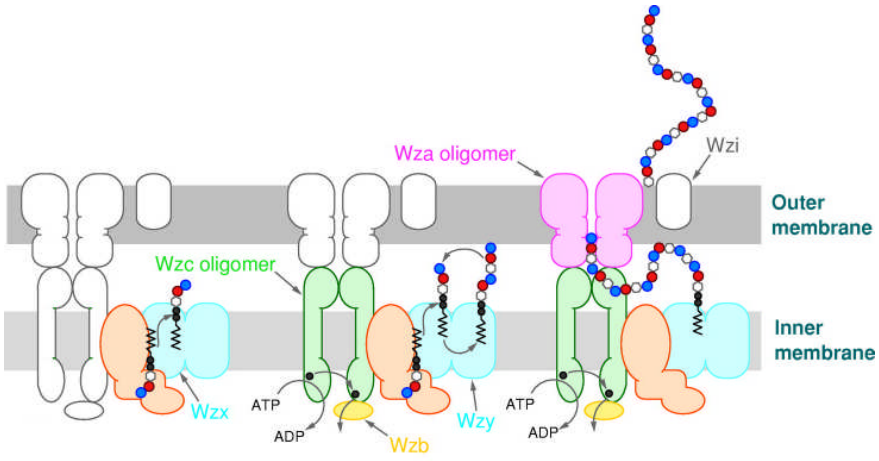

Figure 5.1.2.1 The Wzy-dependent pathway of group 1 and 4 capsular polysaccharides biosynthesis and assembly in *E. coli*.

5.1.3 Wzi and aim of this project

Our laboratory has been engaging the capsular synthesis and assembly pathway by solving the structures of important proteins. Structures of Wza (Dong et al., 2006) and, more recently Wzb (Hagelueken et al., 2009) have been solved and published. As an ongoing effort, it is important to solve the structure of each protein that is involved in this pathway. Wzi is predicted to be an outer membrane β-barrel protein (Rahn et al., 2003). With the experience of successfully purifying and crystallizing the OmpC outer membrane protein, it is easier to apply these techniques to another β-barrel protein.

Apart from Wza, Wzi is the second outer membrane protein involved in the capsule synthesis and assembly pathway (Rahn et al., 2003). Studies of Wzi mutant strain showed a significant reduction of capsule production on the cell surface (Rahn et al., 2003) suggesting that Wzi is important. Although it is believed that Wzi might serve as a late role in the capsular assembly pathway (Rahn et al., 2003), the exact function is not yet known. This might largely depend on the structure that awaits to be solved.

5.2 Material and Methods

5.2.1 Expression, extraction and purification of Wzi

The DH5α *E. coli* cells containing the plasmid vector pWQ193 which is a pBAD24 derivative was provided by our collaborator Prof. C. Whitfield at Guelph University, Canada (Rahn et al., 2003). The pWQ193 vector contained the required gene coding for ampicillin resistance and overexpression of the target protein from the *E. coli* B44 (O9:K30) strain. *E. coli* DH5α cells containing the antibiotic ampicillin (100 µl/ml, Roche Diagnostics GmbH) were grown in LB medium at 37°C. Cells were grown to an OD_{600} of 0.8 and were induced with 0.02% L-arabinose. After induction with L-arabinose, cells were grown for a further 5 hours to achieve a maximum protein production. The cells were collected by centrifugation at 6,000g (Beckman-Coulter™ with JLA 8.1000 rotor) and used directly for next steps of purification or stored as a paste at -80°C.

Cells harvested from the fermentation were typically resuspended in 200mL (this volume varied, usually the ratio of buffer to paste was 5:1) 20mM sodium phosphate buffer (pH 7.4) plus 50mM sodium chloride. Bacterial cells were mixed to a homogenous state before passing through cell disruptor. Cells were disrupted twice at 30Kpsi and the crude extract was fractionated by ultracentrifugation (100,000g) for 1 hour at 4°C (Beckman-Coulter Optima™ L-90K Ultracentrifuge with 70Ti rotor). The supernatant solution was discarded and the pellet containing cell membranes was re-suspended in 200mL 20mM sodium phosphate, pH7.4, 50mM sodium chloride with 2% N-lauryl

sarcosine (Sigma Aldrich) to solubilise the inner membranes (Filip et al., 1973). The crude extracts were incubated at room temperature with rolling for 4 hours. The extract went through ultracentrifugation again at 100,000g for 1 hour at 4°C. The supernatant solution was then discarded and the pellet containing the outer membranes was re-suspended in 200mL 20mM sodium phosphate, pH7.4, 50mM sodium chloride with 0.5% SB3.14 (Sigma Aldrich). The membranes were incubated with rolling overnight at room temperature. The insoluble materials were then removed by centrifugation at 100,000g for 1 hour at 4°C.

As for the OmpC (Chapter 3), a similar two-step purification strategy was applied to purify Wzi. Affinity and size exclusion chromatography were used. All purifications were carried out with an AKTA purifier. The first step is the affinity chromatography using a 5ml chelating nickel column (HisTrap™ FF, GE Healthcare) which was equilibrated with 20mM sodium phosphate, 500mM sodium chloride and 0.05% SB3.14 (Sigma Aldrich). Wzi is C-terminal hexa-histidine tagged, this ensures its effectiveness of binding to the Nickel column. Once bound, the detergent in the running buffer is changed to 0.1% LDAO (Anatrace, 99.96% purity). The protein is step-washed by a series of imidazole concentrations: 0mM, 12.5mM, 25mM, 50mM, 100mM, and 500mM (Figure 5.2.1.1). Protein eluted corresponding to every peak was checked by SDS-PAGE (Figure 5.2.1.1) and the target protein Wzi was pooled.

Further experiments used the detergents β-OG (1%) (Melford Laboratories Ltd.) OPOE (0.5%) (Bachem, UK Ltd.) and C_8E_4 (0.45%) (Anatrace, 99.93% purity) instead of LDAO.

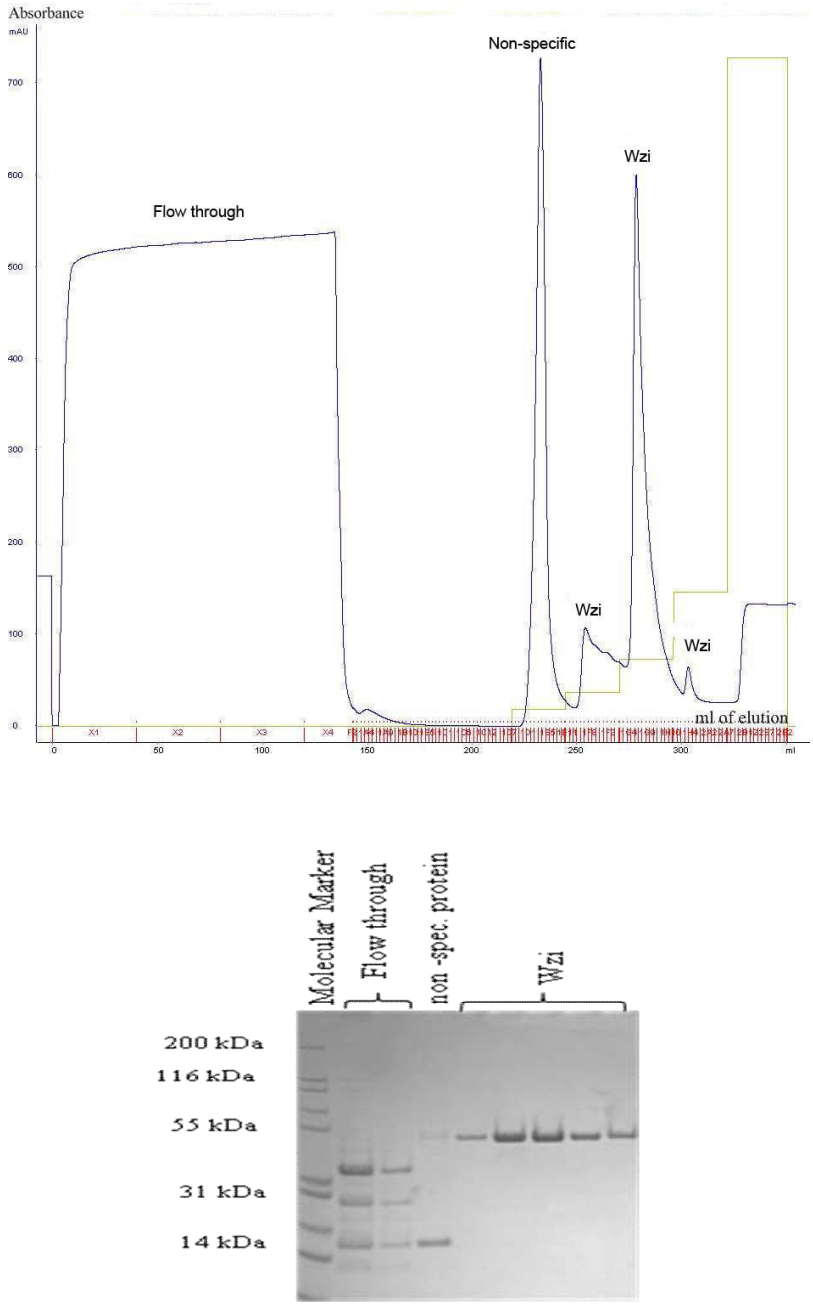

Figure 5.2.1.1 Nickel affinity chromatography for Wzi purification and protein purity checked by SDS-PAGE.

A further step of purification, gel filtration, was applied to remove the aggregates, lipids and imidazole (Figure 5.2.1.2). The running buffer was 20mM Tris-HCl with the detergent used in the last step of Nickel affinity chromatography. Protein purity was checked again by SDS-PAGE (Figure 5.2.1.2) and protein identity was checked by Mass-spec (Figure 5.2.1.3). Trypsin digestion finger-printing shows the matching sequence of Wzi is 61% as shown red below:

```
  1 AQAYAAGLVV NDNDLRNDLA WLSDRGVIHL SLSTWPLSQE EIARALKKAK
 51 PSYSSEQVVL ARINQRLSAL KADFRVTGYT STDQPGTPQG FGQTQPADNS
101 LGLAFNNSGE WWDVHLQGNV EGGERISNGS RFNANGAYGA VKFWNQWLSF
151 GQVPQWWGPG YEGSLIRGDA MRPMTGFLMQ RAEQAAPETW WLRWVGPWQY
201 QISASQMNQY NAVPHAKIIG GRFTFSPIQS LELGASRIMQ WGGKGRPESL
251 SNFWDGLTGK DNTAANDPNE PGNQLAGFDF KFKLEPTLGW PVSFYGQMIG
301 EDESGFLPSA NMFLGGIEGH HGWGKDAVNW YLEAHDTRTN MSRTNYSYTH
351 HIYKDGYYQQ GYPLGDAMGG DGQLVAGKVE LITEDNQRWS TRLVYAKVNP
401 ENQSINKAFP HADTLKGIQL GWSGDVYQSV RLNTSLWYTN ANNSDSDDVG
451 ASAGIEIPFS L
```

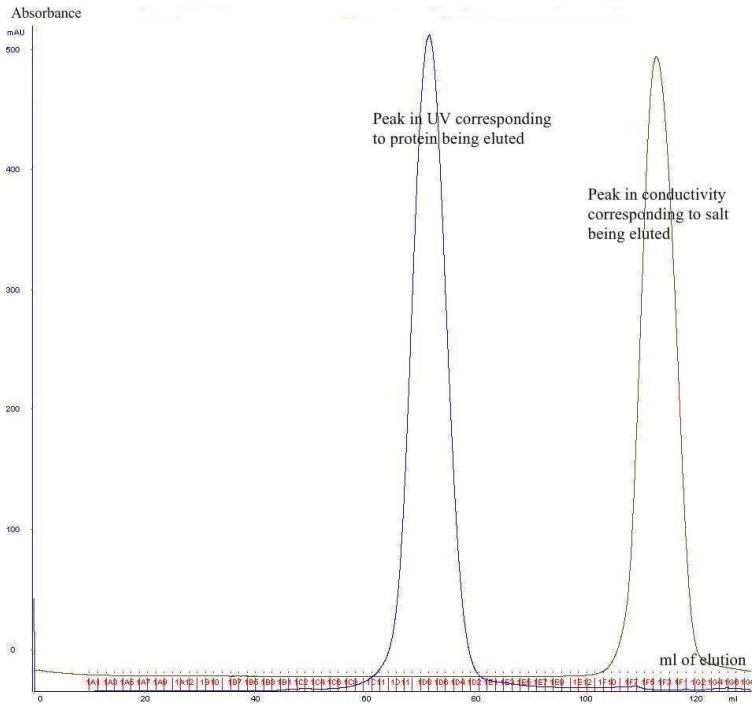

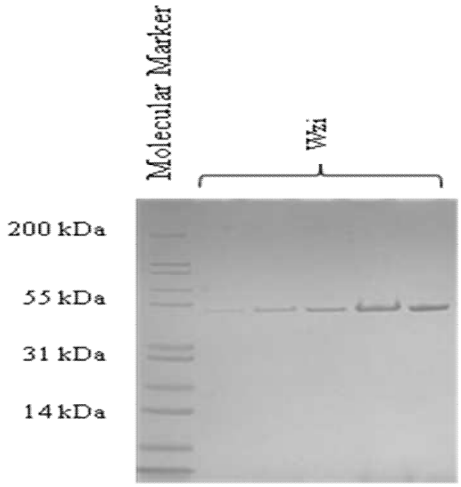

Figure 5.2.1.2 Gel filtration and SDS-PAGE. Protein sample was quite pure after this step as indicated by the gel.

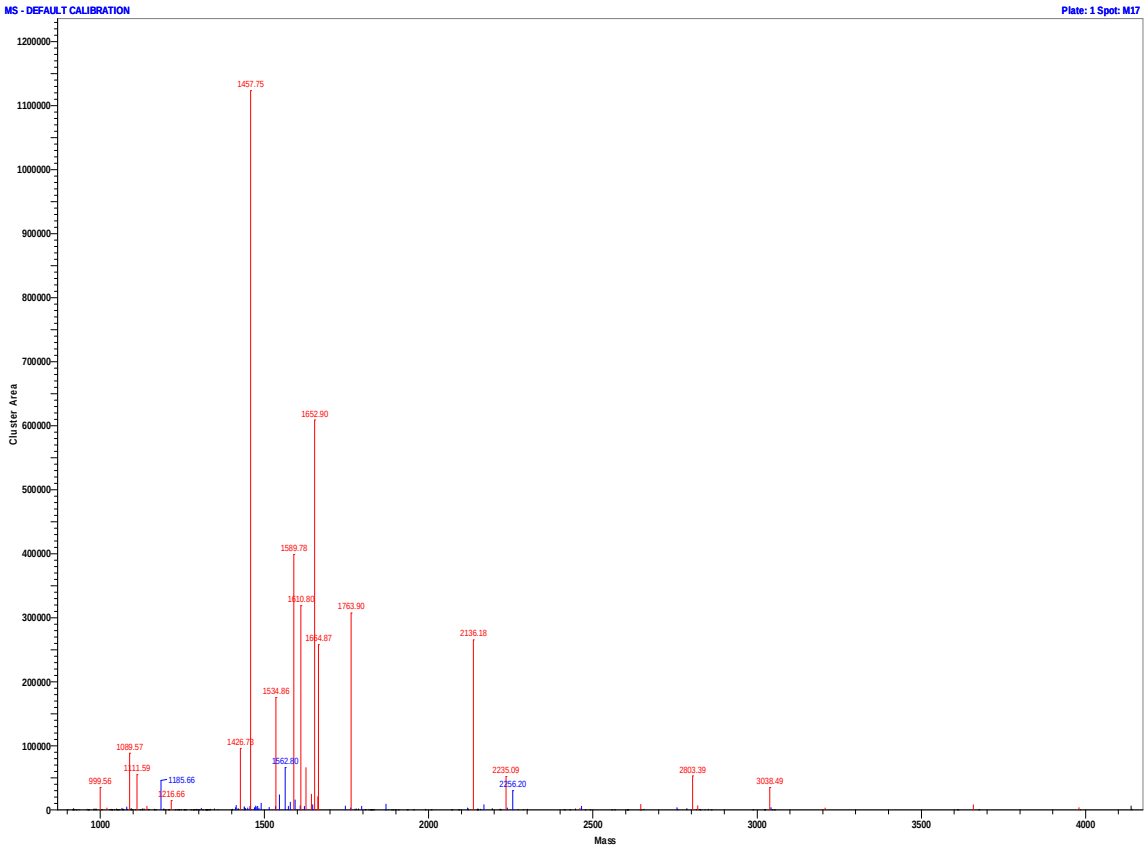

Figure 5.2.1.3 Matching mass for Wzi after trypsin digestion. The red spikes are the peptides that matching the amino sequence of Wzi. The blue spikes are noise.

5.2.2 Initial crystallization of Wzi

Prior to any crystallization experiments, the protein solution was treated by ultracentrifugation (100,000g, 1hour, 277K) to remove aggregates. Crystallization trials were performed using the screen Memplus™ (Molecular Dimensions Limited), MembFac™ (Hampton Research) or the Sigma™ screen (BioChemika). The protein concentration used for crystallization was 8-19 mg/ml. The sitting drop vapor diffusion technique was applied throughout the screening and optimization process, with protein drops of 2 µl and a 1:1 ratio of protein: precipitant set up against 100 µl of reservoir solution. The crystallization trials were set up both at cold room temperature (4°C) and room temperature (20°C). A summary of the crystallization trials is listed in Table 5.2.2.1. Crystals with different shapes appeared after a couple of days up to weeks even months in different conditions (Figure 5.2.2.1).

Table 5.2.2.1 Crystallization conditions for Wzi (C-his_6) protein.

Detergent	**Screen**	**Protein Concentration (mg ml^{-1})**	**Method**	**Temperature**
0.1% LDAO	Memplus	11.4	SD[1]	20°C
0.1% LDAO	Memplus	19.1	SD	20°C
0.1% LDAO	Memplus	12.5	SD	4°C
0.1% LDAO	Membfac	10.8	SD	4°C
0.1% LDAO	Sigma	10.8	SD	4°C
1% β-OG	Memplus	12.8	HD[2]	20°C
1% β-OG	Memplus	12.8	HD	20°C
1% β-OG	Memplus	8	SD	4°C
1% β-OG	Membfac	8	SD	4°C
1% β-OG	Sigma	8	SD	4°C
0.45% C8E4	Memplus	11.39	SD	4°C
0.45% C8E4	Membfac	11.39	SD	4°C
0.45% C8E4	Sigma	11.39	SD	4°C

SD[1]: Sitting drop; HD[2]: Hanging drop.

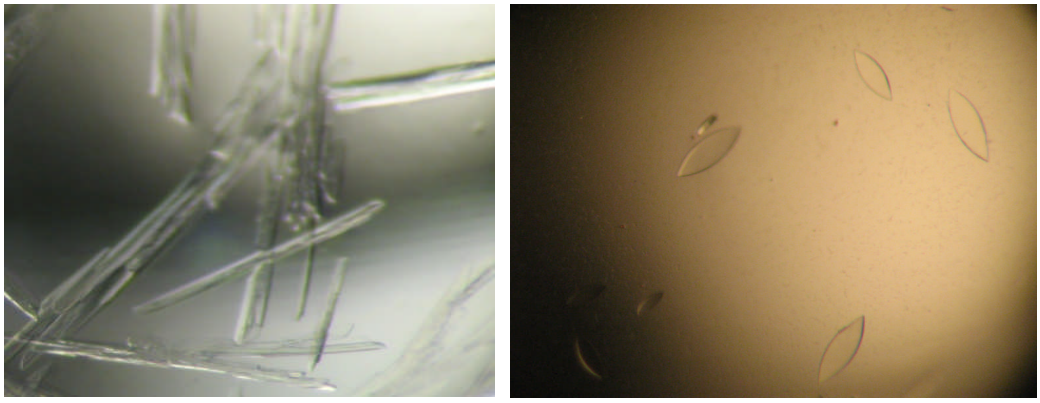

Figure 5.2.2.1 Different crystal forms of Wzi purified in 0.1% LDAO obtained in two different conditions. Left: crystal observed in one week in MemPlus™ condition #15 at 4°C: 0.1M sodium chloride, 0.1M EPPS (pH 8.0) and PEG 1500 (33% w/v). Right: crystals grew after two months in the condition of MemPlus™ condition #17 at 4°C: 0.1M sodium cacodylate (pH 6.5), PEG 2000 MME (12.5% w/v).

5.2.3 X-ray characterisation and optimization of wzi crystals

Crystals were frozen by placing them into liquid nitrogen prior to screening at our in-house X-ray facility. Crystals were cryo-protected using a step-wise soaking strategy. Briefly, the soaking solution with high concentration of glycerol (~20%) or PEG400 (30%) as final cryoprotectant is defined 100%, soaking solutions without any cryoprotectant is defined 0%. The step-wise soaking usually go through from 0%, 10%, 50% and 100%. Initial crystals diffracted to 20 Å (data not shown) from the condition: 0.1M sodium chloride, 0.1M EPPS (pH 8.0) and PEG 1500 (33% w/v). After two months a crystal diffracted to

~10Å at Diamond beamline (Figure 5.2.3.1) from a new condition: 0.1M sodium cacodylate (pH 6.5), PEG 2000 MME (12.5% w/v).

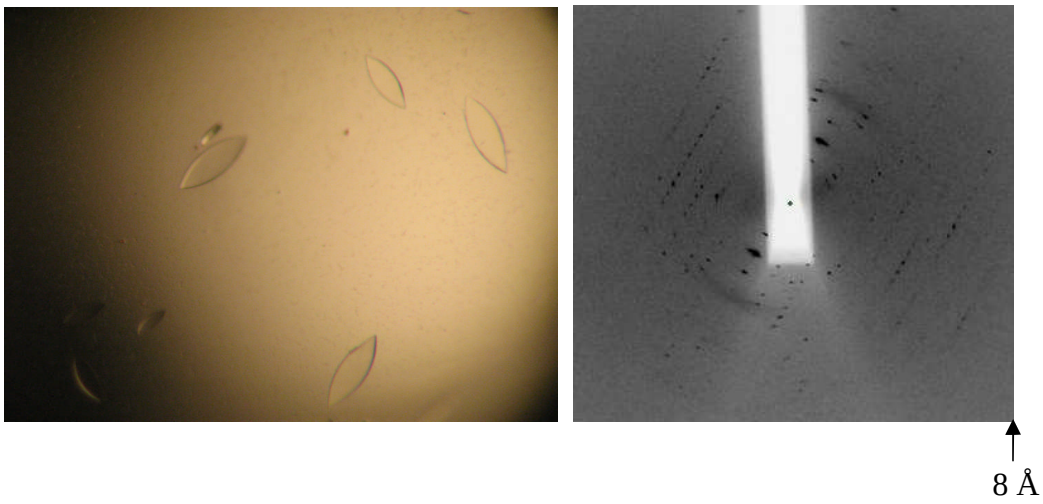

Figure 5.2.3.1 Crystals that diffracted to ~10 Å at Diamond beamline. The condition was at cold room temperature (4°C), protein purified in 0.1% LDAO with concentration of 12.5mg/ml, Memplus screen condition No.17: 0.1M sodium cacodylate pH 6.5, 12.5% (w/v) PEG 2000 MME, with protein solution 2µl plus 2µl mother liquor, after 2 months of incubation, diffraction to ~10 Å shown in the picture right.

Optimised crystallisation trials were set up using the conditions in Table 5.2.3.1 as a base, a number of salts were added as well as glycerol and the additive 1,2,3-heptanetriol. Summary from recent publications on outer membrane proteins crystallization suggest 1,2,3-heptanetriol is the most successful additive so far (Newstead et al., 2008). Table 5.2.3.2 summaries the salts and additives used for optimisation.

Table 5.2.3.1 Optimisation conditions originated from the initial growth condition: 0.1M sodium cacodylate (pH6.5), PEG2000 MME 12.5% as highlighted in the table.

Tube #	Buffer	pH	Percipitant
1	0.1M sodium cacodylate	6.25	PEG2000 MME 8%
2	0.1M sodium cacodylate	6.25	PEG2000 MME 10%
3	0.1M sodium cacodylate	6.25	PEG2000 MME 12.5%
4	0.1M sodium cacodylate	6.25	PEG2000 MME 14%
5	0.1M sodium cacodylate	6.25	PEG2000 MME 16%
6	0.1M sodium cacodylate	6.25	PEG2000 MME 18%
7	0.1M sodium cacodylate	6.5	PEG2000 MME 8%
8	0.1M sodium cacodylate	6.5	PEG2000 MME 10%
9	0.1M sodium cacodylate	6.5	PEG2000 MME 12.5%
10	0.1M sodium cacodylate	6.5	PEG2000 MME 14%
11	0.1M sodium cacodylate	6.5	PEG2000 MME 16%
12	0.1M sodium cacodylate	6.5	PEG2000 MME 18%
13	0.1M sodium cacodylate	6.75	PEG2000 MME 8%
14	0.1M sodium cacodylate	6.75	PEG2000 MME 10%
15	0.1M sodium cacodylate	6.75	PEG2000 MME 12.5%
16	0.1M sodium cacodylate	6.75	PEG2000 MME 14%
17	0.1M sodium cacodylate	6.75	PEG2000 MME 16%
18	0.1M sodium cacodylate	6.75	PEG2000 MME 18%
19	0.1M sodium cacodylate	7	PEG2000 MME 8%
20	0.1M sodium cacodylate	7	PEG2000 MME 10%
21	0.1M sodium cacodylate	7	PEG2000 MME 12.5%
22	0.1M sodium cacodylate	7	PEG2000 MME 14%
23	0.1M sodium cacodylate	7	PEG2000 MME 16%
24	0.1M sodium cacodylate	7	PEG2000 MME 18%

Table 5.2.3.2 Salts and additives used for Wzi crystallization optimisation.

Additive Name	Concentration
NaCl	0.1M; 0.2M; 0.3M
$CaCl_2$	0.1M
$MgCl_2$	0.1M
Li_2SO_4	0.1M
Glycerol	10%, 20%
1,2,3-heptanetriol	1.5%

Within two weeks, in contrast to two months initially, crystals started to form in several conditions and the size was generally bigger than previously obtained (Figure 5.2.3.2)

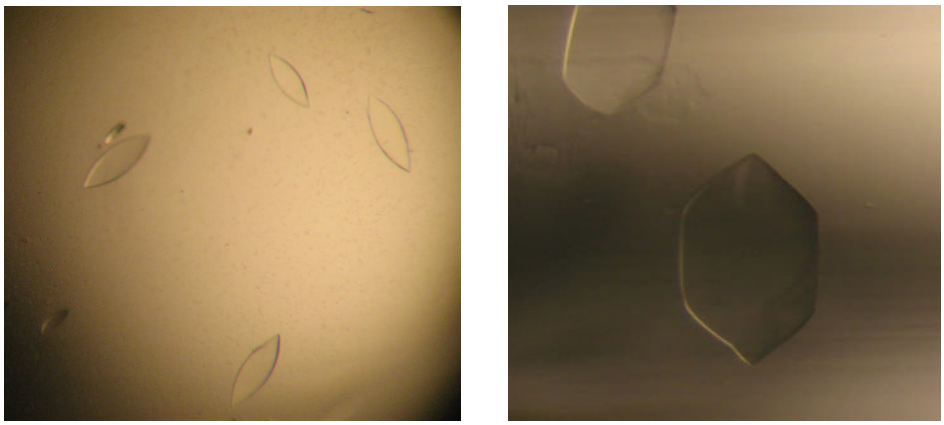

Figure 5.2.3.2 Crystal forms before (left) and after (right) optimisation. Microscope zooming scale was the same level.

The diffraction resolution was also improved, with one crystal diffracted to 4Å using our in-house X-ray facility (Figure 5.2.3.3). However, the diffraction pattern was anisotropic that a dataset was not collectable.

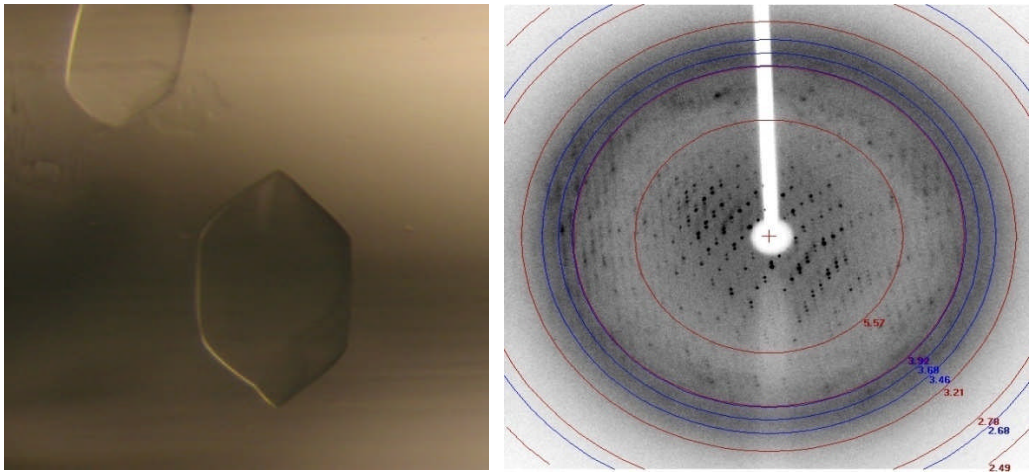

Figure 5.2.3.3 Crystals diffracted to ~4 Å at in-house X-ray facility. The growth condition was at cold room temperature (4°C), protein purified in 0.1% LDAO with concentration of 12.5mg/ml in 0.1M sodium cacodylate pH 6.5, 12.5% (w/v) PEG 2000 MME, with protein solution 2µl plus 2µl mother liquor, after two weeks of incubation.

We also tested the crystals grown in the other optimized conditions, Table 5.2.3.3 summaries the crystals that had been tested. All of these crystals diffracted to 5-7Å at the highest resolution range, however, no dataset was collected as the diffraction pattern was quite anisotropic.

Table 5.2.3.3 Summary of crystals analysed by in-house X-ray facility.

Buffer	**pH**	**Precipitant**	**Salt**	**Detergent**	**Protein Conc.** (mg/ml)
0.1M sodium cacodylate	6.25	8% PEG 2000 MME	0.1M Li_2SO_4	0.1% LDAO	12.5
0.1M sodium cacodylate	6.25	10% PEG 2000 MME	0.1M Li_2SO_4	0.1% LDAO	12.5
0.1M sodium cacodylate	6.25	12.5% PEG 2000 MME	0.1M Li_2SO_4	0.1% LDAO	12.5
0.1M sodium cacodylate	6.5	14% PEG 2000 MME	0.M Li_2SO_4	0.1% LDAO	12.5
0.1M sodium cacodylate	6.25	8% PEG 2000 MME	-	0.1% LDAO	12.5
0.1M sodium cacodylate	6.25	10% PEG 2000 MME	-	0.1% LDAO	12.5
0.1M sodium cacodylate	6.25	10% PEG 2000 MME	0.1M NaCl	0.1% LDAO	12.5
0.1M sodium cacodylate	6.25	14% PEG 2000 MME	0.1M NaCl	0.1% LDAO	12.5
0.1M sodium cacodylate	6.25	16% PEG 2000 MME	0.1M NaCl	0.1% LDAO	12.5
0.1M sodium cacodylate	6.5	14% PEG 2000 MME	0.1M NaCl	0.1% LDAO	12.5
0.1M sodium cacodylate	6.5	18% PEG 2000 MME	0.1M NaCl	0.1% LDAO	12.5
0.1M sodium cacodylate	6.25	18% PEG 2000 MME	0.1M $MgCl_2$	0.1% LDAO	12.5

The additives listed in Table 5.2.3.2 do not have same effect on Wzi crystallization, as shown in table 5.2.3.3, the salt Li_2SO_4 and NaCl gave more hits than other salts. This suggestions that the salt Li_2SO_4 and NaCl might be more favored in comparison with other salt/additives. We therefore set up a further optimized kit focusing on the salt Li_2SO_4 and NaCl. Table 5.2.3.4 summarized the conditions that were used for the further optimization.

Table 5.2.3.4 Further optimization conditions for Wzi crystallization.

0.1M Sodium Cacodylate pH 6.25/pH6.0						
PEG2000 MME	Salts					
	Li_2SO_4	Li_2SO_4	Li_2SO_4+NaCl	NaCl	NaCl	NaCl+Li_2SO_4
8%	0.1M	0.05M	0.05M+0.05M	0.05M	0.1M	0.1M+0.1M
10%	0.1M	0.05M	0.05M+0.05M	0.05M	0.1M	0.1M+0.1M
12%	0.1M	0.05M	0.05M+0.05M	0.05M	0.1M	0.1M+0.1M
14%	0.1M	0.05M	0.05M+0.05M	0.05M	0.1M	0.1M+0.1M

5.2.4 X-ray data collection

Crystals started to grow within two weeks in the second round optimized conditions. One of the crystals from the following condition diffracted to 2.4Å at Diamond beamline IO4: protein purified in 0.1% LDAO with a concentration of 12.5 mg/ml, 0.1M sodium cacodylate pH 6.25, PEG2000 MME 14%, 0.1M NaCl, in cold room temperature.

Data were processed with MOSFLM (Leslie, 2006). Indexing of two diffraction images (0°, 90°) indicated the crystal had a space group of P222, with unit-cell parameters a=64.2Å, b=64.5Å, c=159.9Å, α=β=γ=90°. A 90° of data was collected with exposure time 5s for each 0.5° image. The X-rays had a wavelength of 0.971Å. Data were integrated in MOSFLM but further scaling using the program SCALA was not successful. Attempts using HKL2000 and XDS also failed to scale the data. Careful investigation into the diffraction images revealed that the crystal had deteriorated after 35° rotation (Figure 5.2.4.1).

(A) (B)

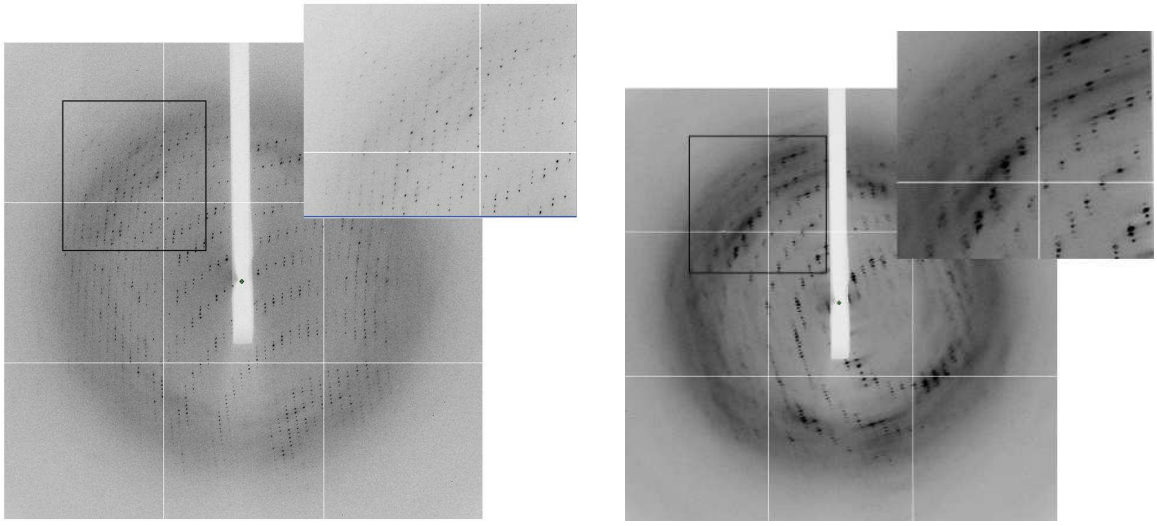

Figure 5.2.4.1 X-ray diffraction pattern of Wzi C-terminal histidine tagged protein crystal, collected at Diamond IO4. (A) Diffraction pattern at 0°, the highest resolution is about 2.4 Å at the edge. (B) Diffraction pattern after 35° rotation the spots became smeary and the highest resolution dropped down to less than 3.0 Å.

5.2.5 Is Wzi a monomer?

Previous studies suggested that Wzi is a monomer in solution (Rahn et al., 2003). This conclusion was based on dynamic light scattering and SDS-PAGE. Dynamic light scattering predicted a molecular mass of 52KDa which is in agreement with the monomeric behaviour. The result from SDS-PAGE is less clear. We wished to check the possibility of Wzi being a monomer by applying the gel filtration technique. A sample of mixtures of proteins with known molecular mass was used as the background standard. The peaks in the chromatogram with corresponding molecular weights appeared in an

order as shown in figure 5.2.5.1. The peak for Wzi-His_6 appeared at approximately the position of ovalbumim, which has a molecular mass of 44kDa. This result is in agreement with other data that suggests Wzi is more likely a monomer.

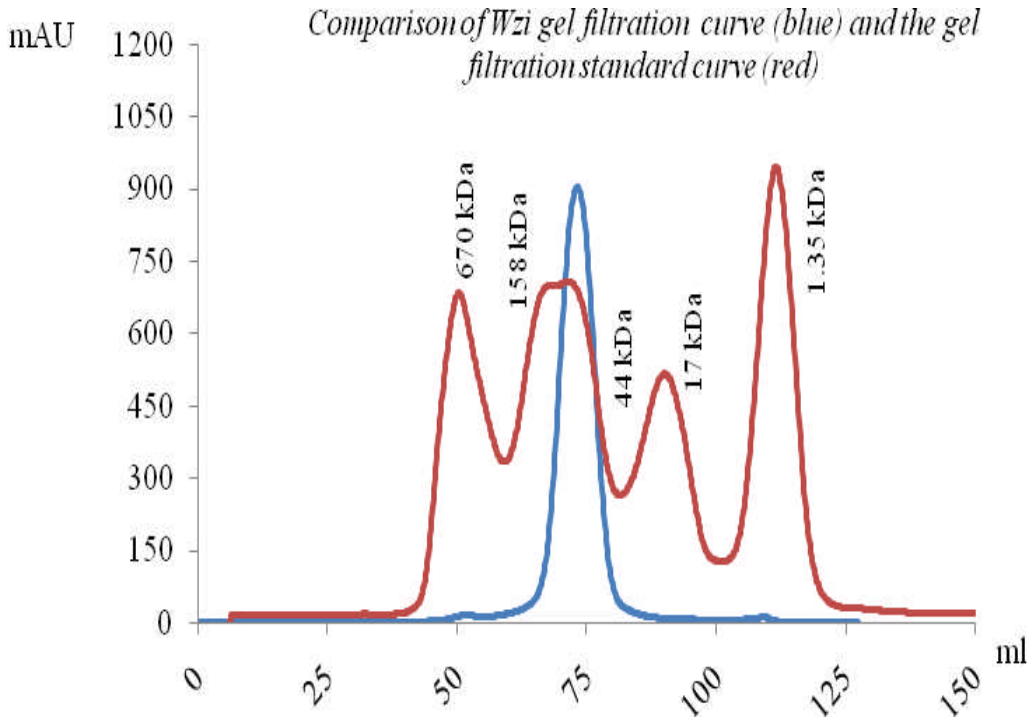

Figure 5.2.5.1 Gel filtration of Wzi-His_6 (blue curve) and the standard proteins (red curve). The peaks in the red curve correspond to the following proteins with order: The first peak is thyroglobulin (MW 670,000 Da); the second peak corresponds to γ-globulin (MW: 158,000 Da); the third belongs to ovalbumin (MW: 44,000 Da), four belongs to myoglobin (MW: 17,000 Da) and peak five corresponds to the small protein vitamin B_{12} (MW: 1,350 Da).

5.2.6 Structure prediction by online server

The sequence of Wzi starting from AQA was submitted to the Phyre serve (**P**rotein **H**omology/analog**Y** **R**ecognition **E**ngine) for structure prediction (Kelley and Sternberg, 2009). Developed by Imperial College London, Phyre uses homologies or analogies of known protein structure to predict new protein structure (Kelley and Sternberg, 2009). By submitting the amino acids sequence to the server, a predicted PDB file is sent back and the predicted structure can be investigated.

5.3 Discussions and prospectives

Wzi has been successfully purified and crystallized. There has been no publication yet on Wzi crystals. However, Wzi was previously crystallized and the best diffraction resolution was 20Å (K. Beis, PhD thesis, University of St Andrews). Here the crystal quality has been significantly improved and higher resolution has been achieved to 2.4Å. The parameters: temperature, salts (additives), buffer pH and the choice of detergents, that influence the crystallization process were investigated. For Wzi C-his_6 protein, cold room temperature turns out to be more successful than normal room temperature. Small salts like NaCl and Li_2SO_4 facilitates the crystallization. The detergent LDAO is the most successful one in comparison with other choices.

It was previously suggested that Wzi is a β-barrel protein (Rahn et al., 2003). Results from Phyre server indicated that Wzi is highly likely a β-barrel. Residue 114 to 459 was predicted to be an open β-barrel with 12 β-strands, as shown in figure 5.3.1. The shape of the predicted β-barrel is like the monomer of OmpC porin. However with the first 114 residues missing, the β-barrel from X-ray crystal structure might have different shape or even more strands as there's still room left. In an attempt to predict the structure of the first 114 residues of Wzi, Phyer gave a model for the first 77 residues as shown in Figure 5.3.2. This N-terminal three helix motif has been seen in 14 β-strands outer membrane protein TodX and FadL as described in Figure 1.3.4.6, Chapter 1. Both TodX and FadL are transporters. It is possible that Wzi shares a similar structure with these 14 β-strands

proteins, however, the inwarded loop inside the barrel in figure 5.3.1 has to be placed elsewhere in that case. Wzi is probably a completely new structure that is not seen before.

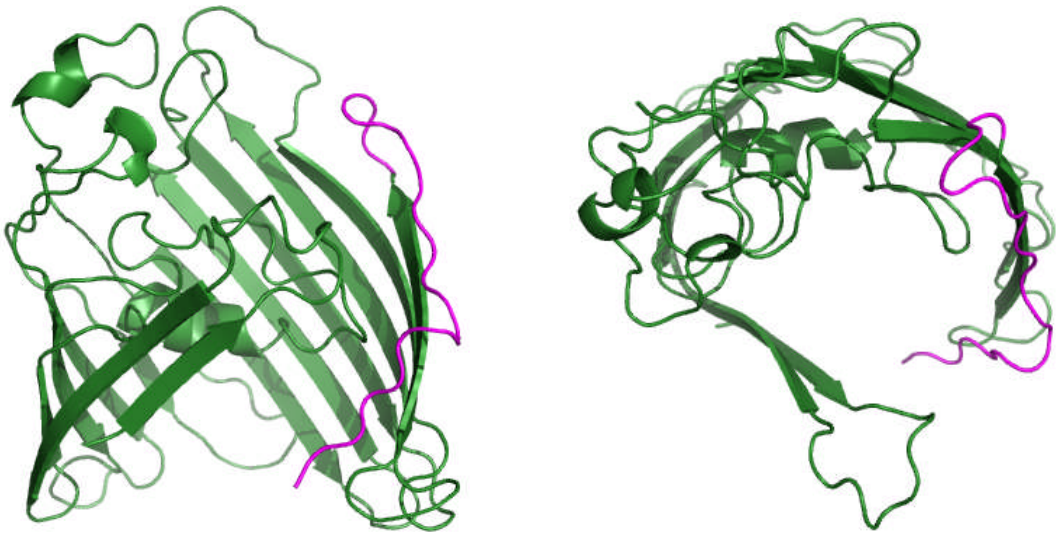

Figure 5.3.1 Cartoon model of Wzi predicted by Phyre server from residues 114 to 459. The C terminal loop is colored mengenta.

Figure 5.3.2 Cartoon model of Wzi from residue 2 to 77.

The crystallised form of Wzi in this project is C-terminal His_6 tagged. For future work, further crystallization optimization might be desirable. From the predicted structure model, there are extracellular long loops especially at the C-terminal (colored mengenta). The long

loops are usually structurally flexible thus bring disorders to affect the crystal quality. The C-terminal residues may be truncated to make it shorter loop. Homologues of Wzi found in *K. pneumoniae* (Rahn et al. 2003) could be cloned and the structure of the homologue may provide more amenable crystals. As no homologous' structures have been known yet, it might be desirable to use heavy metal soaking strategy for solving the structure. 12 or 14 β-strands known structures can be used as models for molecular replacement to reveal the Wzi β-barrel. For its functional properties, single channel conductance measurement might provide some insights. Wzi crystals soaking with polysaccharides might also provide detailed information on the structure and function relationship.

References

Ahn, V. E., Lo, E. I., Engel, C. K., Chen, L., Hwang, P. M., Kay, L. E., Bishop, R. E., and Prive, G. G. (2004). A hydrocarbon ruler measures palmitate in the enzymatic acylation of endotoxin. Embo J *23*, 2931-2941.

Akama, H., Kanemaki, M., Yoshimura, M., Tsukihara, T., Kashiwagi, T., Yoneyama, H., Narita, S., Nakagawa, A., and Nakae, T. (2004). Crystal structure of the drug discharge outer membrane protein, OprM, of *Pseudomonas aeruginosa*: dual modes of membrane anchoring and occluded cavity end. J Biol Chem *279*, 52816-52819.

Babic, M., Hujer, A. M., and Bonomo, R. A. (2006). What's new in antibiotic resistance? Focus on beta-lactamases. Drug Resist Updat *9*, 142-156.

Baneyx, F. (1999). Recombinant protein expression in *Escherichia coli*. Curr Opin Biotechnol *10*, 411-421.

Barnard, T. J., Dautin, N., Lukacik, P., Bernstein, H. D., and Buchanan, S. K. (2007). Autotransporter structure reveals intra-barrel cleavage followed by conformational changes. Nat Struct Mol Biol *14*, 1214-1220.

Basle, A., Iyer, R., and Delcour, A. H. (2004). Subconductance states in OmpF gating. Biochim Biophys Acta *1664*, 100-107.

Basle, A., Rummel, G., Storici, P., Rosenbusch, J. P., and Schirmer, T. (2006). Crystal structure of osmoporin OmpC from *E. coli* at 2.0 Å. J Mol Biol *362*, 933-942.

Berridge, M. V., Herst, P. M., and Tan, A. S. (2005). Tetrazolium dyes as tools in cell biology: new insights into their cellular reduction. Biotechnol Annu Rev *11*, 127-152.

Bishop, N. D., Lea, E. J., Mobasheri, H., and Spiro, S. (1996). Altered voltage sensitivity of mutant OmpC porin channels. FEBS Lett *379*, 295-298.

Biswas, S., Mohammad, M. M., Movileanu, L., and van den Berg, B. (2008). Crystal structure of the outer membrane protein OpdK from *Pseudomonas aeruginosa*. Structure *16*, 1027-1035.

Biswas, S., Mohammad, M. M., Patel, D. R., Movileanu, L., and van den Berg, B. (2007). Structural insight into OprD substrate specificity. Nat Struct Mol Biol *14*, 1108-1109.

Bredin, J., Saint, N., Mallea, M., De, E., Molle, G., Pages, J. M., and Simonet, V. (2002). Alteration of pore properties of *Escherichia coli* OmpF induced by mutation of key residues in anti-loop 3 region. Biochem J *363*, 521-528.

Buchanan, S. K., Lukacik, P., Grizot, S., Ghirlando, R., Ali, M. M., Barnard, T. J., Jakes, K. S., Kienker, P. K., and Esser, L. (2007). Structure of colicin I receptor bound to the R-domain of colicin Ia: implications for protein import. Embo J *26*, 2594-2604.

Buehler, L. K., Kusumoto, S., Zhang, H., and Rosenbusch, J. P. (1991). Plasticity of *Escherichia coli* porin channels. Dependence of their conductance on strain and lipid environment. J Biol Chem *266*, 24446-24450.

Byrne, B., and Iwata, S. (2002). Membrane protein complexes. Curr Opin Struct Biol *12*, 239-243.

Chevalier, J., Pages, J. M., Eyraud, A., and Mallea, M. (2000). Membrane permeability modifications are involved in antibiotic resistance in *Klebsiella pneumoniae*. Biochem Biophys Res Commun *274*, 496-499.

Chimento, D. P., Mohanty, A. K., Kadner, R. J., and Wiener, M. C. (2003). Substrate-induced transmembrane signaling in the cobalamin transporter BtuB. Nat Struct Biol *10*, 394-401.

Clantin, B., Delattre, A. S., Rucktooa, P., Saint, N., Meli, A. C., Locht, C., Jacob-Dubuisson, F., and Villeret, V. (2007). Structure of the membrane protein FhaC: a member of the Omp85-TpsB transporter superfamily. Science *317*, 957-961.

Cobessi, D., Celia, H., Folschweiller, N., Schalk, I. J., Abdallah, M. A., and Pattus, F. (2005). The crystal structure of the pyoverdine outer membrane receptor FpvA from *Pseudomonas aeruginosa* at 3.6 angstroms resolution. J Mol Biol *347*, 121-134.

Corbett, D., and Roberts, I. S. (2008). Capsular polysaccharides in *Escherichia coli*. Adv Appl Microbiol *65*, 1-26.

Corpet, F. (1988). Multiple sequence alignment with hierarchical clustering. Nucleic Acids Res *16*, 10881-10890.

Cowan, S. W., Schirmer, T., Rummel, G., Steiert, M., Ghosh, R., Pauptit, R. A., Jansonius, J. N., and Rosenbusch, J. P. (1992). Crystal structures explain functional properties of two *E. coli* porins. Nature *358*, 727-733.

Danelon, C., Nestorovich, E. M., Winterhalter, M., Ceccarelli, M., and Bezrukov, S. M. (2006). Interaction of zwitterionic penicillins with the OmpF channel facilitates their translocation. Biophys J *90*, 1617-1627.

Davies, J. (1994). Inactivation of antibiotics and the dissemination of resistance genes. Science *264*, 375-382.

Delcour, A. H. (1997). Function and modulation of bacterial porins: insights from electrophysiology. FEMS Microbiol Lett *151*, 115-123.

Delcour, A. H. (2002). Structure and function of pore-forming beta-barrels from bacteria. J Mol Microbiol Biotechnol *4*, 1-10.

Delcour, A. H. (2003). Solute uptake through general porins. Front Biosci *8*, d1055-1071.

Delcour, A. H. (2008). Outer membrane permeability and antibiotic resistance. Biochim Biophys Acta.

Denizot, F., and Lang, R. (1986). Rapid colorimetric assay for cell growth and survival. Modifications to the tetrazolium dye procedure giving improved sensitivity and reliability. J Immunol Methods *89*, 271-277.

Dong, C., Beis, K., Nesper, J., Brunkan-Lamontagne, A. L., Clarke, B. R., Whitfield, C., and Naismith, J. H. (2006). Wza the translocon for *E. coli* capsular polysaccharides defines a new class of membrane protein. Nature *444*, 226-229.

Doyle, D. A., Morais Cabral, J., Pfuetzner, R. A., Kuo, A., Gulbis, J. M., Cohen, S. L., Chait, B. T., and MacKinnon, R. (1998). The structure of the potassium channel: molecular basis of K+ conduction and selectivity. Science *280*, 69-77.

Drummelsmith, J., and Whitfield, C. (1999). Gene products required for surface expression of the capsular form of the group 1 K antigen in *Escherichia coli* (O9a:K30). Mol Microbiol *31*, 1321-1332.

Dutzler, R., Rummel, G., Alberti, S., Hernandez-Alles, S., Phale, P., Rosenbusch, J., Benedi, V., and Schirmer, T. (1999). Crystal structure and functional characterization of OmpK36, the osmoporin of *Klebsiella pneumoniae*. Structure *7*, 425-434.

Evans, P. (2006). Scaling and assessment of data quality. Acta Crystallogr D Biol Crystallogr *62*, 72-82.

Faller, M., Niederweis, M., and Schulz, G. E. (2004). The structure of a mycobacterial outer-membrane channel. Science *303*, 1189-1192.

Federici, L., Du, D., Walas, F., Matsumura, H., Fernandez-Recio, J., McKeegan, K. S., Borges-Walmsley, M. I., Luisi, B. F., and Walmsley, A. R. (2005). The crystal structure of the outer membrane protein VceC from the bacterial pathogen *Vibrio cholerae* at 1.8 Å resolution. J Biol Chem *280*, 15307-15314.

Ferguson, A. D., Chakraborty, R., Smith, B. S., Esser, L., van der Helm, D., and Deisenhofer, J. (2002b). Structural basis of gating by the outer membrane transporter FecA. Science *295*, 1715-1719.

Ferguson, A. D., and Deisenhofer, J. (2002). TonB-dependent receptors-structural perspectives. Biochim Biophys Acta *1565*, 318-332.

Ferguson, A. D., Hofmann, E., Coulton, J. W., Diederichs, K., and Welte, W. (1998). Siderophore-mediated iron transport: crystal structure of FhuA with bound lipopolysaccharide. Science *282*, 2215-2220.

Filip, C., Fletcher, G., Wulff, J. L., and Earhart, C. F. (1973). Solubilization of the cytoplasmic membrane of *Escherichia coli* by the ionic detergent sodium-lauryl sarcosinate. J Bacteriol *115*, 717-722.

Forst, D., Welte, W., Wacker, T., and Diederichs, K. (1998). Structure of the sucrose-specific porin ScrY from *Salmonella typhimurium* and its complex with sucrose. Nat Struct Biol *5*, 37-46.

Gouaux, E. (1997). Channel-forming toxins: tales of transformation. Curr Opin Struct Biol *7*, 566-573.

Grinius, L., Dreguniene, G., Goldberg, E. B., Liao, C. H., and Projan, S. J. (1992). A staphylococcal multidrug resistance gene product is a member of a new protein family. Plasmid *27*, 119-129.

Hagelueken, G., Huang, H., Mainprize, I. L., Whitfield, C., and Naismith, J. H. (2009). Crystal structures of Wzb of *Escherichia coli* and CpsB of *Streptococcus pneumoniae*, representatives of two families of tyrosine phosphatases that regulate capsule assembly. J Mol Biol *392*, 678-688.

Harder, K. J., Nikaido, H., and Matsuhashi, M. (1981). Mutants of Escherichia coli that are resistant to certain beta-lactam compounds lack the ompF porin. Antimicrob Agents Chemother *20*, 549-552.

Hearn, E. M., Patel, D. R., and van den Berg, B. (2008). Outer-membrane transport of aromatic hydrocarbons as a first step in biodegradation. Proc Natl Acad Sci U S A *105*, 8601-8606.

Hernandez-Alles, S., Alberti, S., Alvarez, D., Domenech-Sanchez, A., Martinez-Martinez, L., Gil, J., Tomas, J. M., and Benedi, V. J. (1999). Porin expression in clinical isolates of *Klebsiella pneumoniae*. Microbiology *145 (Pt 3)*, 673-679.

Hong, H., Patel, D. R., Tamm, L. K., and van den Berg, B. (2006). The outer membrane protein OmpW forms an eight-stranded beta-barrel with a hydrophobic channel. J Biol Chem *281*, 7568-7577.

Hunte, C., Koepke, J., Lange, C., Rossmanith, T., and Michel, H. (2000). Structure at 2.3 A resolution of the cytochrome bc(1) complex from the yeast *Saccharomyces cerevisiae* co-crystallized with an antibody Fv fragment. Structure *8*, 669-684.

Hunte, C., and Michel, H. (2002). Crystallisation of membrane proteins mediated by antibody fragments. Curr Opin Struct Biol *12*, 503-508.

Iwata, S., Ostermeier, C., Ludwig, B., and Michel, H. (1995). Structure at 2.8 A resolution of cytochrome c oxidase from Paracoccus denitrificans. Nature *376*, 660-669.

Iyer, R., and Delcour, A. H. (1997). Complex inhibition of OmpF and OmpC bacterial porins by polyamines. J Biol Chem *272*, 18595-18601.

James, C. E., Mahendran, K. R., Molitor, A., Bolla, J. M., Bessonov, A. N., Winterhalter, M., and Pages, J. M. (2009). How beta-lactam antibiotics enter bacteria: a dialogue with the porins. PLoS One *4*, e5453.

Jiang, Y., Lee, A., Chen, J., Ruta, V., Cadene, M., Chait, B. T., and MacKinnon, R. (2003). X-ray structure of a voltage-dependent K+ channel. Nature *423*, 33-41.

Karshikoff, A., Spassov, V., Cowan, S. W., Ladenstein, R., and Schirmer, T. (1994). Electrostatic properties of two porin channels from *Escherichia coli*. J Mol Biol *240*, 372-384.

Kelley, L. A., and Sternberg, M. J. (2009). Protein structure prediction on the Web: a case study using the Phyre server. Nat Protoc *4*, 363-371.

Kim, S., Malinverni, J. C., Sliz, P., Silhavy, T. J., Harrison, S. C., and Kahne, D. (2007). Structure and function of an essential component of the outer membrane protein assembly machine. Science *317*, 961-964.

Kleivdal, H., Benz, R., Tommassen, J., and Jensen, H. B. (1999). Identification of positively charged residues of FomA porin of Fusobacterium nucleatum which are important for pore function. Eur J Biochem *260*, 818-824.

Koronakis, V. (2003). TolC--the bacterial exit duct for proteins and drugs. FEBS Lett *555*, 66-71.

Koronakis, V., Sharff, A., Koronakis, E., Luisi, B., and Hughes, C. (2000). Crystal structure of the bacterial membrane protein TolC central to multidrug efflux and protein export. Nature *405*, 914-919.

Kreusch, A., and Schulz, G. E. (1994). Refined structure of the porin from Rhodopseudomonas blastica. Comparison with the porin from *Rhodobacter capsulatus*. J Mol Biol *243*, 891-905.

Kumar, A., and Schweizer, H. P. (2005). Bacterial resistance to antibiotics: active efflux and reduced uptake. Adv Drug Deliv Rev *57*, 1486-1513.

Lambert, P. A. (2005). Bacterial resistance to antibiotics: modified target sites. Adv Drug Deliv Rev *57*, 1471-1485.
Leslie, A. G. (2006). The integration of macromolecular diffraction data. Acta Crystallogr D Biol Crystallogr *62*, 48-57.
Levy, S. B. (1998). The challenge of antibiotic resistance. Sci Am *278*, 46-53.
Lewis, K. (1994). Multidrug resistance pumps in bacteria: variations on a theme. Trends Biochem Sci *19*, 119-123.
Liu, N., and Delcour, A. H. (1998). The spontaneous gating activity of OmpC porin is affected by mutations of a putative hydrogen bond network or of a salt bridge between the L3 loop and the barrel. Protein Eng *11*, 797-802.
Livermore, D. M. (1998). Beta-lactamase-mediated resistance and opportunities for its control. J Antimicrob Chemother *41 Suppl D*, 25-41.
Locher, K. P., Rees, B., Koebnik, R., Mitschler, A., Moulinier, L., Rosenbusch, J. P., and Moras, D. (1998). Transmembrane signaling across the ligand-gated FhuA receptor: crystal structures of free and ferrichrome-bound states reveal allosteric changes. Cell *95*, 771-778.
Low, A. S., MacKenzie, F. M., Gould, I. M., and Booth, I. R. (2001). Protected environments allow parallel evolution of a bacterial pathogen in a patient subjected to long-term antibiotic therapy. Mol Microbiol *42*, 619-630.
Marger, M. D., and Saier, M. H., Jr. (1993). A major superfamily of transmembrane facilitators that catalyse uniport, symport and antiport. Trends Biochem Sci *18*, 13-20.
Massova, I., and Mobashery, S. (1998). Kinship and diversification of bacterial penicillin-binding proteins and beta-lactamases. Antimicrob Agents Chemother *42*, 1-17.
Medeiros, A. A., O'Brien, T. F., Rosenberg, E. Y., and Nikaido, H. (1987). Loss of OmpC porin in a strain of *Salmonella typhimurium* causes increased resistance to cephalosporins during therapy. J Infect Dis *156*, 751-757.
Meng, G., Surana, N. K., St Geme, J. W., 3rd, and Waksman, G. (2006). Structure of the outer membrane translocator domain of the Haemophilus influenzae Hia trimeric autotransporter. Embo J *25*, 2297-2304.
Mobasheri, H., and Lea, E. J. (2002). Biophysics of gating phenomena in voltage-dependent OmpC mutant porin channels (R74C and R37C) of *Escherichia coli* outer membranes. Eur Biophys J *31*, 389-399.
Moeck, G. S., and Coulton, J. W. (1998). TonB-dependent iron acquisition: mechanisms of siderophore-mediated active transport. Mol Microbiol *28*, 675-681.
Montal, M., and Mueller, P. (1972). Formation of bimolecular membranes from lipid monolayers and a study of their electrical properties. Proc Natl Acad Sci U S A *69*, 3561-3566.
Moraes, T. F., Bains, M., Hancock, R. E., and Strynadka, N. C. (2007). An arginine ladder in OprP mediates phosphate-specific transfer across the outer membrane. Nat Struct Mol Biol *14*, 85-87.
Mosmann, T. (1983). Rapid colorimetric assay for cellular growth and survival: application to proliferation and cytotoxicity assays. J Immunol Methods *65*, 55-63.

Movileanu, L., Howorka, S., Braha, O., and Bayley, H. (2000). Detecting protein analytes that modulate transmembrane movement of a polymer chain within a single protein pore. Nat Biotechnol *18*, 1091-1095.

Mueller, M., Grauschopf, U., Maier, T., Glockshuber, R., and Ban, N. (2009). The structure of a cytolytic alpha-helical toxin pore reveals its assembly mechanism. Nature *459*, 726-730.

Murshudov, G. N., Vagin, A. A., and Dodson, E. J. (1997). Refinement of macromolecular structures by the maximum-likelihood method. Acta Crystallogr D Biol Crystallogr *53*, 240-255.

Nestorovich, E. M., Danelon, C., Winterhalter, M., and Bezrukov, S. M. (2002). Designed to penetrate: time-resolved interaction of single antibiotic molecules with bacterial pores. Proc Natl Acad Sci U S A *99*, 9789-9794.

Neu, H. C. (1992). The crisis in antibiotic resistance. Science *257*, 1064-1073.

Newstead, S., Hobbs, J., Jordan, D., Carpenter, E. P., and Iwata, S. (2008). Insights into outer membrane protein crystallization. Mol Membr Biol *25*, 631-638.

Nikaido, H. (1994a). Prevention of drug access to bacterial targets: permeability barriers and active efflux. Science *264*, 382-388.

Nikaido, H. (2003). Molecular basis of bacterial outer membrane permeability revisited. Microbiol Mol Biol Rev *67*, 593-656.

Nikaido, H., and Nakae, T. (1979). The outer membrane of Gram-negative bacteria. Adv Microb Physiol *20*, 163-250.

Nikaido, H., and Saier, M. H., Jr. (1992). Transport proteins in bacteria: common themes in their design. Science *258*, 936-942.

Olesky, M., Hobbs, M., and Nicholas, R. A. (2002). Identification and analysis of amino acid mutations in porin IB that mediate intermediate-level resistance to penicillin and tetracycline in *Neisseria gonorrhoeae*. Antimicrob Agents Chemother *46*, 2811-2820.

Oomen, C. J., van Ulsen, P., van Gelder, P., Feijen, M., Tommassen, J., and Gros, P. (2004). Structure of the translocator domain of a bacterial autotransporter. Embo J *23*, 1257-1266.

Ostermeier, C., Essen, L. O., and Michel, H. (1995). Crystals of an antibody Fv fragment against an integral membrane protein diffracting to 1.28 Å resolution. Proteins *21*, 74-77.

Pages, J. M., James, C. E., and Winterhalter, M. (2008). The porin and the permeating antibiotic: a selective diffusion barrier in Gram-negative bacteria. Nat Rev Microbiol *6*, 893-903.

Paiment, A., Hocking, J., and Whitfield, C. (2002). Impact of phosphorylation of specific residues in the tyrosine autokinase, Wzc, on its activity in assembly of group 1 capsules in *Escherichia coli*. J Bacteriol *184*, 6437-6447.

Painter, J., and Merritt, E. A. (2006). Optimal description of a protein structure in terms of multiple groups undergoing TLS motion. Acta Crystallogr D Biol Crystallogr *62*, 439-450.

Parker, M. W., and Feil, S. C. (2005). Pore-forming protein toxins: from structure to function. Prog Biophys Mol Biol *88*, 91-142.

Pautsch, A., and Schulz, G. E. (1998). Structure of the outer membrane protein A transmembrane domain. Nat Struct Biol *5*, 1013-1017.

Pawelek, P. D., Croteau, N., Ng-Thow-Hing, C., Khursigara, C. M., Moiseeva, N., Allaire, M., and Coulton, J. W. (2006). Structure of TonB in complex with FhuA, *E. coli* outer membrane receptor. Science *312*, 1399-1402.

Phale, P. S., Philippsen, A., Kiefhaber, T., Koebnik, R., Phale, V. P., Schirmer, T., and Rosenbusch, J. P. (1998). Stability of trimeric OmpF porin: the contributions of the latching loop L2. Biochemistry *37*, 15663-15670.

Phale, P. S., Philippsen, A., Widmer, C., Phale, V. P., Rosenbusch, J. P., and Schirmer, T. (2001). Role of charged residues at the OmpF porin channel constriction probed by mutagenesis and simulation. Biochemistry *40*, 6319-6325.

Phale, P. S., Schirmer, T., Prilipov, A., Lou, K. L., Hardmeyer, A., and Rosenbusch, J. P. (1997). Voltage gating of *Escherichia coli* porin channels: role of the constriction loop. Proc Natl Acad Sci U S A *94*, 6741-6745.

Poole, K., Krebes, K., McNally, C., and Neshat, S. (1993). Multiple antibiotic resistance in *Pseudomonas aeruginosa*: evidence for involvement of an efflux operon. J Bacteriol *175*, 7363-7372.

Prince, S. M., Achtman, M., and Derrick, J. P. (2002). Crystal structure of the OpcA integral membrane adhesin from *Neisseria meningitidis*. Proc Natl Acad Sci U S A *99*, 3417-3421.

Pugsley, A. P., and Schnaitman, C. A. (1978). Identification of three genes controlling production of new outer membrane pore proteins in *Escherichia coli* K-12. J Bacteriol *135*, 1118-1129.

Raetz, C. R., and Whitfield, C. (2002). Lipopolysaccharide endotoxins. Annu Rev Biochem *71*, 635-700.

Rahn, A., Beis, K., Naismith, J. H., and Whitfield, C. (2003). A novel outer membrane protein, Wzi, is involved in surface assembly of the *Escherichia coli* K30 group 1 capsule. J Bacteriol *185*, 5882-5890.

Remaut, H., Tang, C., Henderson, N. S., Pinkner, J. S., Wang, T., Hultgren, S. J., Thanassi, D. G., Waksman, G., and Li, H. (2008). Fiber formation across the bacterial outer membrane by the chaperone/usher pathway. Cell *133*, 640-652.

Saier, M. H., Jr., Tam, R., Reizer, A., and Reizer, J. (1994). Two novel families of bacterial membrane proteins concerned with nodulation, cell division and transport. Mol Microbiol *11*, 841-847.

Saint, N., Lou, K. L., Widmer, C., Luckey, M., Schirmer, T., and Rosenbusch, J. P. (1996). Structural and functional characterization of OmpF porin mutants selected for larger pore size. II. Functional characterization. J Biol Chem *271*, 20676-20680.

Schirmer, T., Keller, T. A., Wang, Y. F., and Rosenbusch, J. P. (1995). Structural basis for sugar translocation through maltoporin channels at 3.1 Å resolution. Science *267*, 512-514.

Schmitt, E. K., Vrouenraets, M., and Steinem, C. (2006). Channel activity of OmpF monitored in nano-BLMs. Biophys J *91*, 2163-2171.

Shultis, D. D., Purdy, M. D., Banchs, C. N., and Wiener, M. C. (2006). Outer membrane active transport: structure of the BtuB:TonB complex. Science *312*, 1396-1399.

Simonet, V., Mallea, M., Fourel, D., Bolla, J. M., and Pages, J. M. (1996). Crucial domains are conserved in Enterobacteriaceae porins. FEMS Microbiol Lett *136*, 91-97.

Snijder, H. J., Ubarretxena-Belandia, I., Blaauw, M., Kalk, K. H., Verheij, H. M., Egmond, M. R., Dekker, N., and Dijkstra, B. W. (1999). Structural evidence for dimerization-regulated activation of an integral membrane phospholipase. Nature *401*, 717-721.

Song, L., Hobaugh, M. R., Shustak, C., Cheley, S., Bayley, H., and Gouaux, J. E. (1996). Structure of staphylococcal alpha-hemolysin, a heptameric transmembrane pore. Science *274*, 1859-1866.

Strong, M., Sawaya, M. R., Wang, S., Phillips, M., Cascio, D., and Eisenberg, D. (2006). Toward the structural genomics of complexes: crystal structure of a PE/PPE protein complex from *Mycobacterium tuberculosis*. Proc Natl Acad Sci U S A *103*, 8060-8065.

Subbarao, G.V., and van den Berg, B. (2006). Crystal structure of the monomeric porin OmpG. J Mol Biol *360*, 750-759.

Sugawara, E., and Nikaido, H.(1992). Pore-forming activity of OmpA protein of *Escherichia coli*. J Biol Chem *267*, 2507-2511.

Thiolas, A., Bornet, C., Davin-Regli, A., Pages, J. M., and Bollet, C. (2004). Resistance to imipenem, cefepime, and cefpirome associated with mutation in Omp36 osmoporin of *Enterobacter aerogenes*. Biochem Biophys Res Commun *317*, 851-856.

Trias, J., and Nikaido, H. (1990). Protein D2 channel of the *Pseudomonas aeruginosa* outer membrane has a binding site for basic amino acids and peptides. J Biol Chem *265*, 15680-15684.

Ubarretxena-Belandia, I., Boots, J. W., Verheij, H. M., and Dekker, N. (1998). Role of the cofactor calcium in the activation of outer membrane phospholipase A. Biochemistry *37*, 16011-16018.

Ulukaya, E., Ozdikicioglu, F., Oral, A. Y., and Demirci, M. (2008). The MTT assay yields a relatively lower result of growth inhibition than the ATP assay depending on the chemotherapeutic drugs tested. Toxicol In Vitro *22*, 232-239.

van den Berg, B., Black, P. N., Clemons, W. M., Jr., and Rapoport, T. A. (2004). Crystal structure of the long-chain fatty acid transporter FadL. Science *304*, 1506-1509.

Van Gelder, P., Saint, N., Phale, P., Eppens, E. F., Prilipov, A., van Boxtel, R., Rosenbusch, J. P., and Tommassen, J. (1997). Voltage sensing in the PhoE and OmpF outer membrane porins of Escherichia coli: role of charged residues. J Mol Biol *269*, 468-472.

Vandeputte-Rutten, L., Bos, M. P., Tommassen, J., and Gros, P. (2003). Crystal structure of Neisserial surface protein A (NspA), a conserved outer membrane protein with vaccine potential. J Biol Chem *278*, 24825-24830.

Vandeputte-Rutten, L., Kramer, R. A., Kroon, J., Dekker, N., Egmond, M. R., and Gros, P. (2001). Crystal structure of the outer membrane protease OmpT from *Escherichia coli* suggests a novel catalytic site. Embo J *20*, 5033-5039.

Vistica, D. T., Skehan, P., Scudiero, D., Monks, A., Pittman, A., and Boyd, M. R. (1991). Tetrazolium-based assays for cellular viability: a critical examination of selected parameters affecting formazan production. Cancer Res *51*, 2515-2520.

Vogt, J., and Schulz, G. E. (1999). The structure of the outer membrane protein OmpX from *Escherichia coli* reveals possible mechanisms of virulence. Structure *7*, 1301-1309.

Wallin, E., and von Heijne, G. (1998). Genome-wide analysis of integral membrane proteins from eubacterial, archaean, and eukaryotic organisms. Protein Sci *7*, 1029-1038.

Wandersman, C., and Delepelaire, P. (1990). TolC, an *Escherichia coli* outer membrane protein required for hemolysin secretion. Proc Natl Acad Sci U S A *87*, 4776-4780.

Weiss, M. S., Wacker, T., Weckesser, J., Welte, W., and Schulz, G. E. (1990). The three-dimensional structure of porin from Rhodobacter capsulatus at 3 A resolution. FEBS Lett *267*, 268-272.

Welch, R. A., Burland, V., Plunkett, G., 3rd, Redford, P., Roesch, P., Rasko, D., Buckles, E. L., Liou, S. R., Boutin, A., Hackett, J., *et al.* (2002). Extensive mosaic structure revealed by the complete genome sequence of uropathogenic *Escherichia coli*. Proc Natl Acad Sci U S A *99*, 17020-17024.

Whitfield, C. (2006). Biosynthesis and assembly of capsular polysaccharides in *Escherichia coli*. Annu Rev Biochem *75*, 39-68.

Whitfield, C., and Roberts, I. S. (1999). Structure, assembly and regulation of expression of capsules in *Escherichia coli*. Mol Microbiol *31*, 1307-1319.

Wiener, M. C. (2004). A pedestrian guide to membrane protein crystallization. Methods *34*, 364-372.

Yildiz, O., Vinothkumar, K. R., Goswami, P., and Kuhlbrandt, W. (2006). Structure of the monomeric outer-membrane porin OmpG in the open and closed conformation. EMBO J *25*, 3702-3713.

Yue, W. W., Grizot, S., and Buchanan, S. K. (2003). Structural evidence for iron-free citrate and ferric citrate binding to the TonB-dependent outer membrane transporter FecA. J Mol Biol *332*, 353-368.

Zachariae, U., Kluhspies, T., De, S., Engelhardt, H., and Zeth, K. (2006). High resolution crystal structures and molecular dynamics studies reveal substrate binding in the porin Omp32. J Biol Chem *281*, 7413-7420.

Zeth, K., Diederichs, K., Welte, W., and Engelhardt, H. (2000). Crystal structure of Omp32, the anion-selective porin from Comamonas acidovorans, in complex with a periplasmic peptide at 2.1 Å resolution. Structure *8*, 981-992.